WHEEL/RAIL NOISE AND VIBRATION.
VOLUME I: MECHANICS OF WHEEL/
RAIL NOISE GENERATION

Paul J. Remington, et al

Transportation Systems Center

PB244514

WHEEL/RAIL NOISE AND VIBRATION
Volume I: Mechanics of Wheel/Rail Noise Generation

Paul J. Remington
Michael J. Rudd
István L. Vér

MAY 1975
FINAL REPORT

1. Report No.	2. Government Accession No.	3. Recipient's Catalog No.
UMTA-MA-06-0025-75-10		PB 244 514

4. Title and Subtitle	5. Report Date
WHEEL/RAIL NOISE AND VIBRATION Volume I: Mechanics of Wheel/Rail Noise Generation	May 1975
	6. Performing Organization Code

7. Author(s)	8. Performing Organization Report No.
Paul J. Remington, Michael J. Rudd, István L. Vér	DOT-TSC-UMTA-75-1.I

9. Performing Organization Name and Address	10. Work Unit No.
Bolt Beranek and Newman Inc.* 50 Moulton Street Cambridge MA 02138	UM504/R5721
	11. Contract or Grant No.
	DOT-TSC-644-1
	13. Type of Report and Period Covered

12. Sponsoring Agency Name and Address	
U.S. Department of Transportation Urban Mass Transportation Administration Office of Research and Development Rail Technology Division, Washington DC 20590	Final Report July 1973 to November 1974
	14. Sponsoring Agency Code

15. Supplementary Notes	
*Under contract to:	U.S. Department of Transportation Transportation Systems Center Kendall Square Cambridge MA 02142

16. Abstract Reported here are the final results of a project under the UMTA Urban Rail Supporting Technology Program to develop a basic understanding of urban transit wheel/rail noise control measures. Analytical models of impedance, response, radiation efficiency, and directivity of wheels and rails are presented and compared with field and laboratory measurements. Analytical formulas for the prediction of noise in the three general categories of wheel/rail noise - squeal, impact, and roar - are presented and verified by comparison with laboratory measurements as well as field measurements using a small steel-wheeled personal rapid transit vehicle on a test track. In general, the agreement between the predictions and the measurements is adequate to verify the formulas, although uncertainties in the wheel/rail stick-slip curve and significant variations in roughness across the faces of wheels and rails (measured by a device developed during the program) lead to some uncertainties in the squeal and roar predictions, respectively. A number of new devices for the control of wheel/rail noise are suggested and a number of old techniques are evaluated in light of new information generated during this program. Lastly, testing techniques are suggested for reproducibly evaluating wheel/rail noise control measures. The report is divided into two volumes. The first deals with the theory of wheel/rail noise generation and the second deals with applying the theory to the control of wheel/rail noise.

17. Key Words	18. Distribution Statement
Noise, Transportation Noise, Wheel/Rail Interaction Noise Control	DOCUMENT IS AVAILABLE TO THE PUBLIC THROUGH THE NATIONAL TECHNICAL INFORMATION SERVICE, SPRINGFIELD, VIRGINIA 22161 **PRICES SUBJECT TO CHANGE**

19. Security Classif. (of this report)	20. Security Classif. (of this page)	21. No. of Pages	22. Price
Unclassified	Unclassified	210	7.25/2.25

Form DOT F 1700.7 (8-69)

PREFACE

This final report presents the results of the last four tasks
under a seven-task program to study wheel/rail noise control tech-
nology in urban rail transit systems. The first three tasks,
dealing primarily with a compilation and assessment of state-of-
the-art information on wheel/rail noise and its control, the
development of an acoustic rating scale for wheel/rail noise, and
the development of a methodology for assessing the economic impact
of wheel/rail noise control measures, are the subjects of two
interim reports, Schultz (1974) and Remington *et al* (1974). The
four tasks dealt with here are concerned with the development and
verification of analytical models for the prediction of wheel/
rail noise, the development of innovative measures for the con-
trol of wheel/rail noise, and techniques for assessing the acous-
tic performance of these measures.

The report has been prepared by Bolt Beranek and Newman Inc.
(BBN) under contract DOT-TSC-644 as part of the Urban Rail Sup-
porting Technology Program managed by the Transportation Systems
Center, Cambridge, Massachusetts, under the sponsorship of the
Rail Programs Branch, Urban Mass Transportation Administration,
Washington, D.C.

The report is organized in two volumes and a summary is pro-
vided in Volume I for those who wish to obtain an overview of the
major results and findings without going into the details con-
tained in the main body of the report.

This effort was technically coordinated at the Transportation
Systems Center by Robert Lotz (Code TMP), and was performed prin-
cipally by Paul J. Remington (Program Manager), Michael J. Rudd,
and István Vér, with contributions from Erich K. Bender, Anthony
J. Galaitsis, Michael Alakel, Mark M. Myles, Eric E. Ungar,

Preceding page blank

iii

TABLE OF CONTENTS

VOLUME I

VOLUME II

LIST OF FIGURES

VOLUME I

LIST OF FIGURES *(Cont'd.)*

LIST OF FIGURES *(Cont'd.)*

VOLUME II

xiv

LIST OF FIGURES *(Cont'd.)*

LIST OF FIGURES *(Cont'd.)*

SUMMARY

Conventional mass transit systems which consist of vehicles
with flanged steel wheels running on steel rails offer an econom-
ical, durable, safe, and well-tried means for rapidly transport-
ing large numbers of people in urban areas. A major drawback to
these systems is the intense noise produced by the interaction
between the wheels and the rails. This project was undertaken
to develop analytical models of the wheel/rail noise genera-
tion mechanisms, and from these models, to identify means for
suppression of wheel/rail nois . The results of that program
are presented in this report. This summary presents the major
findings and conclusions of the report for those who wish a
concise overview.

Models of the Wheel/Rail Noise Generating Mechanisms

Wheel/rail noise is commonly divided into three very general
categories — squeal, impact, and roar — each resulting from ex-
citation of the wheel and rail by a different mechanism. Squeal
is the intense noise composed of one or more pure tones that
occurs when wheels of transit vehicles alternately stick and slip
as they pass through short radius curves. Impact is the impul-
sive noise produced by wheels encountering discontinuities, such
as rail joints or flat spots on the wheels themselves. Roar is
the continuous noise caused by the small-scale roughnesses on
wheels and rails.

Figure S-1 shows schematically how the noise is produced.
Each excitation mechanism affects the interaction between the
wheel and the rail and results in a force at the wheel/rail
interface. This force then causes the wheel and rail to respond;
this response, i.e., mechanical vibration, is transformed into
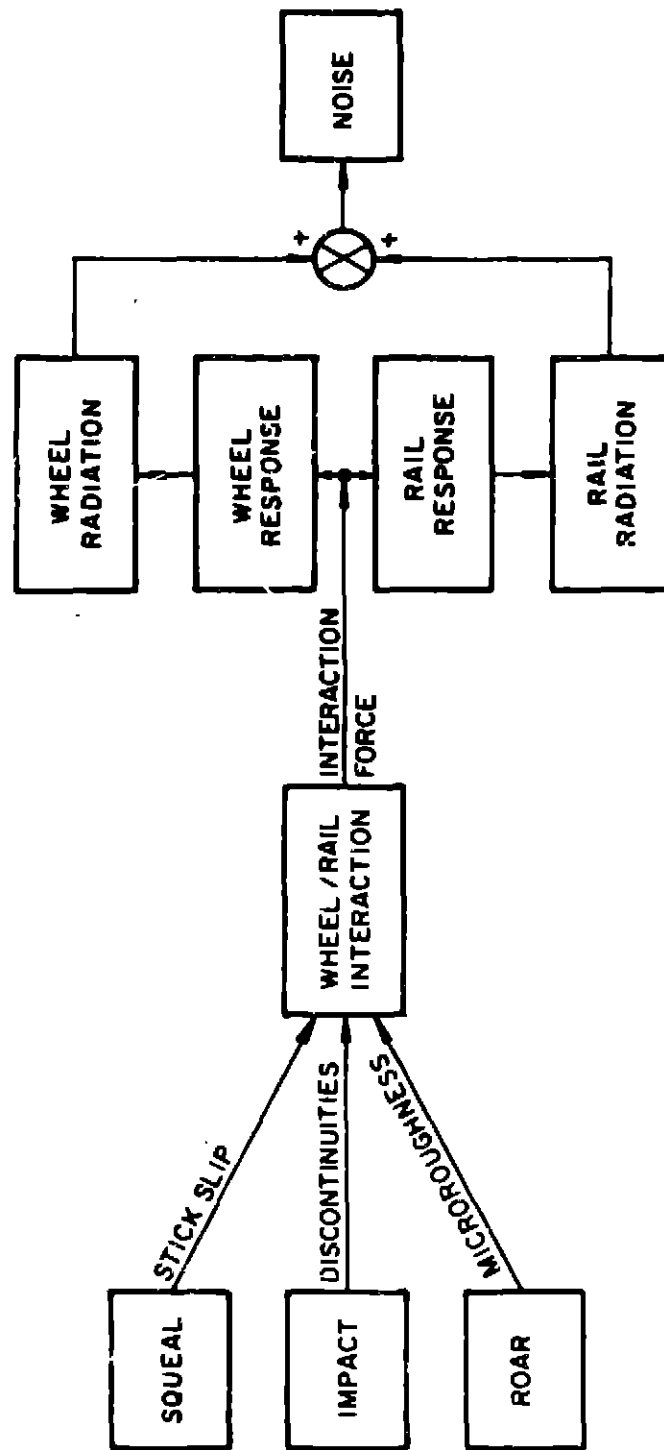
FIG. S-1. PREDICTIVE FORMULA DEVELOPMENT

xx

sound radiation; and the sound from the wheel and rail sum to
produce the total resulting wheel/rail noise. An understanding
of wheel/rail noise generation requires a quantification of the
mechanisms producing the excitation that results in the interac-
tion force at the wheel/rail interface and a quantification of
the wheel/rail dynamic system which transforms the excitation
into sound radiation.

The wheel/rail dynamic system

The response of the wheel and rail at the wheel/rail inter-
face is determined by the relative magnitudes of the wheel and
rail impedances, i.e., their resistance to motion under harmonic
forcing. The spatial distributions of response in the wheel and
rail must be known, so that the response at the wheel/rail inter-
face can be related to the response at the principal radiation
surface of the wheel (the web) and the rail (the head, web, and
foot). In addition, the distribution of response along the rail
must be known, so that the length of rail that radiates can be
determined. Once the response of the appropriate surfaces of
the wheel and rail are known, one can determine from the radia-
tion efficiencies of the wheel and rail how this mechanical
vibration is transformed into radiated acoustic power. Knowledge
of the directivity then enables one to calculate the sound pres-
sure level at a known distance away. Below we list the simple
models used to describe these wheel/rail dynamic properties. The
specific formulas can be found in Sec. 2.1 of the report.

Rail Impedance

- The impedance of a rail on ties and ballast under vertical
  or lateral forcing can be modeled as the impedance of an
  infinitely long beam having the same vertical and lateral

bending stiffness as the rail. This simple model is quite good in the 200 Hz to 4000 Hz frequency range and, in fact, is also approximately valid near rail joints.

- The impedance of a rail on resilient fasteners under vertical forcing is best modeled as the impedance of a beam on an elastic foundation, where the beam has the same bending stiffness as the rail and the foundation stiffness is the fastener stiffness at the operating load divided by the fastener spacing. The model will predict too low an impedance near the resonance frequency of the rail on the fastener owing to the neglect of damping in the fastener, but otherwise is a good model in the 200 Hz to 4000 Hz frequency range.

Wheel Impedance

- The radial wheel impedance in the 200 Hz to 1000 Hz frequency range can be modeled as that of a simple mass equal to the wheel mass plus one-third of the axle mass. Above 1000 Hz the wheel impedance is very approximately modeled as an infinite beam having the same bending stiffness as the wheel tread (without the web) for deflections in the radial direction.

- No simple model has been developed for the highly resonant axial wheel impedance.

Wheel Response

- Under radial forcing at the tread, the web and tread of the wheel respond the same, i.e., the web acceleration levels in the axial direction are of the same magnitude as the tread acceleration levels in the radial direction.

- Under axial forcing at the side of the tread, the axial acceleration levels in the center of the web are 6 to 10 dB below the axial acceleration levels at the side of the tread. This fact suggests a cantilever-like motion of the tread and web about the hub.

Rail Response

- Under vertical forcing at the head of the rail, the head and foot of the rail respond the same way in the vertical direction in the 200 Hz to 3000 Hz frequency range. The web response is negligible up to 4000 Hz. This motion is consistent with the simple beam impedance model.

- Under lateral forcing at the rail head, the horizontal acceleration of the head and the horizontal acceleration level at the center of the web are of the same magnitude in the 200 Hz to 2500 Hz frequency range. Vertical acceleration levels on the foot are negligible to 2000 Hz. Again, this motion is consistent with the simple beam impedance model.

- The decay of vibration along the length of the rail is highest at low frequency. Below 1000 Hz the effective length of rail that radiates sound is approximately 4 ft (1.2 m), from 1000 Hz to 2000 Hz this effective length is about 8 ft (2.5 m), and above 2000 Hz it is in excess of 30 ft (9.1 m).

Rail Radiation Efficiency

- The rail radiation efficiency for vertical forcing at the rail head is well modeled by the radiation efficiency of two rigid cylinders (vibrating independently and at the same levels) having diameters equal to the rail head width and rail foot width, respectively.

- The rail radiation efficiency under lateral forcing at the rail head is well modeled by the radiation efficiency of a rigid cylinder having a diameter equal to the height of the rail.

Wheel Radiation Efficiency

- The wheel radiation efficiency is well modeled by the radiation efficiency of an unbaffled rigid disk vibrating normal to its plane.

Wheel and Rail Directivity

- For estimations of wayside noise, the wheel and rail directivity can be taken as uniform.

Squeal noise predictive formulas

A typical rapid transit rail car is supported on two two-axle trucks. Since the axles are rigidly attached, the truck is not well-suited to steering around curves. However, because the tread of the wheels is tapered, when the truck enters a curve, it moves outwards between the rails; due to the taper, the outer wheel had a larger effective radius than the inner wheel, which enables the truck to roll around the curve. This mechanism only works, however, for curves of a radius greater than about 2000 ft (608 m). On tighter curves, one or more of the wheel flanges rub against the rails. This situation is illustrated in Fig. S-2.

On a tight curve, with radius less than 2000 ft (608 m), the inner and outer wheels of the truck will attempt to roll at different velocities, which will set up a torque in the wheels. The effect of this torque is to compress the tread on the inner wheel and extend it on the outer wheel, thus changing the effective

CRABBING ANGLE

TRUCK

RAIL
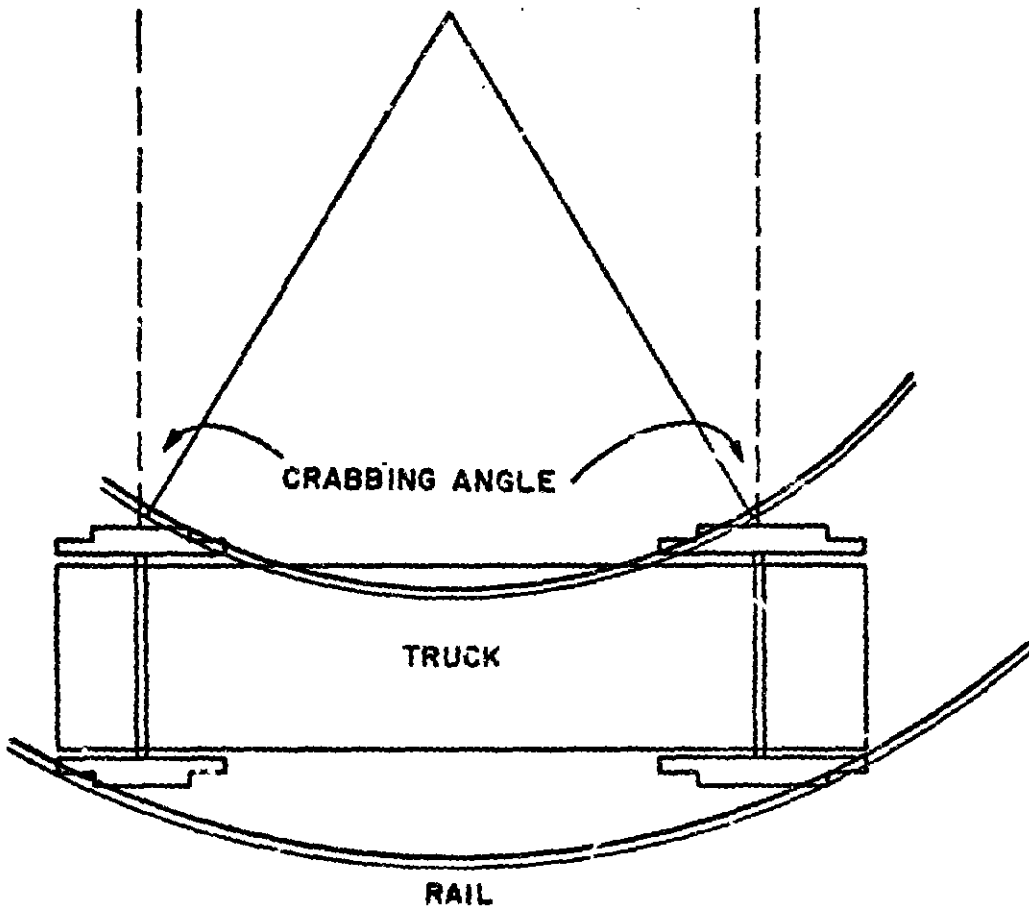
FIG. 5-2. CRABBING OF WHEELS IN A CURVE.

radius of the wheel. It was shown by Remington *et al* (1974) that
this elastic deformation of the wheel was sufficient to allow a
wheel set to roll around quite sharp curves without any macro-
scopic slipping of the wheel.

Since the axles of a two-axle truck are nominally parallel,
even in a curve, it is not possible for both axles to lie along
a radius (see Fig. S-2). This fact means that one or both axles
must slip sideways on the rail as well as roll around the curve.
It is proposed that this lateral slipping of the wheel is the
mechanism which produces squeal. Because the slipping is normal
to the wheel, the wheel will tend to vibrate in this same direc-
tion and its acoustic radiation efficiency will be very good.
This model predicts the very high sound levels which are, in fact,
observed.

The theoretical model used to describe wheel squeal is one
of mechanical instability rather than resonance. The friction of
the wheel on the rail can be described as a damping in the gen-
eralized equation of motion, albeit the damping is nonlinear.
When the wheel starts to slip, the friction decreases and the
slope of friction versus slippage is negative. For small vibra-
tion amplitudes, this situation can be represented by a negative
damping coefficient. If this negative damping is larger in mag-
nitude than the positive damping in the wheel, which is a result
of internal losses and acoustic radiation, then vibrations will
grow in amplitude with time and the wheel is considered vibra-
tionally unstable.

It will be shown that, as the amplitude of vibration increases,
the negative damping decreases until an amplitude is reached at
which the negative and positive damping are equal in magnitude,
after which time the amplitude remains constant. The wheel is then
vibrationally stable.

The acoustic radiation efficiency of the wheel has been measured (Sec. 2.1); hence, if the amplitude of the vibration is known, the radiated sound can be predicted. At the high frequencies of interest for squeal, the wheel is a very efficiency radiator.

The model requires that the negative damping of the stick-slip mechanism excite the wheel or rail at a resonance, since then the imaginary parts of the impedance must disappear. The damping in the rail is very large. A wheel is much more lightly damped and, accordingly, much more easily excited at a resonance. Hence, the model assumes that the wheel becomes vibrationally unstable in one of its natural resonant modes.

There is very little experimental information available on the nature of the stick-slip curve for transverse sliding. Accordingly, an arbitrary analytical function was employed in the model, which had the correct approximate form, yet was analytically tractable. It was found possible to calculate analytically the change in negative damping with vibration amplitude and then calculate the stable vibration amplitude *a priori*. The sound pressure level at 50 ft (15.2 m) can then be calculated from the known acoustic radiation efficiency of the wheel, assuming spherical spreading:

$$L_p \text{ at 50 ft (15.2 m)} = 10 \log \left| \sigma A V \left(\frac{L}{R} - 1.5\, \xi_0 \right) \right|$$

$$+ 113 \text{ dB re } 0.0002 \text{ } \mu\text{bar} ,$$

where σ is acoustic radiation efficiency, A is the area of one side of the wheel, V is train speed, L is length of track wheelbase, R is the curve radius, and ξ_0 is slippage for maximum friction (about 0.7%). This result applies to a wheel with very little

damping and so the damping parameter does not appear. A plot of SPL at 50 ft (15.2 m) versus curve radius for various truck wheelbases is shown in Fig. S-3.

At the same time it is possible to predict how much damping is required in order to stabilize the wheel and suppress squeal. This is given by

$$\eta_{int} > \frac{P\nu_{max}}{m\omega_{min}V}$$

where η is loss factor of wheel, P is wheel loading, ν_{max} is greatest slope of stick-slip curve (between 2 and 30), m is modal mass of wheel, ω_{min} is lowest resonant angular frequency, and V is train speed in the curve.

It has also been found that the *maximum curve radius on which wheel squeal will occur is about 100 times the length of the truck wheelbase*, although this radius will vary somewhat with the state of the rail and the gage relief. Increasing gage relief will *worsen* the occurrence of squeal.

Impact noise predictive formulas

Impact excitation of the wheel and rail occurs if the contact surface of the rail and/or the wheel has discontinuities. Typical rail discontinuities are rail joints, switches, and frogs; wheel discontinuities are generally restricted to wheel flats caused by locking of the wheel during braking.

In the case of a rail discontinuity, a strong impulse sound is generated each time a wheel of a long train passes over the discontinuity, resulting in a quasi-periodic impulse train emanating from the position of the rail discontinuity. The frequency
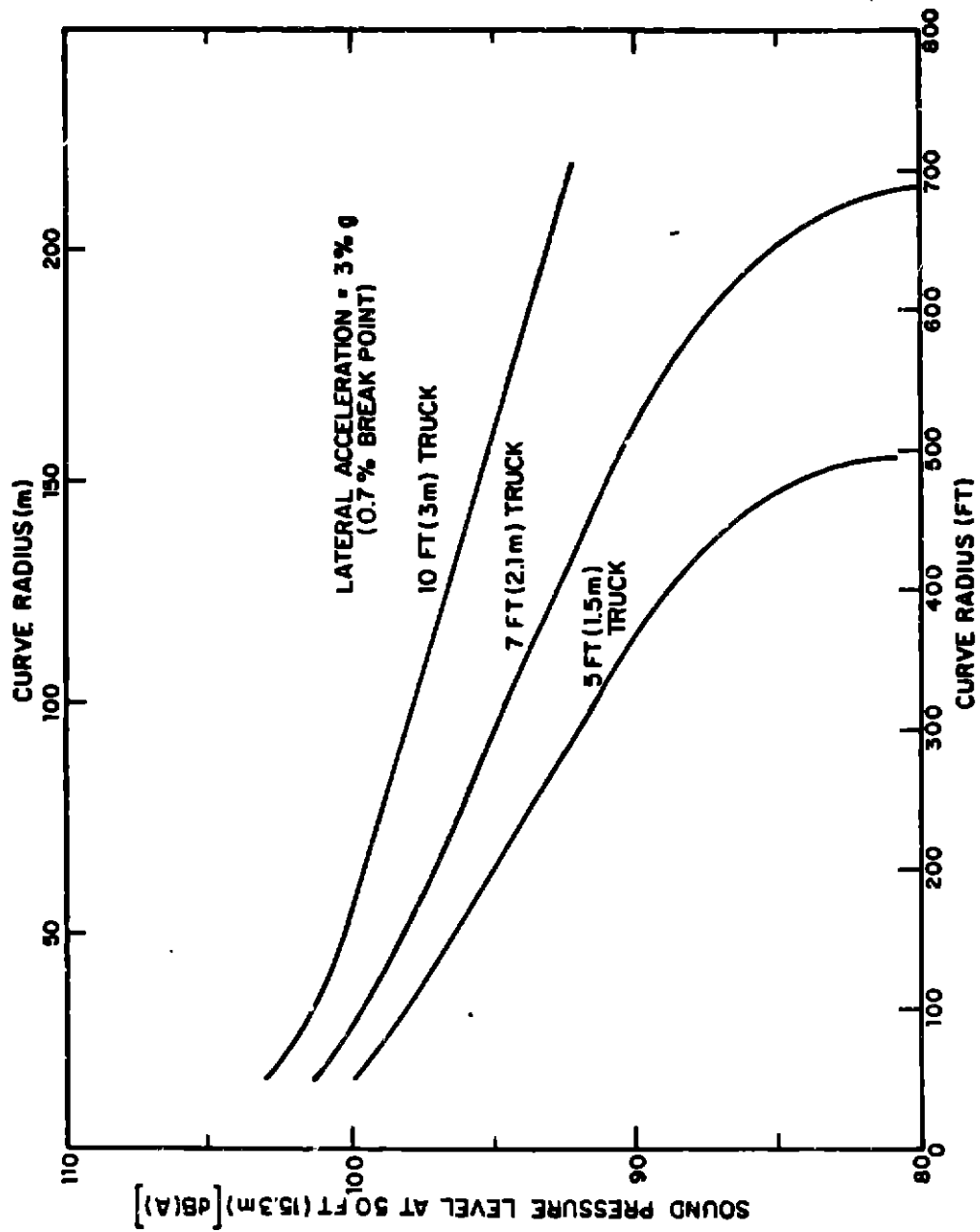
FIG. S-3. PREDICTED SOUND LEVELS OF SQUEAL.

The figure shows a graph with:
- Top axis: CURVE RADIUS (m) with values 50, 100, 150, 200
- Bottom axis: CURVE RADIUS (FT) with values 100, 200, 300, 400, 500, 600, 700, 800
- Left axis (rotated): SOUND PRESSURE LEVEL AT 50 FT (15.3m)[dB(A)] with values 110, 100, 90, 80
- Curves labeled: LATERAL ACCELERATION = 3% g (0.7% BREAK POINT), 10 FT (3m) TRUCK, 7 FT (2.1m) TRUCK, 5 FT (1.5m) TRUCK

of the repetitions and, up to a certain critical speed, the amplitude of the pulse increase linearly with increasing train speed.

As a wheel with a flat spot rolls on the rail, it produces an impulse each time the flat spot comes in contact with the rail head, resulting in a train of periodic pulses, where each pulse is radiated from a different location spaced a wheel-perimeter apart. Here again, the frequency of repetition and, up to a certain critical speed, the amplitude of the pulse increase linearly with train speed.

The generation of impulse noise by rail discontinuities is analogous to hammering on the rail head by a person stationed on the ground at the location of the rail discontinuity. The generation of impulse noise by wheel flats is analogous to hammering on the rail head by a person stationed on the moving car. In both cases, the strength of the impact and the frequency of repetition is proportional to the train speed.

The hammer blow not only gives a good analogy for the temporal and spatial pattern of the impulse train but also describes to a large extent the dynamics of the rail/wheel interaction at discontinuities. The time period during which the dynamic interaction responsible for the sound generation takes places between the wheel and rail is very short. This duration is controlled by the mass of the wheel, the equivalent mass of the rail, and the Hertzian contact stiffness. Because of the short duration of the interaction, most of the dynamic force acting on the rail is compensated for by the inertia of the equivalent rail mass. Only the low-frequency components of the force pulse, which do not contribute much to the sound radiation, are transmitted to the tie and ultimately to the ballast bed. Accordingly, in studying

xxx
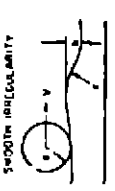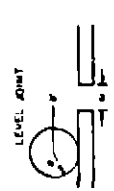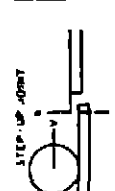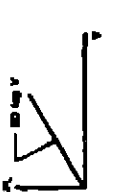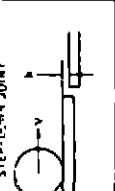
the excitation forces responsible for the generation of impact
noise, the rail can be considered dynamically decoupled from the
tie and the ballast.

According to this impact mode', the duration of the force
pulse is practically fixed. The repetition rate is a simple
function of the train speed. A more difficult task is to charac-
terize the impulse force, which depends on factors such as geom-
etry of the rail and wheel, axle load, dynamic properties of the
rail, and train speed. Consequently, the main thrust of the
investigations was directed towards determining the characteristic
dependence of the force pulse on these variables for various cate-
gories of the rail and wheel discontinuities. This impulse force
acts simultaneously on both rail and wheel, which respond to this
excitation and radiate impulsive sound according to their respective
dynamic properties. It will be shown that this force pulse can
be characterized by the total change in momentum of the impacting
wheel and rail.

Rigid Rail Case

In the case of a rigid rail, the rail head does not move and
the wheel has either to follow the discontinuities of the contact
surface or to separate temporarily from the rail. Since the
magnitude of the generated impact force follows completely dif-
ferent laws depending on whether or not the wheel is separated,
the criteria for wheel separation and the dependence of the im-
pact force generated by various types of impulse producing ir-
regularities have been calculated   Table S-1 shows the geometry
of the configuration, the critical train speed for separation,
the total change in momentum $m\Delta v$ of the impacting wheel above and
below critical speed, and the shape of the typical peak sound
pressure level versus train speed curves caused by a smooth rail

TABLE S-1. SUMMARY OF IMPACT FORMULAS FOR RIGID RAIL.*

Name and Geometry	Critical Train Speed for Separation	Wheel Impulse, maV		Shape of Typical SPL vs Train Speed Curve	Note
		Below Critical Speed	Above Critical Speed		
SMOOTH IRREGULARITY	$V_{CR} = \left[rg\left(1+\frac{M}{m}\right)\right]^{1/2}$		$m\left[2hg\left(1+\frac{M}{m}\right)\right]^{1/2}$		May contribute to rolling noise at high train speeds.
LEVEL JOINT	$V_{CR} = \left[ag\left(1+\frac{M}{m}\right)\right]^{1/2}$	$v\frac{m}{2a}$	$m v\left(1-\frac{M}{m}\right)$ (Not observed)		Inconsequential compared with joints with even the smallest height difference. Dotted portion of curve not observed experimentally.
STEP-UP JOINT	None	$v\left(\frac{2h}{a}\right)^{1/2} m$			Generates highest noise of all geometries.
STEP-DOWN JOINT	$V_{CR} = \left[ag\left(1+\frac{M}{m}\right)\right]^{1/2}$	$v\left(\frac{2h}{a}\right)^{1/2} m$	$V_{CR}\left(\frac{2h}{a}\right)^{1/2} m$		Below V_{CR} same as step-up joint. Above V_{CR} no increase in SPL with increasing train speed.
FLAT WHEEL	$V_{CR} = \left[ag\left(1+\frac{M}{m}\right)\right]^{1/2}$	$v\left(\frac{2h}{a}\right)^{1/2} m$	$2v\left(\frac{2h}{a}\right)^{1/2} m$		Behaves like the step-down joint but change in vertical speed is 2v.

*See Glossary of Symbols following Table S-2.

irregularity, level rail joint, step-up and step-down rail joint, and flat wheel.
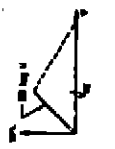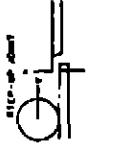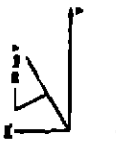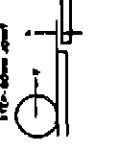
Elastically Mounted Rail

Rails of rapid transit and railroad tracks are elastically mounted. The finite bending stiffness of the rail and the resiliency of the tie and the ballast bed permit the rail to deform under the static as well as dynamic loads. The resilient nature of the rail increases the critical train speed needed for loss of contact and decreases the peak amplitude of the impact forces produced by the various kinds of contact surface irregularities.

Table S-2 provides a summary of the relevant impact formulas for the elastically mounted rail in the same form as presented in Table S-1 for the rigid rail. Comparing the critical train speeds and the magnitude of impact forces for the rigid and elastic rail cases as given in Tables S-1 and S-2, respectively, one notes:

- For the same contact surface discontinuity, an elastically supported rail requires a substantially higher train speed for wheel separation than does a rigid rail. This is because the deformed rail is free to move upward and retains contact with the wheel up to much higher speeds than the rigid rail. The increase in critical speed is roughly proportional to the square root of the equivalent wheel-mass/rail-mass ratio $(m/m_{eq})^{\frac{1}{2}}$.

- For the same contact surface discontinuity and train speed, an elastically supported rail produces substantially smaller impact forces than does a rigid rail. This is because the lighter rail, but not the more massive wheel, must be forced to follow the shape of the contact surface irregularity. The reduction in impact force is proportional to the ratio of the equivalent rail mass and wheel mass, m_{eq}/m.

TABLE S-2. SUMMARY OF IMPACT FORMULAS FOR ELASTICLY SUPPORTED RAIL.*

Name and Geometry	Critical Train Speed for Separation†	Rail Impulse, $m_{eq}\dot{\delta}$		Shape of Typical SPL vs Train Speed Curve	Note
		Below Critical Speed	Above Critical Speed		
SMOOTH MISALIGNMENT	$V_{CR} = V_{CR}\left(1+\frac{m}{m_1}\frac{g}{2}\right)^{b}$		$2m_{eq}v_1\dot{\gamma}_0\left[1-\left(1-\frac{h}{z_0}\right)^2\right]^{b}$ or for $h \ll z_0$, $2(2m_{eq}hP_0)^{b}$		May contribute to rolling noise at high train speeds.
LEVEL JOINT	$V_{CR} = V_{CR}\left(1-\frac{m}{m_1}\frac{g}{2}\right)^{b}$	$v\, m_{eq}\frac{h}{z_0}$			Inconsequential compared with joints with even the smallest height difference. Dotted portion of curve not observed experimentally.
STEP-UP JOINT	None		$v\, m_{eq}\sqrt{\frac{2h}{g}}$		Generates highest noise levels of all geometries.
STEP-DOWN JOINT	$V_{CR} = V_{CR}\left(1+\frac{m}{m_1}\frac{g}{2}\right)^{b}$	$v\, m_{eq}\sqrt{\frac{2h}{g}}$	$2m_{eq}v_1\dot{\gamma}_0\left[1-\left(1-\frac{h}{z_0}\right)^2\right]^{b}$ or for $h \ll z_0$, $2(2m_{eq}hP_0)^{b}$		Below V_{CR} behaves as the step-up joint. Above V_{CR} no increase in SPL with increasing train speed.
FLAT WELD	$V_{CR} = V_{CR}\left(1+\frac{m}{m_1}\frac{g}{2}\right)^{b}$	$v\, m_{eq}\sqrt{\frac{2h}{g}}$	$2m_{eq}v_1\dot{\gamma}_0\left[1-\left(1-\frac{h}{z_0}\right)^2\right]^{b}$ or for $h \ll z_0$, $2(2m_{eq}hP_0)^{b}$		Behaves like the step-down joint of the same h.

*See Glossary of Symbols on next page.

†Formulas for V_{CR} are given in the corresponding rows of Table S-1.

Glossary of Symbols in Tables S-1 and S-2.

a = wheel radius

E = Young's modulus of rail material

F_0 = Mg = static spring force per wheel

g = acceleration of gravity

h = joint height difference or wheel-flat height

I = moment of inertia of the rail cross section

K = foundation stiffness per unit length of rail

m = equivalent mass of single wheel

m_{eq} = equivalent impact mass of the rail

M = spring supported mass of car per wheel

r = radius of curvature

SPL = peak sound pressure level

v_y = vertical velocity of wheel at time of impact

V = train speed

V_{CE} = critical train speed for wheel separation; elastic rail case

V_{CR} = critical train speed for wheel separation; rigid rail case

w = joint gap width

y_0 = static deflection of rail under load

β = $[K/(4EI)]^{\frac{1}{4}}$

ρ_ℓ = rail mass per unit length

ω_0 = $(K/m')^{\frac{1}{2}}$ = resonance frequency of the resiliently supported rail

Comparing the magnitude and characteristic shape of the peak sound pressure level versus train speed curves of the various impact producing contact-surface irregularities for both rigid and elastically supported rail and noting that the sound pressure is directly proportional to the quantity mΔv, as given in Tables S-1 and S-2, one can conclude that:

- Because the peak sound pressure level increases monotonically with increasing train speed and is not masked by the rolling noise at high speeds, the step-up rail joint can be considered the most serious impact noise producing geometry.

- Step-down rail joints and flat wheels cause separation of the wheel from the rail at and above a critical train speed. Above this critical speed, the peak sound pressure does not increase with increasing train speed. Accordingly, the impact noise generated by these geometries is masked by the monotonically increasing rolling noise at high train speeds.

- For the same height difference h, step-up joints, step-down joints, and wheel flats generate the same impact noise below critical speed. The peak sound pressure increases with increasing axle load and height difference.

- Even smooth irregularities can cause separation. The critical train speed where separation occurs increases with increasing axle load and increasing radius of curvature of the irregularity. This special type of impact noise may in fact be part of the rolling noise observed.

- Impact noise generated by level joints is much less than that generated by joints with even the smallest height difference.

Roar noise predictive formulas

Roar noise is produced by the microroughness on wheel and rail surfaces exciting both structures as the wheel rolls over the rail. Taking into account the geometry of receiver position relative to the wheels and rails and the dynamic properties of wheels and rails described above, we have developed formulas predicting the sound pressure level at the wayside. The rail contribution to the 1/3-octave band sound pressure level perceived by a receiver at perpendicular distance R from a rail which 's excited by a single wheel a distance L down the track is gi. ' ry

$$L_p^{(R)} = 10 \log \sigma_R + 10 \log\left(\frac{w_H + w_F}{\pi R}\right) + 10 \log\left|\frac{Z_W}{Z_W + Z_R}\right|^2$$

$$+ 10 \log\left[\left(\frac{\rho c \omega}{p_0}\right)^2 \Phi_{mR}(k)\Delta k |H_{cp}(k)|^2\right]$$

$$+ 10 \log G(\eta R, \eta L) , \qquad (S-1)$$

where σ_R is the rail radiation efficiency, w_H and w_F are the widths of the rail head and foot respectively, Z_W and Z_R the wheel and rail impedances, respectively, ρc the acoustic impedance of air, ω the frequency, p_0 the reference pressure ($2 \cdot 10^{-4}$ μbar), and $\Phi_{mR}(k)\Delta k$ the 1/3-octave band roughness wavenumber spectrum,[*] i.e., the sum of the roughness spectra on the wheel and the rail. The function $G(\eta R, \eta L)$ determines the decay of noise with distance R from the rail, i.e., whether the rail behaves like a point or a line source. This function depends strongly on the

---

[*]The variable k is the wavenumber of the roughness given by $2\pi/\lambda$, where λ is the wavelength of the roughness or ω/V where V is the train speed.

decay of vibration along the length of the rail and is described fully in Sec. 2.4.2. The function $H_{cp}(k)$ reflects the fact that the contact area between the wheel and the rail effectively filters the short wavelength roughness. Typical filter characteristics for a circular contact patch of radius b are shown in Fig. S-4. The variable α reflects the degree of correlation between parallel roughness profiles at a given wavenumber. Large α implies poor correlation and small α good correlation. We find that the curve for $\alpha = 10$ provides the best agreement with data, reflecting the well-known fact that parallel roughness profiles on machined surfaces are poorly correlated.

The wheel contribution to the 1/3-octave band sound pressure level perceived by a receiver a distance R' from a single wheel is given by

$$L_P^{(W)} = 10 \log \sigma_W + 10 \log \frac{a^2}{2R^2} + 10 \log \left| \frac{Z_R}{Z_W + Z_R} \right|$$

$$+ 10 \log \left[\left(\frac{\rho c \omega}{P_0} \right)^2 |H_{cp}(k)|^2 \Phi_{mR}(k) \Delta k \right] , \qquad (S-2)$$

where σ_W is the wheel radiation efficiency and a the wheel radius.

Equation S-1 must be used to estimate the rail contribution due to the excitation from each wheel of the train and Eq. S-2 must be used to obtain the contribution of each wheel.

The quantities σ_W, σ_R, Z_W, and Z_R can be estimated from the formulas and measurements given in Sec. 2.1. The function $G(\eta R, \eta L)$ is given in Sec. 2.4.2 and $H_{cp}(k)$ is shown in Fig. S-4. The wheel/rail roughness $\Phi_{mR}(k) \Delta k$ has been measured with a device that was built especially for this task and that is described fully in Sec. 2.4.3 of the report. Typical 1/3-octave band wheel
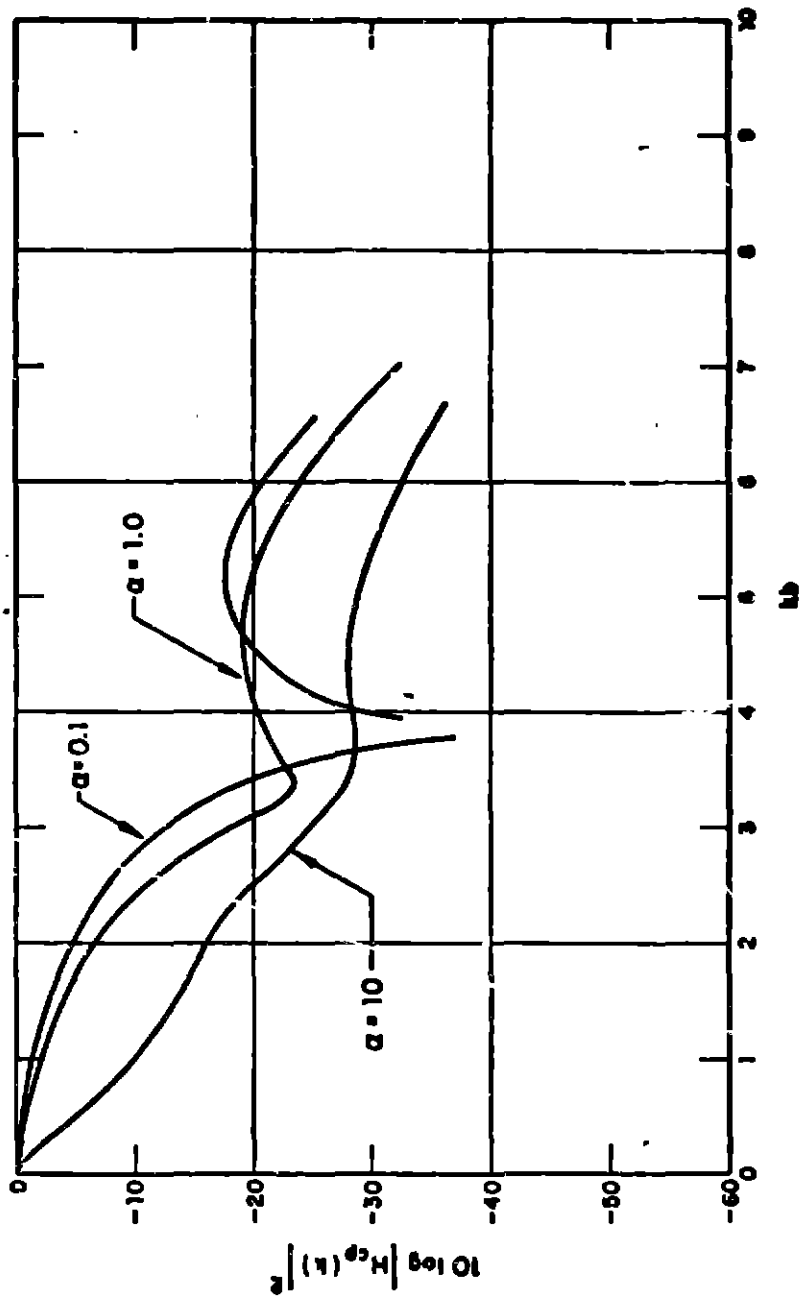
FIG. 5-4.   CONTACT PATCH WAVENUMBER FILTER.

xxxix

and rail roughness spectra measured on the Massachusetts Bay Transportation Authority (MBTA) in Boston are shown in Figs. S-5 and S-6. These data have been used with Eqs. S-1 and S-2 to estimate the noise due to passage of a four-car train at 50 mph (80 km/h) at 25 ft (7.6 m) from the track centerline. These predictions, shown in Fig. S-7, are compared with data measured by Rickley and Quinn (1972) on the South Shore line (welded rail) of the MBTA.

A number of fairly general conclusions have been obtained from this and other similar calculations:

- At low frequencies (around 200 to 400 Hz), the wheel contribution dominates, because the radiation efficiency of the rail is low at these frequencies.

- At mid frequencies (below 1000 Hz but above 200 to 400 Hz), the rail contribution dominates. The reason is that the wheel impedance is much greater than the rail impedance, which causes the rail response to dominate. Since the radiation efficiencies of wheel and rail are comparable, the rail sound radiation dominates.

- At high frequencies (above 1000 Hz), the wheel impedance is much less than the rail impedance, which would imply that the wheel response dominates. However, at these high frequencies, the vibration on the rail decays very slowly along its length, making the rail appear like a line source. The sound pressure level of a line source decays like 10 log R, where R is the distance from the rail to the observer, while the sound pressure level from the wheel, essentially a point source, decays like 20 log R. As a result, whether or not the sound pressure level from wheel or rail dominates depends on the distance of the observer from the wheel and rail.
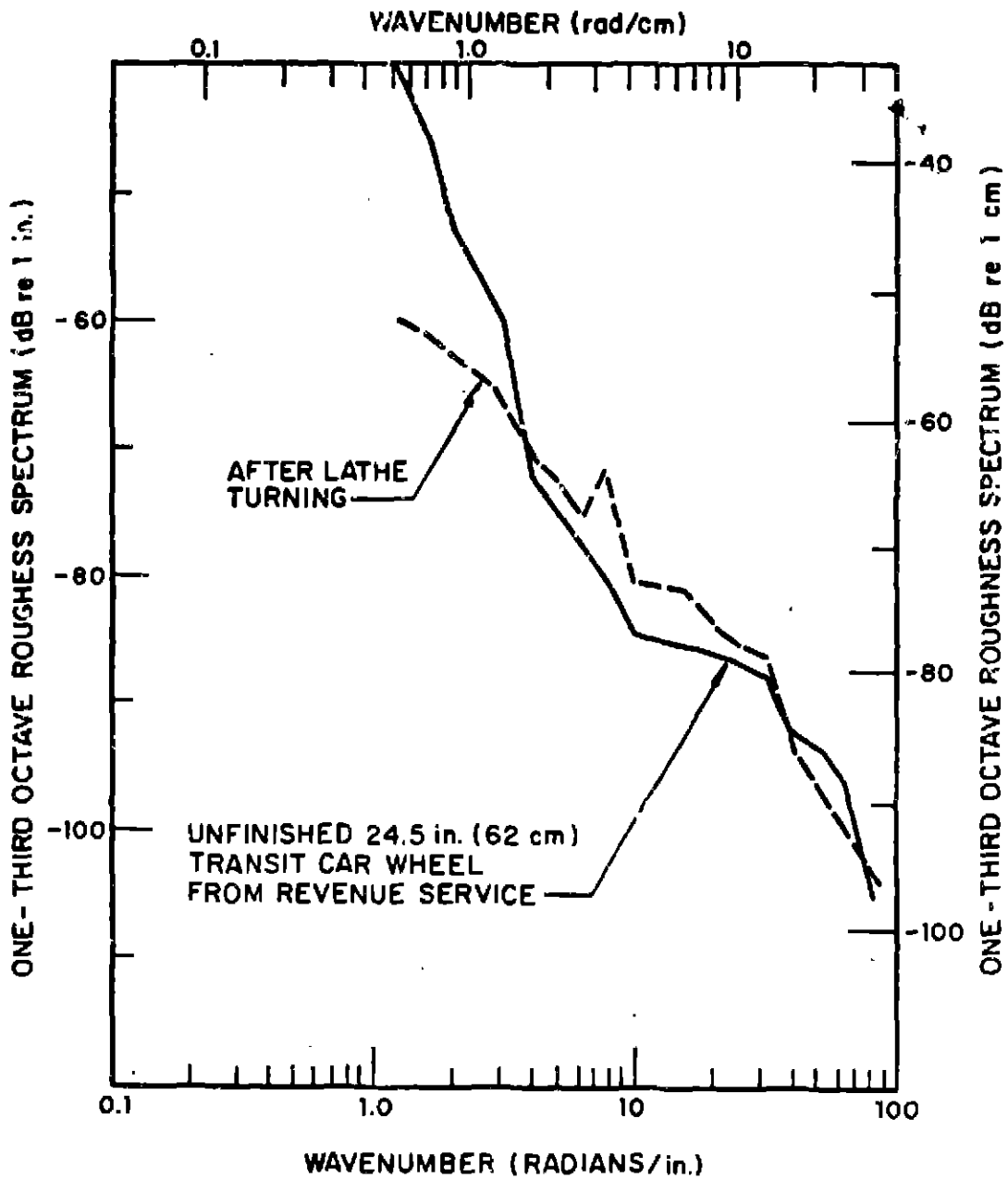
FIG. S-5.   WHEEL WAVENUMBER SPECTRA.
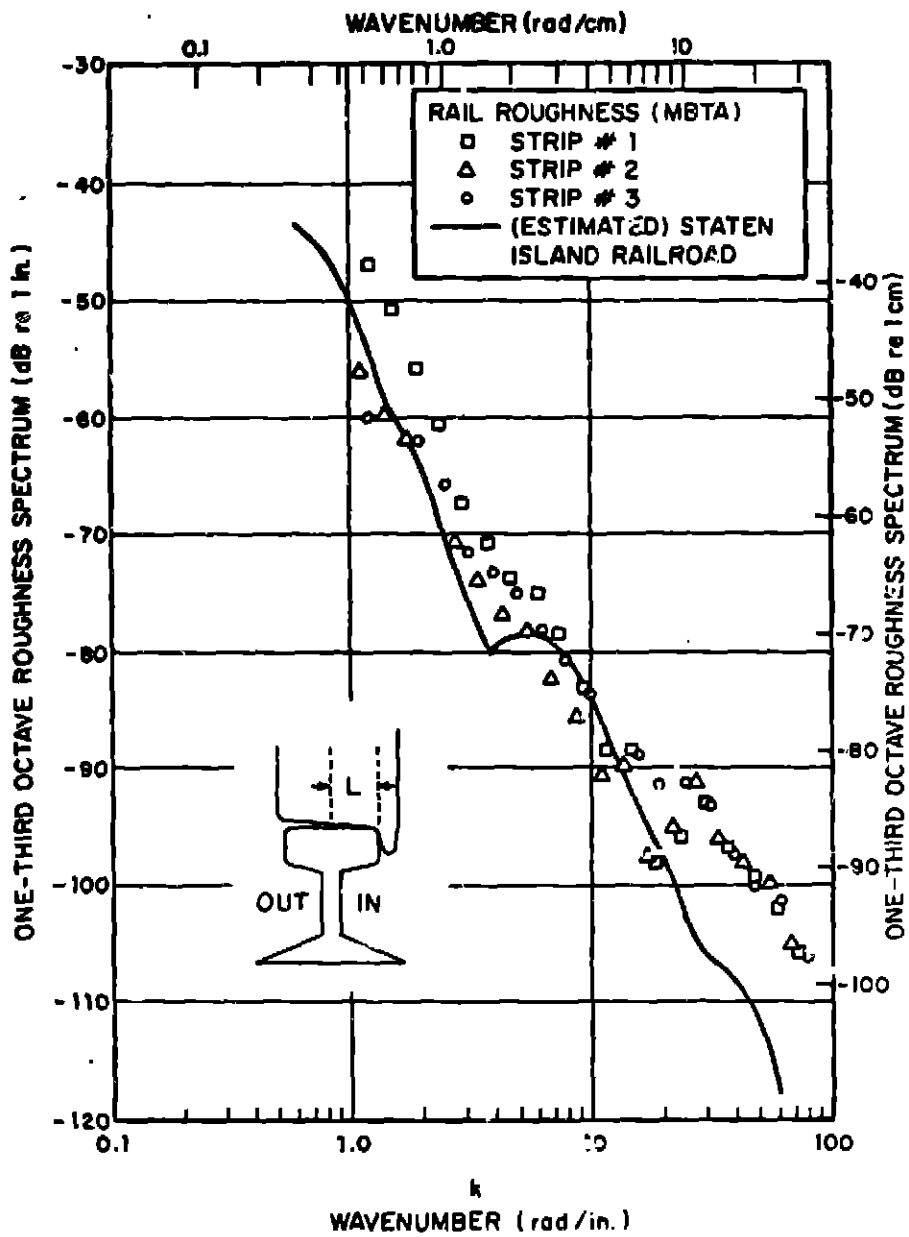
FIG. S-6. MBTA RAIL ROUGHNESS.
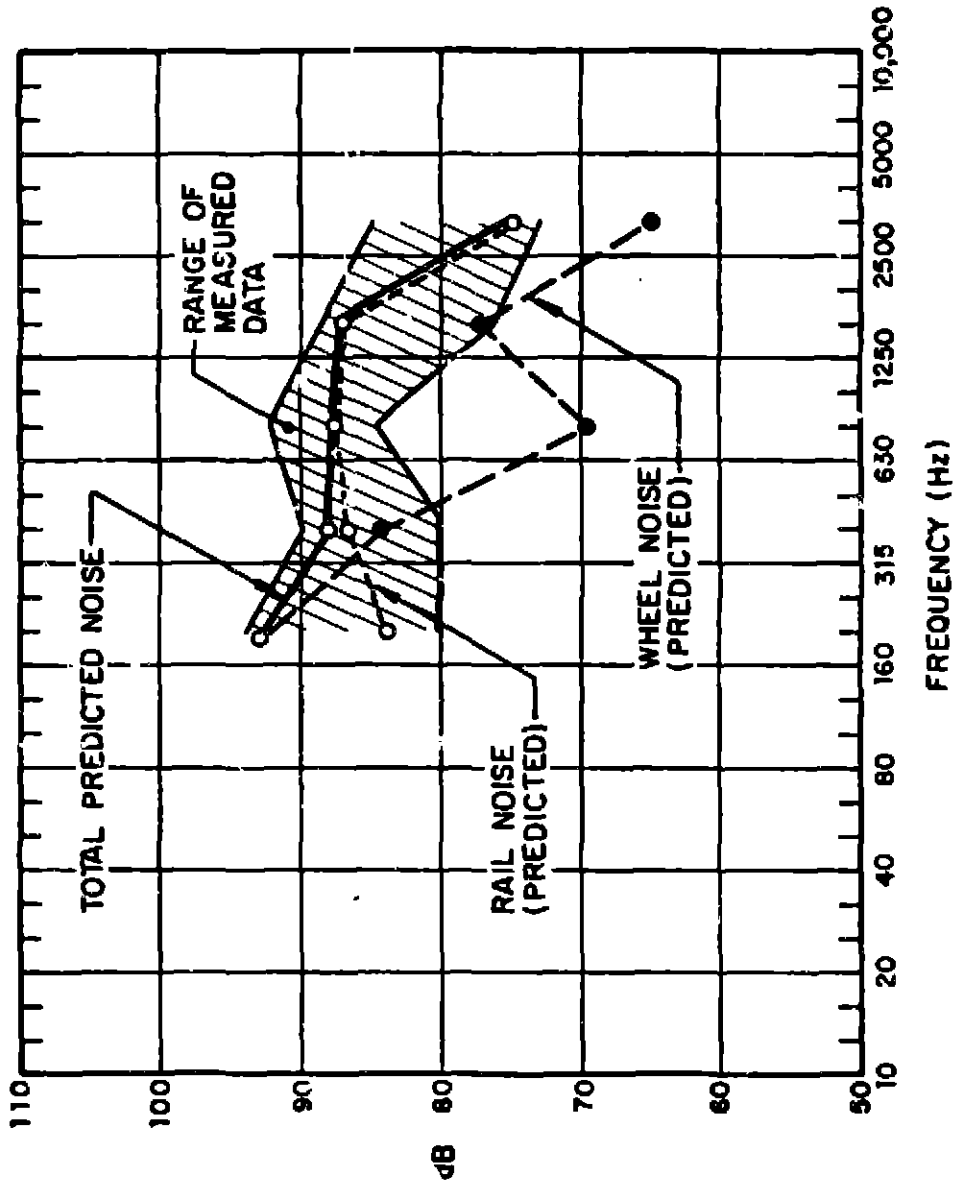
FIG. S-7. COMPARISON OF ROAR NOISE PREDICTIONS AND MEASURED DATA.

Verification of predictive formulas

Confidence in the validity of the predictive formulas for wheel/rail noise was obtained through measurements of wheel/rail noise. These measurements were made with a small (designed for 4 to 6 passengers) steel-wheeled personal rapid transit vehicle (PRT) built by Pullman Standard for the Department of Transportation. The vehicle was run on the Pullman Standard test track at the Champ Carry Technical Center in Hammond, Indiana. Although, ideally, the verification measurements would have been performed on a full-scale transit system, considerable economy and ease of operation were obtained by using the small vehicle. Furthermore, the wheel/rail interaction should be the same for both PRT and full-scale vehicles; therefore, if the predictions can be shown to agree with the measured data from the PRT vehicle, it is very likely that the predictive formulas will be accurate in the full scale.

Measurements were taken of squeal noise on 30-ft and 90-ft (9.2 m and 27.5 m) radius curves, of impact noise at an adjustable rail joint, and of roar noise on a section of welded track where roughness measurements had been taken. The PRT vehicle was equipped with three different types of wheels — standard flanged steel wheels, Penn Cushion resilient wheels, and damped wheels. Details of the instrumentation, PRT vehicle, test track, and wheels can be found in Sec. 3.1.

Wheel squeal predictive formulas

The theoretical model for wheel squeal contains no empirical constants, except for the stick-slip data which were obtained by independent authors. Hence, comparing measured squeal sound levels to predicted levels is a valid test of the model.

Squeal levels were measured as the PRT vehicle passed through
the 30-ft and 90-ft (9.2 m and 27.5 m) radius curves with as wide
a speed range as practical   Figures S-8 and S-9 compare predic-
tions with these measurements. On the 30-ft radius curve, the
measured and predicted sound levels were within ±5 dB in spite of
a large amount of variability in the data. On the 90-ft radius
curve, the levels predicted were about 5 dB higher than those
measured.

The measured frequencies of squeal were compared with the
frequency of the wheel resonances measured in the laboratory and
were found to be a little lower and variable.

An unexpected and very intense squeal at 25 kHz was also
observed on the 30-ft radius curve.

Tests were conducted using resilient and damped wheels to
determine if either type reduced the levels of wheel squeal. The
resilient wheel, which had a loss factor of 3%, eliminated squeal
at the highest speeds and greatly reduced it at lower speeds.
The damped wheel had a very high loss factor at all frequencies,
except its lowest resonance at 1850 Hz, where the loss factor
was 1.3%. Only faint squeal was observed at the lowest speeds
on the 30-ft radius curve and no squeal on the 90-ft radius
curve.

Impact predictive formulas

In the case of the impact predictive formulas, two sets of
verification tests were conducted: scale-model experiments using
BBN's 1:8-scale rail noise research facility and experiments with
the PRT vehicle at the Pullman Standard test track. The results
confirmed the validity of the prediction formulas given in Tables
S-1 and S-2 concerning the characteristic dependence of the peak
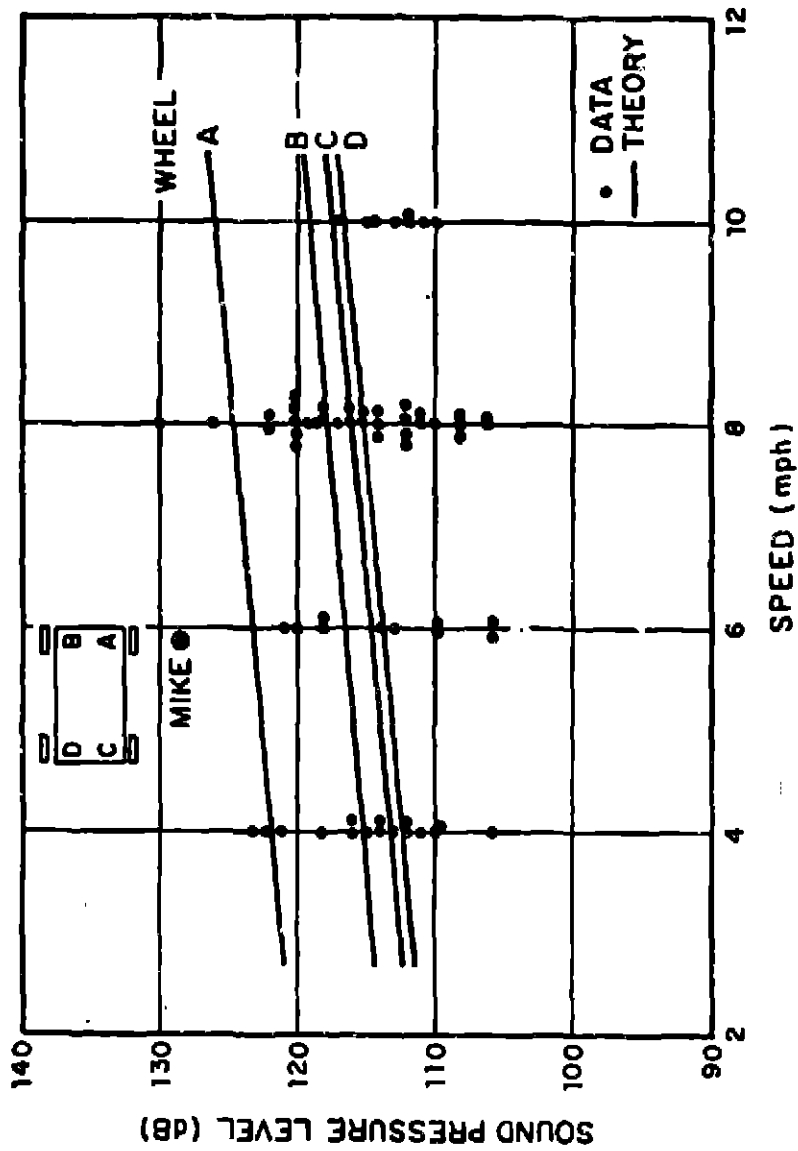
FIG. S-8. SQUEAL SOUND LEVELS VS SPEED ON 30-FT (9.15 m)
RADIUS CURVE.
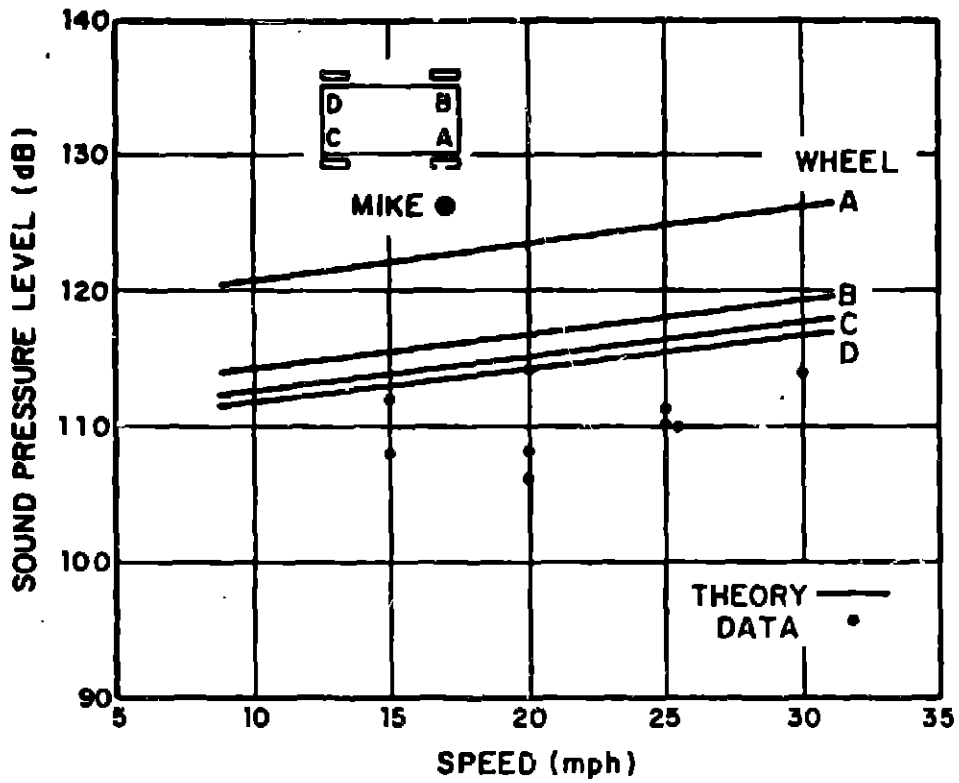
FIG. S-9. SQUEAL SOUND LEVELS VS SPEED ON 90-FT (27.4 m) RADIUS CURVE.

impact sound on train speed, geometry, and axle load. Figures S-10 and S-11, which plot the peak impact noise versus speed for the 1/8-scale model tests, show the predicted 20 log V dependence, where V is the train speed. Comparing the peak impact noise levels in the two figures for the same speeds, one finds that for a joint height change of 0.039 in. (0.010 mm) (Fig. S-10), the peak levels are 4 dB higher than for the joint with a height change of 0.023 in. (0.006 mm) (Fig. S-11). This reult agrees very closely with the 10 log h dependence of the peak impact noise on the joint height change, h. Figure S-12 confirms the fact that impact noise at a step-up joint is independent of the axle load.

The prediction of the time history of the contact force at impact and the corresponding magnitude and spectral distribution of the radiated impact sound would require detailed knowledge of the dynamics of both wheel and rail at the interface and was beyond the scope of the present program. However, if one experimentally evaluates the impact noise produced by a certain vehicle at a well-documented step-down joint as a function of train speed, the formulas given in Table S-2 enable one to estimate the impact noise which would be generated by the same vehicle traversing any other type of discontinuity at any train speed.

Roar predictive formulas

By combining measurements of wheel roughness and rail roughness on a section of welded rail at the Pullman Standard test track with the analytical formulas for roar noise, one can predict the wayside noise due to passage of the PRT vehicle. Measurements of the sound pressure level 3 ft (0.91 m) from the face of one of the wheels of the vehicle (on the wheel axis) were obtained by mounting a microphone and wind screen on a boom at-
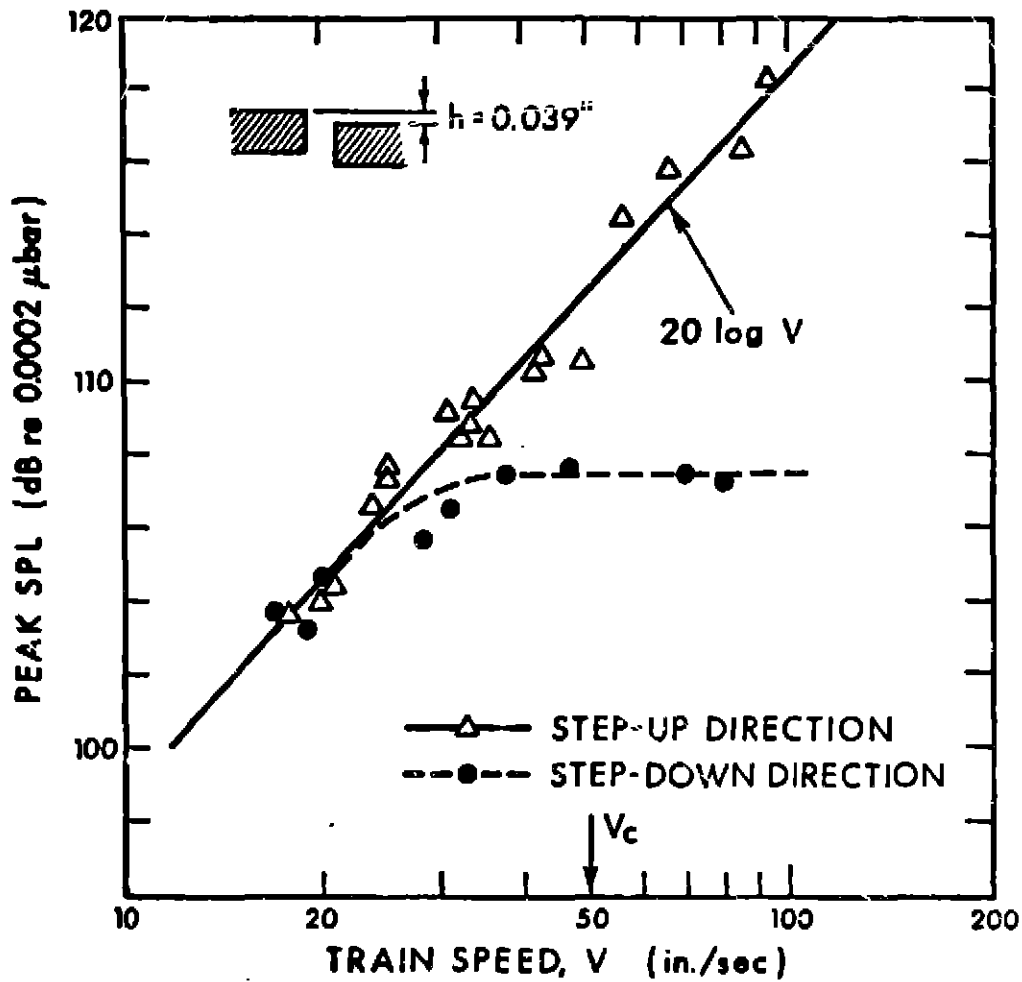
FIG. S-10. PEAK SPL VS TRAIN SPEED CURVES OBTAINED
FOR A RAIL JOINT WITH HEIGHT DIFFERENCE
h = 0.039 in. (0.1 cm) AND STEEL WHEEL —
1/8 SCALE MODEL TRUCK.
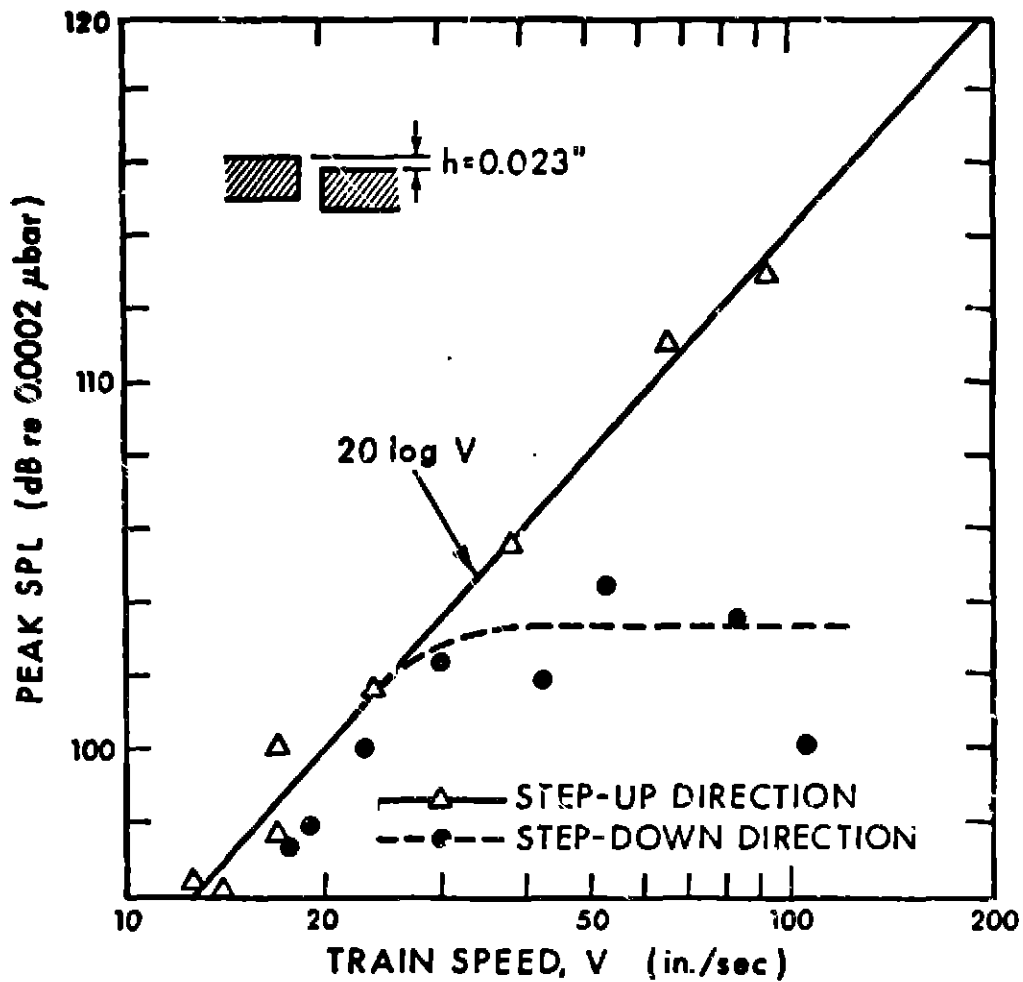
FIG. S-11.   PEAK SPL VS TRAIN SPEED CURVES OBTAINED
FOR A RAIL JOINT WITH HEIGHT DIFFERENCE
h = 0.023 in. (0.056 cm) AND STEEL WHEEL —
1/8 SCALE MODEL TRUCK.

1
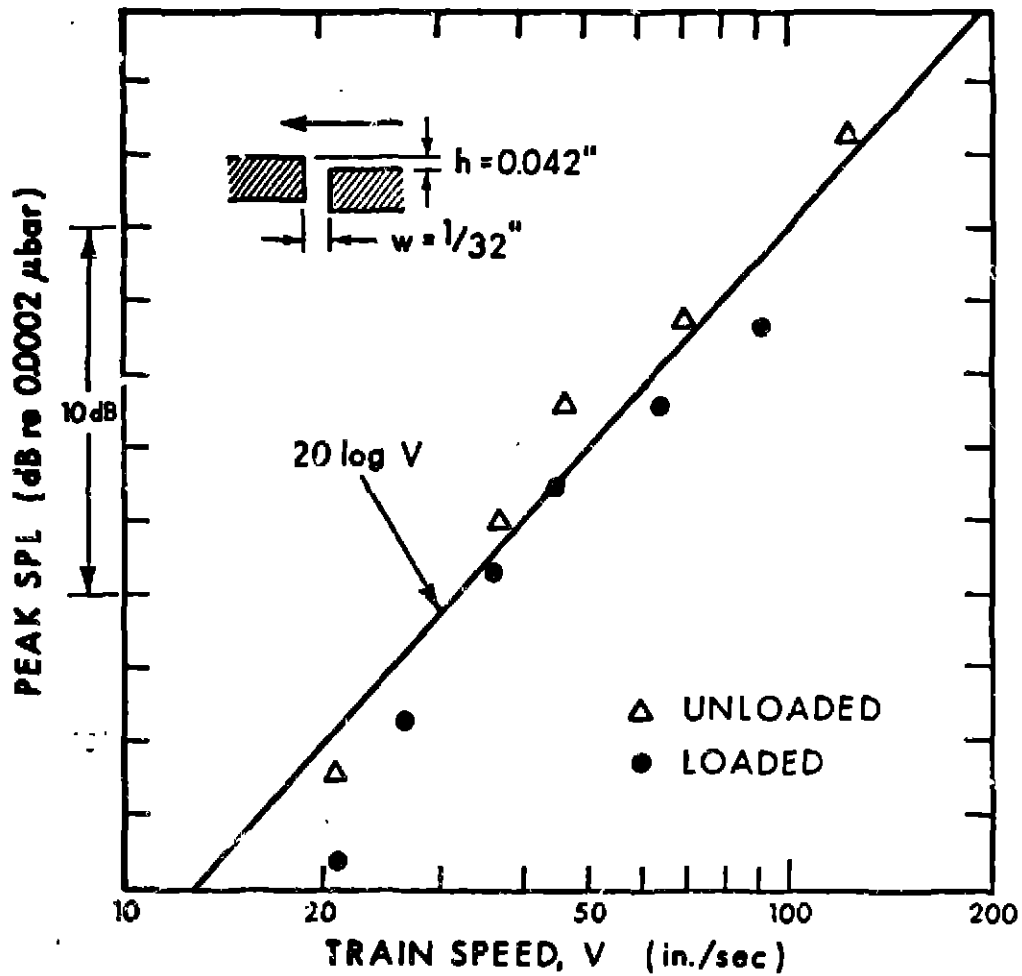
FIG. S-12.   EFFECT OF STATIC AXLE LOAD ON PEAK IMPACT SOUND
            PRESSURE LEVEL FOR TRAVEL IN THE STEP-UP DIREC-
            TION; AXLE LOAD RATIO M/M' = 2.4; STEEL WHEEL —
            1/8 SCALE MODEL TRUCK.

11

attached to the vehicle. Predictions were compared with measurements of the vehicle equipped with standard wheels and traveling at 10, 20, and 25 mph (16, 32, and 40 km/h). In general, the agreement was quite good, as shown in Fig. S-13, for the vehicle passage at 25 mph (40 km/h). Measurements were also performed with the vehicle equipped with damped wheels. The analysis suggested that there would be no change in the roar noise. Measurements generally confirmed this prediction. Finally, with the vehicle equipped with resilient wheels, no significant reduction in roar noise was observed. Again, predictions agreed well with measurements. Section 3.4 of the report presents the details of the predictions and measurements.

Suggestions for the Control of Wheel/Rail Noise

Based on the understanding obtained through the development of the now verified analytical models of the mechanisms for the generation of wheel/rail noise, a number of innovative suggestions for control of this noise have been made. These suggestions are summarized below. Details may be found in Sec. 4.

Wheel squeal noise

Wheel squeal can be suppressed in two ways: by eliminating or reducing the transverse slip of the wheels or by stabilizing the wheel vibrations. The former can be achieved by:

- articulated trucks
- short trucks .

The wheel vibrations can be stabilized by:

- reduced wheel loading
- rail lubrication
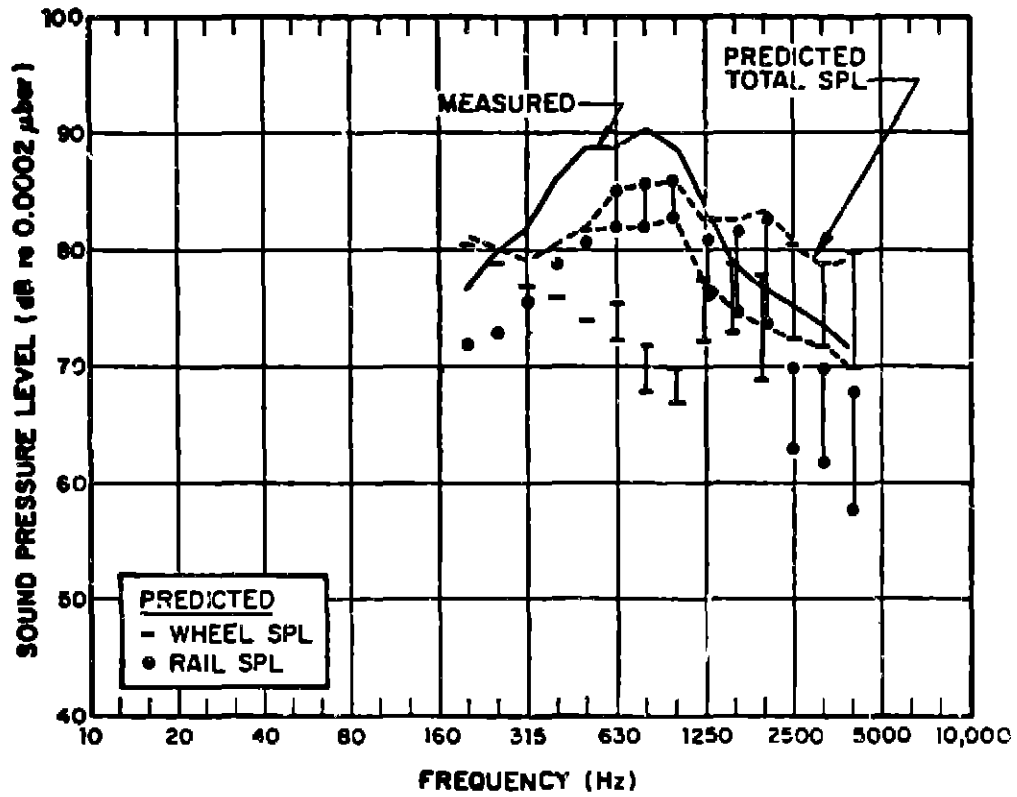
FIG. S-13. WHEEL/RAIL NOISE AT 25 MPH (40 km/h)

- re.ilient wheels
- damped wheels
  - application of viscoelastic material
  - insertion of a damping ring
  - attachment of a damping plate .

The most promising methods are the wheels damped with a visco-
elastic material and rail lubrication.

Impact noise

Since impact noise is generated by discontinuities in the
contact surface of rail and wheel, it could be virtually elimi-
nated by perfect maintenance. Observations made by listening to
passages of well-maintained rolling stock on well-maintained track
with welded rail have proven that impact noise can be reduced to
such an extent that it blends into the rolling noise and becomes
indistinguishable from it. On the other hand, intense impact
noise is a very good indication of the need for maintenance of
track and rolling stock.

The measures for controlling impact noise are listed below
in order of their relative importance:

1. Use welded rail to eliminate rail joints.

2. Maintain rail joints to minimize vertical and horizontal
    micalignment.

3. Provide beneficial contouring of the run-on rail end at
    rail joints.

4. Choose tolerances for vertical alignment of rail joints
    under load so that the joint is a step-down rather than
    a step-up joint for the principal direction of travel.
    This measure could be easily implemented in most rapid
    transit lines.

liv

5. Limit the maximum permissible wheel-flat height by periodic inspection and truing of damaged wheels.

6. Limit the maximum permissible train speed.

7. Limit maximum permissible axle load.

8. Choose the largest practicable wheel radius.

9. Use resilient wheels.

Implementation of any one of the above noise control measures may have a substantial effect on the initial investment or cost of maintenance of rolling stock and track. Formerly untried measures, such as 3 and 4, may introduce new problems in installation and maintenance. Accordingly, the impact of each noise control measure contemplated for an existing or planned vehicle or track must be carefully studied by the design engineer, the maintenance specialist, and the acoustical consultant to ensure that all aspects of cost, safety, and noise-reduction benefits are considered.

Roar noise

Roar noise is produced when the microroughnesses on wheels and rails excite the wheels and rails, which then radiate sound. Three approaches for roar noise control are suggested: a low rail barrier to block rail radiation, a resiliently treaded wheel to reduce wheel and rail response, and wheel truing and rail grinding to reduce the roughness excitation.

- *Rail barrier.* It has been shown that, when the spectrum of roar noise peaks, the rail is the dominant source. Consequently, a low barrier ~6 in. (15.2 cm) from the rail and ~6 in. (15.2 cm) higher than the rail head and on both sides of the rail could result in a 6 to 8 dB(A) reduction in wheel/rail noise 25 ft (7.6 m) or more from the track.

- *Resiliently treaded wheel.* Considerable reduction in roar
  noise can be achieved if the contact patch between the wheel
  and the rail can be enlarged. One method of enlarging the
  contact patch is to use a wheel similar in some respects to
  a resilient wheel. The tread of the wheel is faced with a
  thin [~1/2 in. (12 mm)] resilient layer (probably neoprene)
  and then this layer is faced with a thin tread of steel
  [~1/2 in. (12 mm)] for wear resistance. The result is a
  compliant, yet durable, tread that conforms to the shape of
  the rail head and thereby increases the size of the contact
  patch. This method is expected to achieve ~10 dB reduction
  in roar noise.

- *Wheel truing and rail grinding.* The combined use of wheel
  truing and rail grinding at regular intervals has the poten-
  tial for considerable (10 to 20 dB) reduction in roar noise.
  Unfortunately, it is presently unknown how often these oper-
  ations must be repeated to maintain the noise below a given
  level. Consequently, it is not presently known whether
  truing and grinding is an economically viable noise control
  technique.

Procedures for Testing Wheel/Rail Noise Control Measures

From the knowledge gained through the previous analyses and
field measurements, procedures are suggested for the reprodu-
ible testing of measures for the control of wheel/rail noise.
Section 5 presents these procedures. Since it is a brief section,
the reader is referred there for details.

Future Work

Recommendations for future work emphasize the design, construc-
tion, and field testing of the noise control suggestions described
above. Section 6 gives the details.

1. INTRODUCTION

In recent years attention to increased population and traffic density in cities has created renewed emphasis in this country on the development of safe, fast, reliable, and comfortable urban mass transportation systems. Most existing urban mass transit systems, as well as those planned or under construction, consist of vehicles with flanged metal wheels running on metal rails. The durability, self-guiding capability, low rolling resistance, and high load carrying capacity of this arrangement make it very attractive. Furthermore, steel wheel on steel rail systems have been commonly used in urban mass transit for so many years that there exists a well-established manufacturing and operational technology that tends to encourage new transit systems to be designed using the steel wheel on steel rail concept.

A major drawback of this arrangement for use in urban areas is the intense noise produced by the interaction between the wheel and the rail while the vehicle is in motion. This noise is commonly divided into three very general categories: squeal (or screech), impact, and roar.

Squeal is the term used to describe the intense noise consisting of one or more tones that is associated with transit cars rounding small radius curves. The excitation producing squeal appears to be associated with the fact that, as a transit car rounds a curve, its wheels, because they are attached to a rigid truck, cannot run tangent to the rails. This situation causes what is called "crabbing" (illustrated in exaggerated terms in Fig. 1-1), where the wheel both rolls along the rail and slides laterally across the rail head. The sliding of the wheel across the rail head results in time varying forces being applied to the wheel and rail (due to the sticking and slipping

1
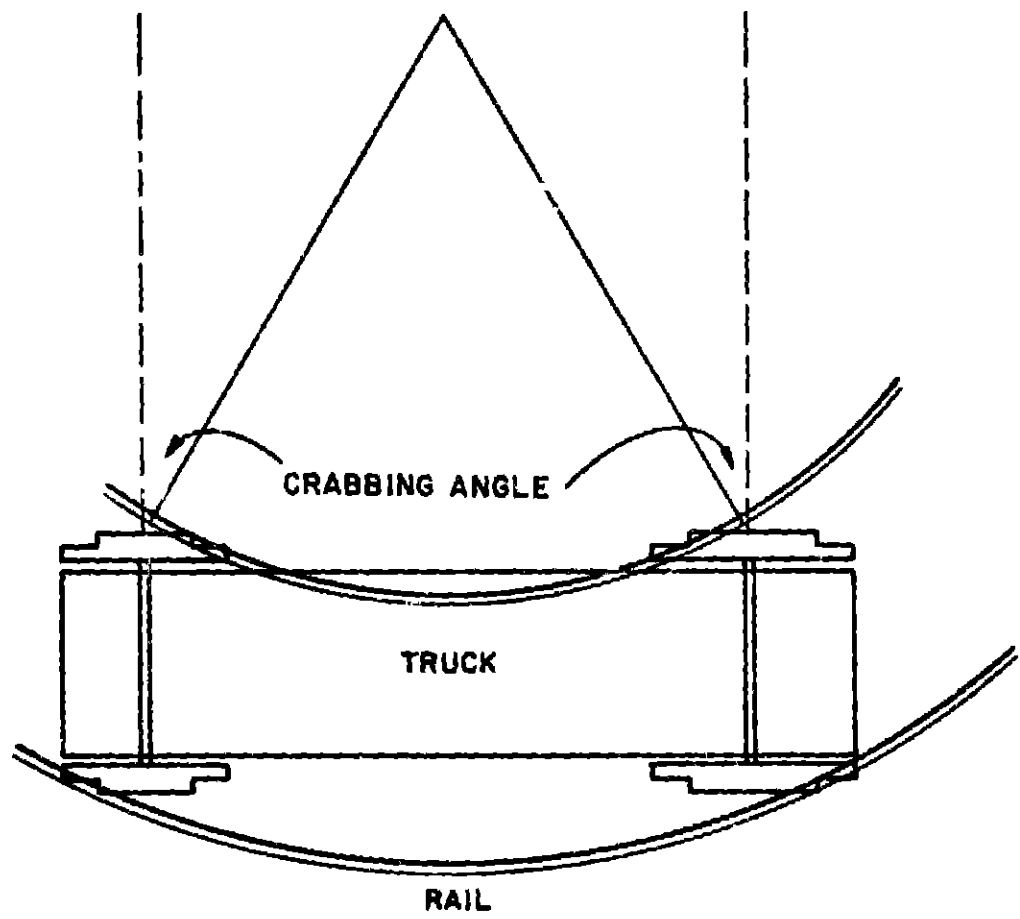
FIG. 1-1. CRABBING OF WHEELS IN A CURVE.

at the interface); this excitation of the wheel and rail results
in sound radiation.

Impact describes the noise associated with wheels rolling
over their own flat spots, over rail joints and over other track
discontinuities. Figure 1-2 illustrates a wheel encountering a
step-up rail joint. As the wheel encounters this change in
elevation, it must either rise up over it, push the rail down
out of the way, or do a little of each. In any evert, the
rapid change in vertical velocity of the wheel and/or rail results
in a large force at the interface, which excites the wheel and
rail and causes them to radiate sound.

Roar noise appears to be produced by the small-scale rough-
ness on wheels and rails. As the wheel rolls over the roughness
(illustrated in exaggerated fashion in Fig. 1-3) and encounters
small bumps and valleys, it must (as when it encounters the much
larger rail joint) either rise up over the bump, push the rail
down out of the way, or do a little of both. The result is a
force at the wheel/rail interface that excites the wheel and the
rail and causes them to radiate sound.

Up to the present time, the mechanisms by which wheel/rail
noise is generated have been poorly understood, hindering the
development of cost-effective advances in its control. The
purpose of the present study is to improve our understanding of
wheel/rail noise mechanisms and apply it to the development of
new wheel/rail noise control devices and procedures.

The first major step in our study of the wheel/rail noise
mechanisms was to develop analytical models of squeal, impact,
and roar, so that the noise from a steel wheel rolling on a
steel rail could be predicted. These models, when verified by
laboratory and field measurements, provided us with the under-
standing of the noise generation mechanisms we needed in order

3

STRUCTURAL VIBRATION

RADIATED SOUND
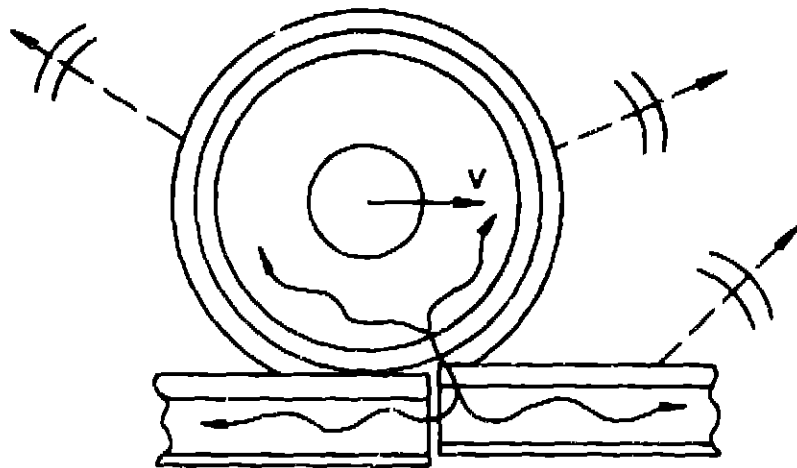
FIG. 1-2.   IMPACT NOISE GENERATION.

4
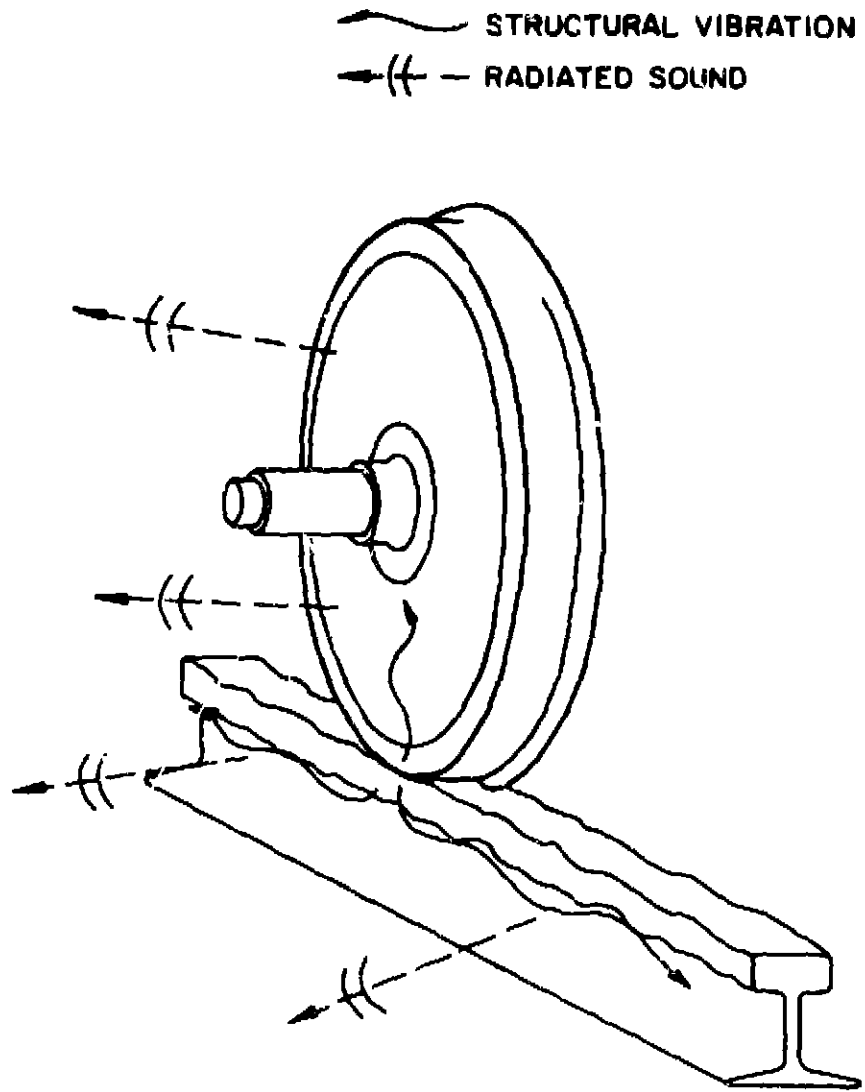
FIG. 1-3. ROAR NOISE GENERATION.

to develop innovative suggestions for the control of wheel/rail
noise. The insight provided by the models also aided us in
designing testing procedures to evaluate noise control measures.

Section 2 presents the analytical models of squeal, impact,
and roar. The major intent of this effort was to provide an
analytical framework that would quantitatively predict trends
in wheel/rail noise in relation to changes in the parameters
defining the wheel/rail system. For example, what would be
the effect of increased wheel loading on roar noise, of shorter
wheelbase trucks on squeal noise, or of increased joint gap
spacing on impact noise? To answer questions such as these in
a quantitative manner, we undertook both analytical and empirical
studies. In order to trace the noise generation process from
excitation to wheel/rail response and then to wheel/rail radia-
tion, it was necessary to define the mechanical and sound radia-
tion properties of the wheel/rail dynamic system through measure-
ments of the impedance, response, radiation efficiency, and direc-
tivity of wheels and rails. Briefly, the impedance is required
for defining the interaction between the wheel and the rail at
their interface; a knowledge of how the wheel and rail respond
is necessary for defining the principal radiating surfaces of
wheels and rails; the radiation efficiency is required for
determining how mechanical vibration is transformed into acous-
tic radiated power; and directivity is required for obtaining
from the radiated power the sound pressure level (SPL) at a
given distance away from the wheel or rail. Of course, under-
standing is not enhanced by the simple acquisition of data alone.
One must relate these data to simple analytical models of the
impedance, response, radiation efficiency, and directivity of
wheels and rails. In this way, one gains insight into the
physical mechanisms operating during wheel/rail interaction as

well as the capability to predict the changes in the above
properties when parameters defining the wheel and rail change.

Since unverified models are unconvincing at best, we sought
to verify these analytical models through comparison of their
predictions with field measurements. Ideally, these field
measurements would have been carried out on a full-scale transit
system. However, considerable economy and logistical advantage
was obtained by performing the field testing on a test track
using a small personal rapid transit (PRT) vehicle constructed
for the Department of Transportation by Pullman Standard. In
many ways the PRT, which runs on four flanged steel wheels, is
similar to a single transit car truck, although there are
differences in gauge, wheel size, wheel loading, and suspension
details. The differences are such that the noise produced by
the PRT vehicle will be different from that of a full-scale
transit car, but the mechanisms for wheel/rail noise generation
will be the same. If the predictions of the analytical models
are found to agree with measurements of wheel/rail noise from
the PRT vehicle, then it is reasonable to expect predictions
based on those models to agree with full-scale measurements.

Measurements of squeal, impact, and roar noise from the
PRT vehicle were made with the vehicle equipped with standard
steel wheels, Penn Cushion resilient wheels, and damped wheels.
For input to the roar noise predictive model, the roughness of
a section of the test track was measured with a device designed
during the program. Squeal and impact required only track
geometry for inputs: curve radius, rail joint gap, etc. Sec-
tion 3 details the PRT measurements and their agreement with
the predictive models.

As mentioned above, based on our understanding of the
mechanisms of wheel/rail noise generation arising from the
development of the now verified analytical models, we sought
to develop innovative suggestions for the control of wheel/rail
noise. In Sec. 4 the difficulties inherent in the problem are
discussed with reference to existing noise control approaches.
In addition, a number of new approaches are suggested, estimates
are made of their anticipated effectiveness, and potential
problems with their implementation are discussed.

Section 5 of the report deals with the development of
procedures for testing the acoustical effectiveness of wheel/
rail noise control measures. While referencing standard testing
procedures for the noise from rail-bound vehicles, Sec. 5 draws
heavily on the knowledge gained from the analyses in Sec. 2 and
the laboratory and field testing in Sec. 3 to present suggested
procedures for obtaining reproducible acoustical performance
data.

Section 6 presents conclusions and suggested new work and
the appendices present details of measurements and analyses
too involved for inclusion in the text.

2.   DEVELOPMENT OF PREDICTIVE FORMULAS FOR WHEEL/RAIL NOISE

In this section we discuss the measurements and analyses required to develop formulas for the prediction of the noise produced by the interaction of metal wheels and rails. In all cases we have sought to relate measurements to the simplest analytical models consistent with the required accuracy, hoping thereby to develop practical formulations to enhance our insight into wheel/rail noise. In later sections we use these formulas to predict wheel/rail noise for comparison with measured data.

2.1   Characterization of the Wheel/Rail Dynamic System

In order to understand and predict the noise generated by rail transit systems, we must thoroughly quantify the dynamic and sound radiation characteristics of wheels and rails. Here, dynamic characteristics refer to how the wheel and rail respond to a dynamic point force such as occurs at the interface between the rail and rolling wheel, Sound radiation characteristics refer to the transformation of the mechanical vibration produced by the interaction of the wheel and rail into acoustic radiation.

One important dynamic characteristic of wheels and rails is their point impedance, a measure of their resistance to motion when excited by a harmonic point force. A knowledge of the relative magnitudes of wheel and rail impedance is crucial to an understanding of wheel/rail interaction because these impedances affect the dynamic behavior of the wheel and rail. Take, for example, the case where the wheel impedance is much greater than the rail impedance. If the wheel encounters a bump as it rolls along the rail, the wheel will not move up over the bump but will push the rail out of the way. If the impedances were reversed, the rail would not move but the wheel would.

Another important consideration is the manner in which different parts of the wheel and rail respond to various excitations. Both are complex structures and it is particularly important for making predictions to know how the different parts of the rail (e.g., the head, web, and foot) respond to excitations applied in various directions to the rail head and also how different parts of the wheel (in particular the tread and web) respond to excitations in various directions at the face of the tread.

When the response of the wheel and rail are known, one can calculate the transformation of their mechanical vibrations into acoustic radiation. A quantity often used to predict this transformation is the radiation efficiency, which relates the sound power radiated by a vibrating structure to the velocity of vibration averaged over the structure and the radiating area of the structure. The sound pressure level radiated to the wayside can in turn be derived from the sound power level predictions when the directivity of the source (both the wheel and the rail in this case) and the distance from source to the observer are known.

In this section we will describe some measurements and simple analytical models of wheel and rail impedance, radiation efficiency, and directivity. In Secs. 2.2 – 2.4, we use these simple models to aid in predicting squeal, impact, and roar noise.

2.1.1 Impedance

As mentioned above, the point impedance of wheels and rails controls the dynamics of their interaction as the wheel rolls on the rail. Various measurements of rail impedance are available in the literature (Bender and Remington, 1974, Naake, 1953) and

several new measurements have been made during the course of this study. The only available measurements of wheel impedance are the ones performed during this program and reported below.

Railroad Rails

We discovered during the course of an extensive literature review (see Remington *et al*, 1974) that measurements of the impedance of rails on resilient fasteners are well modeled analytically by the impedance of a beam on an elastic foundation. This impedance may be expressed by

$$Z_R = j2\sqrt{2} \, (EI)^{\frac{1}{4}} K^{\frac{3}{4}} \frac{1}{\omega} [1 - (\omega/\omega_0)^2]^{\frac{3}{4}} , \qquad \omega \le \omega_0$$

$$= 2(EI)^{\frac{1}{4}} K^{\frac{3}{4}} \frac{1}{\omega} \left[\left(\frac{\omega}{\omega_0}\right)^2 - 1\right]^{\frac{3}{4}} (1-j) , \qquad \omega \ge \omega_0 , \qquad (2.1-1)$$

where j is the square root of -1, E is the modulus of elasticity of the rail material, I is the bending moment of inertia, K is the foundation stiffness per unit length,* $\omega_0 = \sqrt{K/\rho_\ell}$, and ρ_ℓ is the rail mass per unit length.

Although in the literature no such correlation of measurements and analytical models was available for rails on tie and ballast, one would expect that the impedance of a beam on an elastic foundation would still correlate well with measured impedances. In general, ω_0, the resonance frequency of the rail mass on the foundation stiffness, occurs at a lower frequency (less than 100 Hz) for rails on tie and ballast than for resiliently fastened rails. As a result, for most of the

---

*The resilient fastener stiffness divided by the fastener spacing.

audible frequency range (above about 200 Hz), the impedance of
rails on tie and ballast should simplify to (i.e., for $\omega \gg \omega_0$)

$$z_R = 2(EI)^{\frac{1}{4}}\rho_\ell^{\frac{3}{4}}\omega^{\frac{1}{2}}(1-j) , \qquad (2.1-2)$$

which is the impedance of an equivalent infinitely long beam.
The fact that the foundation stiffness does not appear as a
parameter is fortuitous, because estimating that stiffness for
different tie and ballast arrangements would prove to be diffi-
cult.

The only existing data on the impedance of rails on tie
and ballast were obtained by Naake (1953). The measurements
were performed in the vertical and horizontal direction on
rails on ties and ballast with a tie spacing of 2.1 ft (0.65 m).
The bending properties of the rail measured by Naake are given
in Table 2.1 his data are compared with the simple-beam ana-
lytical model in Figs. 2.1-1 and 2.1-2. Agreement between the
phase measurements and predictions is poor, but the impedance
amplitude is fairly well predicted by the simple-beam model
except for strong dips in the impedance at about 800 Hz for the
vertical impedance and about 400 and 800 Hz for the horizontal
impedance. Naake attributes these dips to the periodic support

TABLE 2.1. BENDING PROPERTIES OF THE RAIL IN THE
IMPEDANCE MEASUREMENTS BY NAAKE (1953).

Vertical moment of inertia	42 in.⁴ (1751 cm.⁴)
Horizontal moment of inertia	7.8 in.⁴ (319 cm.⁴)
Cross-sectional area	9.7 in.² (62.3 cm.²)
Mass/unit length	100 lb/yd (48.4 kg/m)
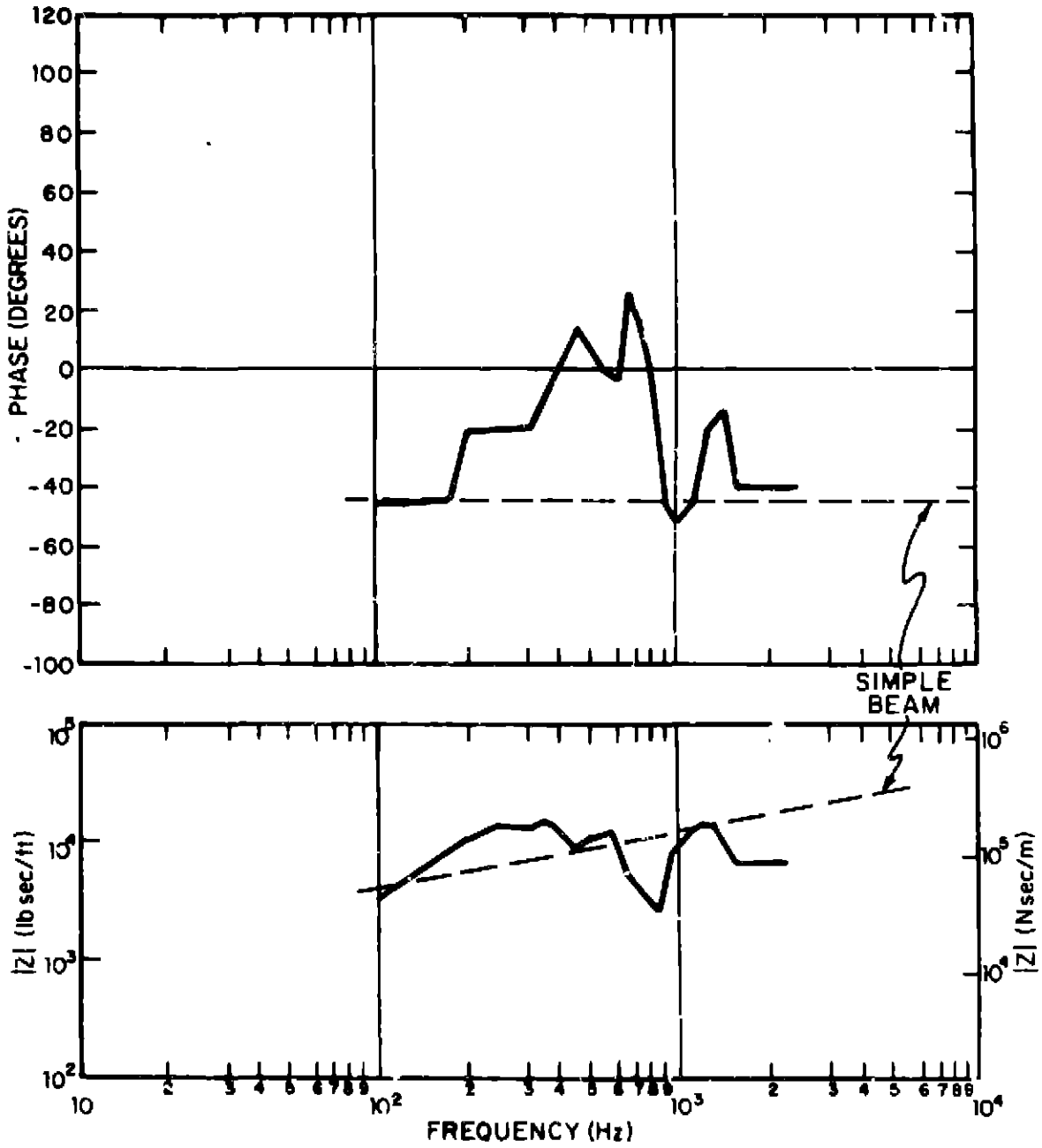
FIG. 2.1-1 VERTICAL IMPEDANCE OF RAIL MOUNTED ON TIE AND BALLAST, FROM NAAKE (1953)
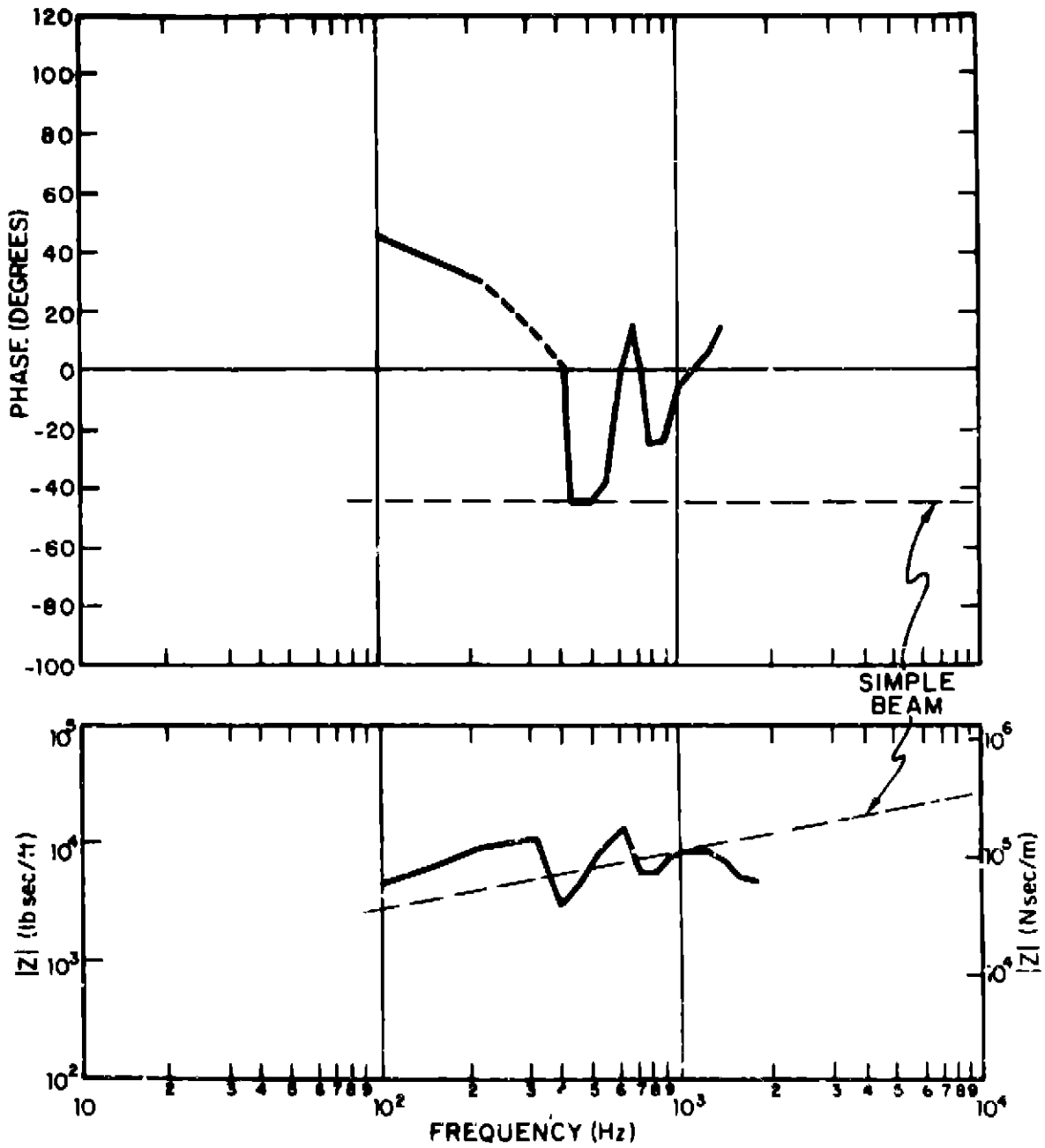
FIG. 2.1-2   HORIZONTAL IMPEDANCE OF RAIL MOUNTED ON TIE AND BALLAST,
FROM NAAKE (1953)

of the rails by the ties, i.e., a half bending wavelength* in
the rail corresponds to the tie spacing.

Because the frequency range of Naake's data is quite
limited and because there are no data available on the impedance
of rails at rail joints, we made arrangements to perform these
measurements on the test track at the Champ Carry Technical
Center of Pullman Standard in Hammond, Indiana. The test track,
a 1/3-mile (0.54 km) oval, contains both welded and bolted ASCE
60 lb/yd (30 kg/m) rail on almost new tie and ballast (see Sec.
3.1). This rail is about one half the weight of rails commonly
used in rapid transit systems. However the excellent condition
of the test track and the ease of obtaining electrical power made
it one of the best sites available. Measurements were performed
on a straight section of the oval by exciting the rail both
laterally at the side of the rail head and vertically at the
top of the rail head with a Goodman V-50 electromagnetic shaker
(with no static load). The shaker was attached to a stud which
was connected to a small ($\frac{1}{2}$ × 1 × $\frac{1}{4}$ in. thick) (12.5 · 25 × 6
mm) aluminum plate glued to the rail. The entire instrumenta-
tion setup is shown in Fig. 2.1-3.

The shaker was excited by 1/10-octave bands of noise from
32.5 Hz to 8 kHz. We chose 1/10-octave band excitation so that
we could examine any detailed changes in the impedance with
frequency that would not be shown up by 1/3-octave band analy-
sis. However, as will be seen below, the impedance was generally
so slowly varying with frequency that data were taken only at
1/3-octave band intervals. The force applied by the shaker to
the rail (generally on the order of a few lbs or less) was

_____

*The dip at 800 Hz for the horizontal impedance corresponds to
 a full bending wavelength.
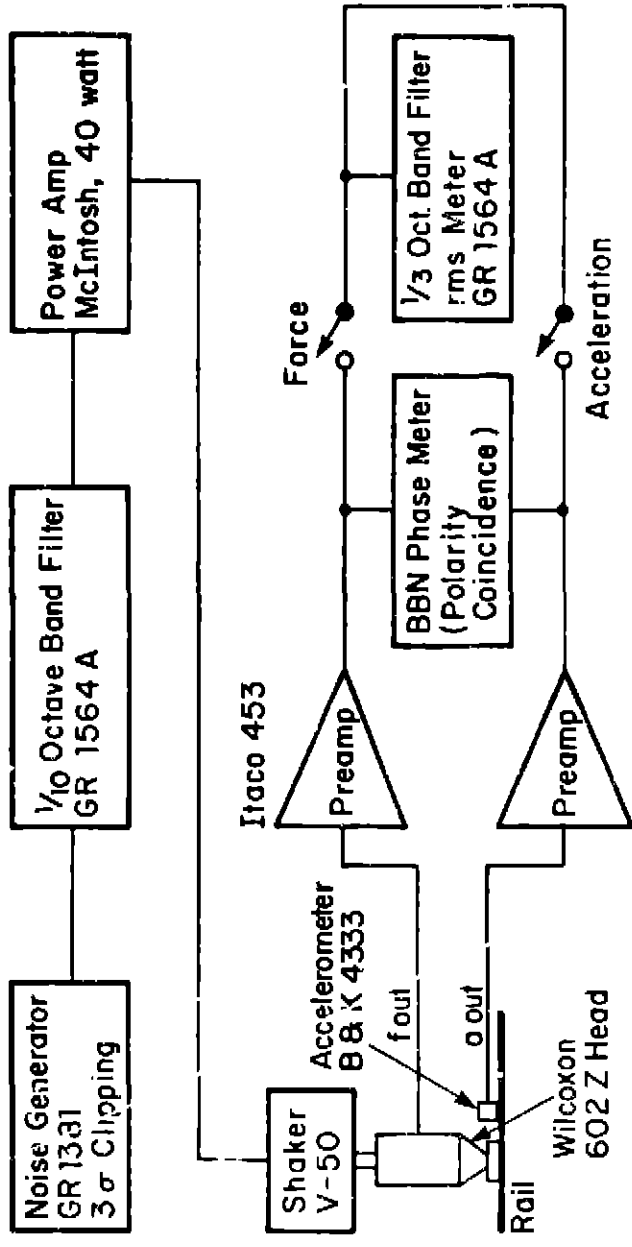
FIG. 2.1-3 RAIL IMPEDANCE MEASUREMENT SETUP

sensed by an impedance head and the acceleration at the point
of excitation was sensed by a separate accelerometer attached
to the rail with beeswax right next to the point of excitation.
These signals were then amplified and measured in broad bands
by what was in effect an rms voltmeter (GR Sound and Vibration
analyzer #1564A). The phase between force and velocity was
then measured at the output of the phase matched preamplifiers
using a polarity coincidence correlator.* Four rail configura-
tions were measured:

1. Vertical forcing of the top of the rail head in the
center of a rail segment between two ties.

2. Horizontal lateral) forcing of the side of the rail
head in the center of a rail segment between two ties.

3. Vertical forcing of the top of the rail head on one
side of a rail joint above a tie.

4. Horizontal (lateral) forcing of the side of the rail
head on one side of a rail joint between two ties.

The phase between force and velocity and the impedance
amplitude for these four cases are shown in Figs. 2.1-4 – 2.1-7.
The polarity coincidence correlator does not give the sign of
the phase angle – i.e., it does not tell which signal is lead-
ing – but gives only the absolute value of the phase angle be-
tween 0° and 180°. As a result, the phase angles given in
Figs. 2.1-4 – 2.1-7 could in fact be shifted by 180°. We have
shown what appears to be the most physically reasonable result.

---

*This device hard clips the inputs, multipl es them together,
and averages them. The result is a normalized output between
+1 volt (0 degrees phase shift) and -1 volt (180° phase shift).
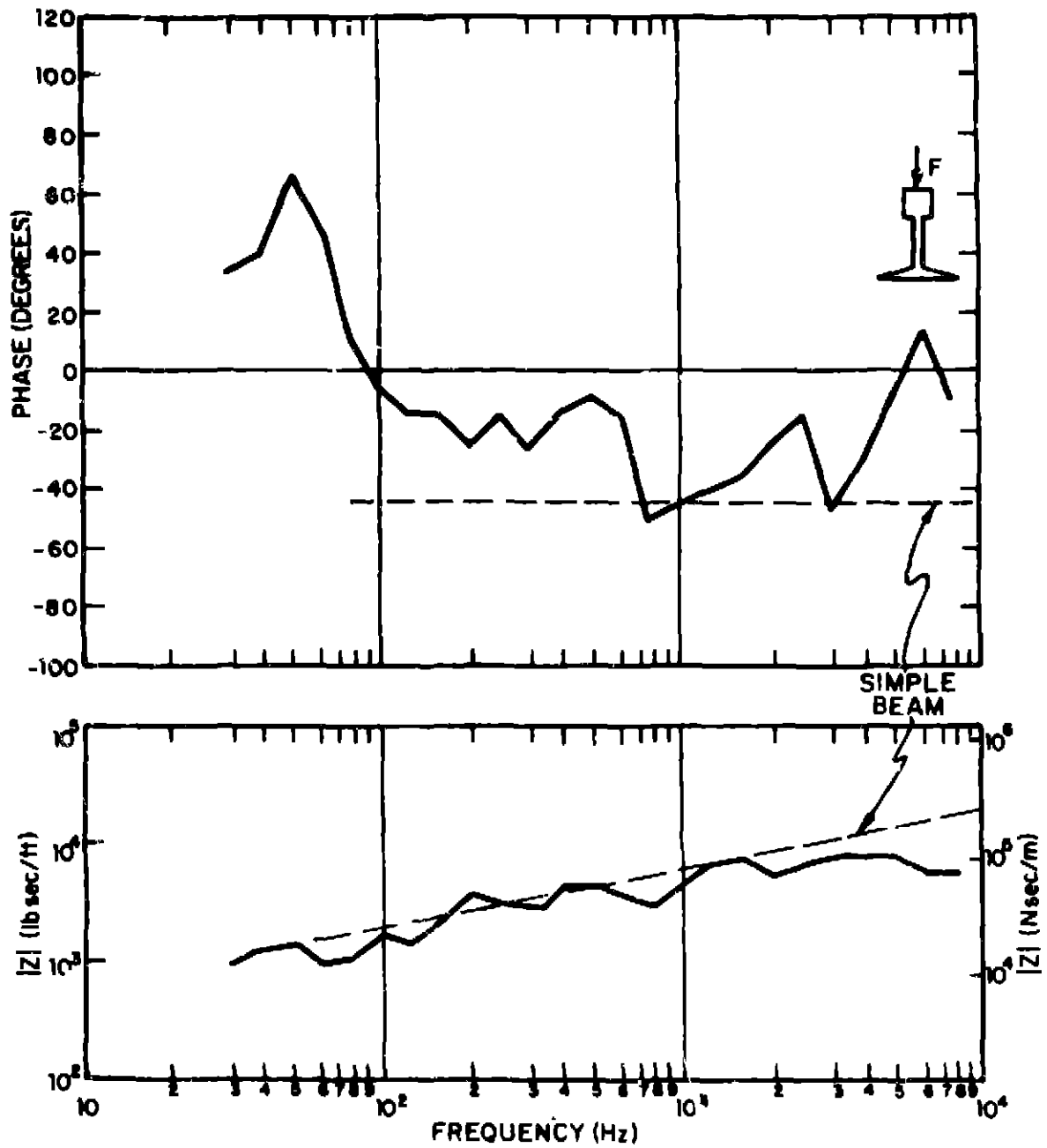
FIG. 2.1-4 VERTICAL IMPEDANCE OF ASCE 60 RAIL MOUNTED ON TIE
AND BALLAST AT A LOCATION AWAY FROM A JOINT BETWEEN
TWO TIES.
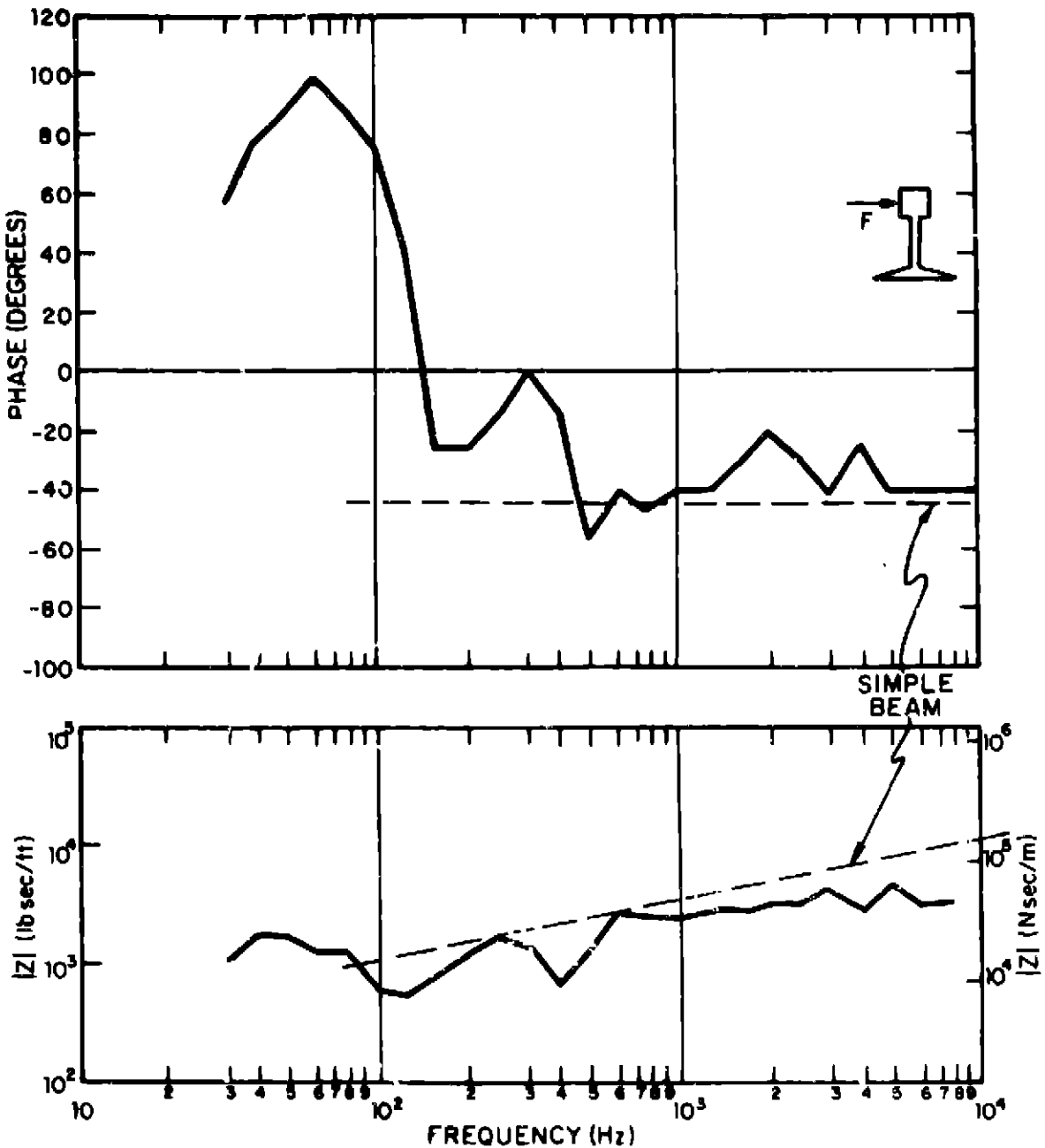
FIG. 2.1-5 HORIZONTAL IMPEDANCE OF ASCE 60 RAIL MOUNTED ON TIE AND BALLAST AT A LOCATION AWAY FROM THE JOINT BETWEEN TWO TIES.
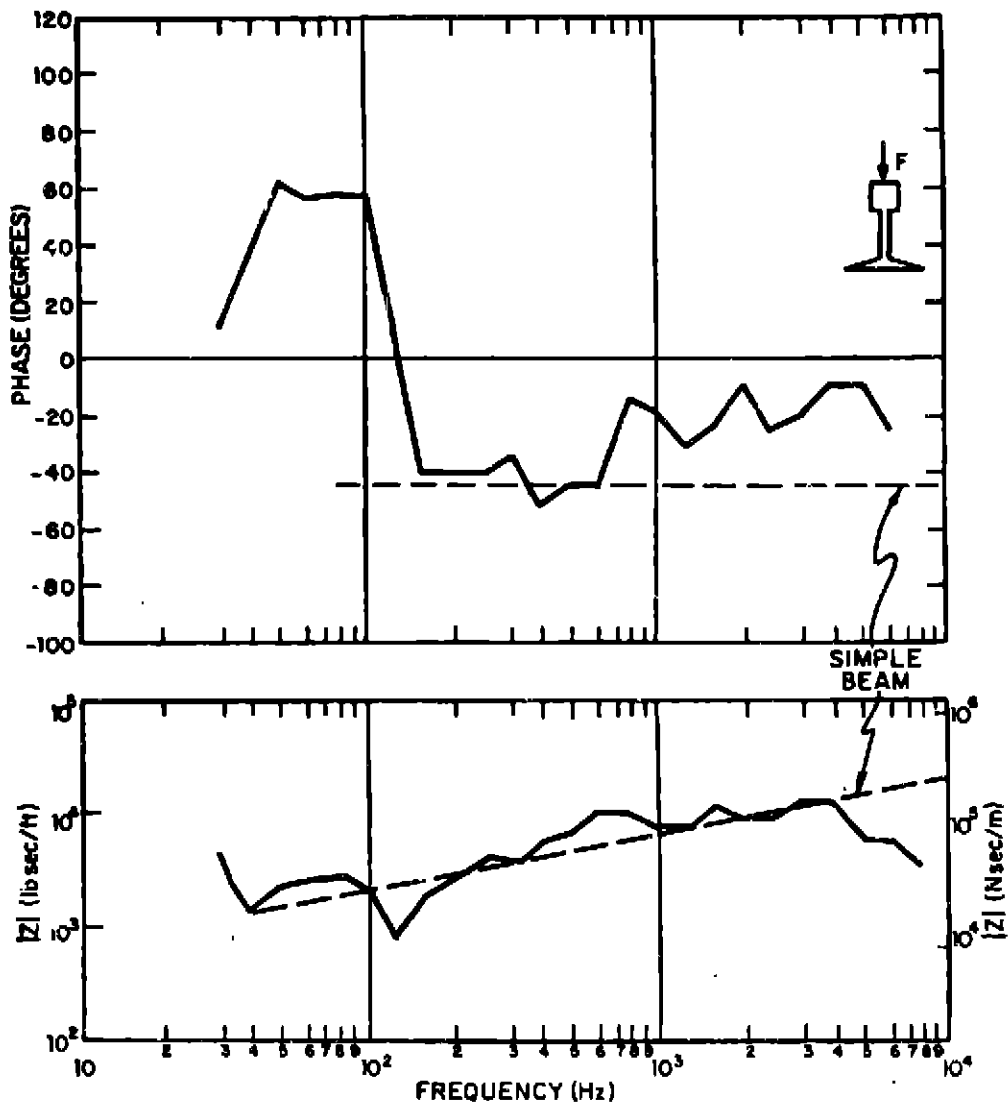
FIG. 2.1-6   VERTICAL IMPEDANCE AT JOINT OF ASCE 60 RAIL
MOUNTED ON TIE AND BALLAST
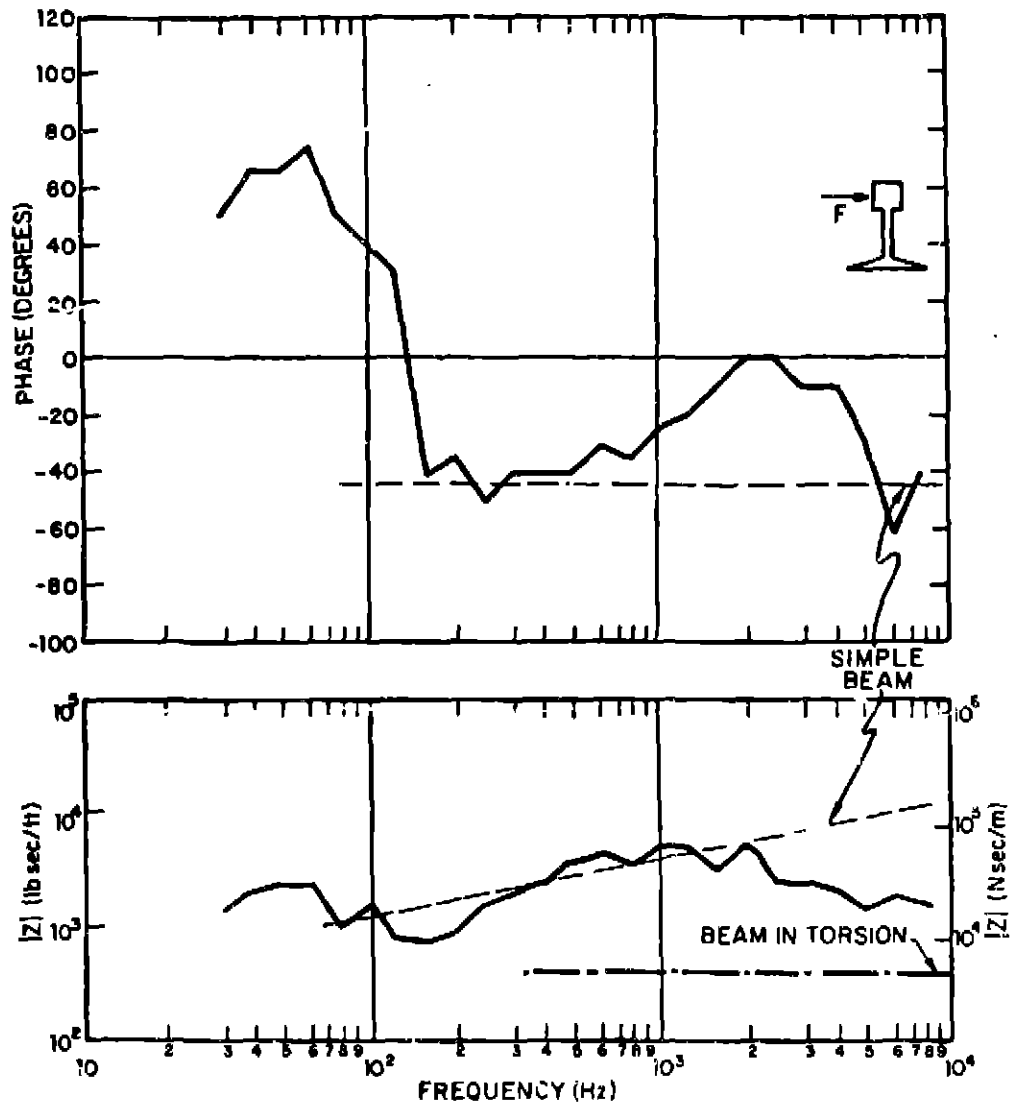
FIG. 2.1-7 HORIZONTAL IMPEDANCE AT THE JOINT OF ASCE 60
RAIL MOUNTED ON TIE AND BALLAST BETWEEN TWO
TIES.

21

It is readily apparent from examination of the phase of
the impedance (i.e., where it goes to zero) that the resonance
of the rail on its foundation is between 90 and 140 Hz for both
the vertical and the horizontal impedance. Pronounced dips in
the impedance amplitude occur at 800 Hz for the vertical force
applied at the center of the rail section (Fig. 2.1-4) and at
400 Hz for the horizontal force applied at the center of the
rail section (Fig. 2.1-5). These dips correspond to the pass-
bands mentioned by Naake (1953) for a beam with the rail bend-
ing stiffness, periodically and simply supported every 2 ft
(0.6 m) (875 Hz and 325 Hz for vertical and horizontal response,
respectively). For a periodically supported beam, there should
be high-frequency passbands at multiples of 4, 9, etc., of the
above frequencies. The reason these passbands do not appear in
the impedance amplitude at high frequency is probably because
of damping, the fact that the measuring bandwidth becomes too
broad at higher frequencies, or dynamic decoupling of the rail
from the ties at high frequencies.

The infinite beam analytical prediction of the impedance
based on the parameters in Table 2.2 is shown as the dotted line
in Figs. 2.1-4 − 2.1-7. For the measured vertical impedance in
Fig. 2.1-4, the agreement with predicted amplitude is good, but
the variations in phase angle from that of a simple beam are

TABLE 2.2.   BENDING PROPERTIES OF ASCE
60 lb/yd (30 kg/m) RAIL.

Vertical moment of inertia	14.6 in.^{4} (610 cm^4)
Horizontal moment of inertia	1.95 in.^{4} (81.5 cm^4)
Cross-sectional area	5.93 in.^{2} (38 cm^2)
Mass/unit length	60 lb/yd (30 kg/m)

substantial. It may, however, be quite difficult to get much
better phase agreement, since that quantity is quite sensitive
to the details of local deformation. Curiously enough, the im-
pedance of a simple beam also fits the measured impedance data
for vertical forcing at a rail joint (Fig. 2.1-6). It appears
that under the conditions tested the joint bars form a very
rigid connection between rail ends.

For horizontal forcing, both in the middle of the rail and
at a rail joint, the rail impedance predicted by the simple-
beam model agrees fairly well with the measured impedance.* The
low-frequency dips in the impedance are due to the rail reso-
nance on the elastic foundation (around 100 Hz) or to the pass-
bands corresponding to the periodic support provided by the
ties (between 300 and 400 Hz). However, the measured impedance
definitely falls below that of the simple-beam model at high
frequency, possibly as a result of the fact (as we shall see
later) that the rail head starts to vibrate independently of
the web and foot at high frequencies.

As a result of the above measurements and analysis,
will analytically model both the vertical and horizontal imped-
ance of a rail on tie and ballast as the impedance of an in-
finitely long unsupported beam. We will use this model for the
impedance near and far removed from the rail joint, bearing in
mind that the model is subject to error in the following re-
gions:

_____

*We have also included in Fig. 2.1-7 an estimate of impedance
 of the rail as if it were an infinitely long beam vibrating in
 torsion (the dot-dash line). Neither the frequency dependence
 nor the amplitude agree with the data, further confirming the
 simple beam-in-bending model.

1. below about 200 Hz due to the resonance of the rail
on the tie and ballast foundation,

2. above 3 to 4 kHz due to the rail head moving independently of the web and foot,

3. at the first passband frequency of the rail on the
ties acting as periodic supports [around 800 Hz for the vertical impedance of a standard transit rail of 100 lb/yd (48 kg/m)
and around 400 Hz for the horizontal impedance of the same
rail].

In all likelihood more complex analytical models of the
rail would provide improved agreement of predictions and data,
but additional complexity is not justified at this time because
equally approximate analyses will be involved in modeling other
aspects of the dynamic and radiation properties of wheels and
rails.

For rails on resilient fasteners, the analytical model we
use is the impedance of an infinite beam on an elastic foundation in which the foundation stiffness, K in Eq. 2.1-1, is the
stiffness of the fastener at the operating load divided by the
fastener spacing. This model has been seen to yield good agreement between prediction and measurement over the range from
40 Hz to about 5000 Hz in one case and from 60 Hz to about
2000 Hz in another case (see Remington et al, 1974). There is,
however, a discrepancy at the resonance frequency of the rail
on the fastener (ω_0) because the damping in the rail fasteners
is not included in the analytical model. One could include
this damping simply by taking K as complex, i.e., K = K_0 (1+ n)
where n is the loss factor, in Eq. 2.1-1, but, of course, this
would require measurements of the complex stiffness of the resilient fasteners of interest. Unfortunately, these measurements are not presently available for any resilient fasteners.

However, we shall see later on that the prediction of the exact magnitude of the rail impedance in the frequency range where resonances occur may not be critical to the prediction of wheel/rail noise.

Railroad Wheels

The lack of measured data on railroad wheel impedance has permitted development of only the simplest models. One such model considers the radial impedance of a railroad wheel as the impedance of a simple mass

$$Z_W = j\omega m , \qquad (2.1-3)$$

where m is the mass of the wheel. This model assumes that there are no resonance frequencies of the wheel in the frequency range of interest, which is not true for wheel/rail noise.

To increase our understanding of wheel impedance, we decided to measure the wheel impedance of a railroad wheel attached to a truck. Arrangements were made with Pullman Standard to visit their "car works" at 111*th* St., Chicago, Ill. There they provided us with a passenger car truck jacked up to provide access to the wheels.*

The 4-wheel truck [36 in. (0.91 m) running tread diameter wheels] was a General Steel Foundaries inside swing hanger truck, Serial No. 146-NYC A-6937; it is shown schematically in Fig. 2.1-8. The truck was raised approximately 2 ft (0.6 m) off the ground and supported at the bearing boxes by thick rubber pads on top of steel columns. One wheel of the truck was

---

*A transit car truck was not available. The passenger car truck was quite similar to transit car trucks except for the absence of drive motors.

SIDE FRAME

SPRING SUPPORTING SIDE FRAME
ON EQUALIZER

SWING HANGERS

BOLSTER

SPRINGS SUPPORTING
BOLSTER

EQUALIZER

BEARING
BLOCK

IMPEDANCE
MEASUREMENT
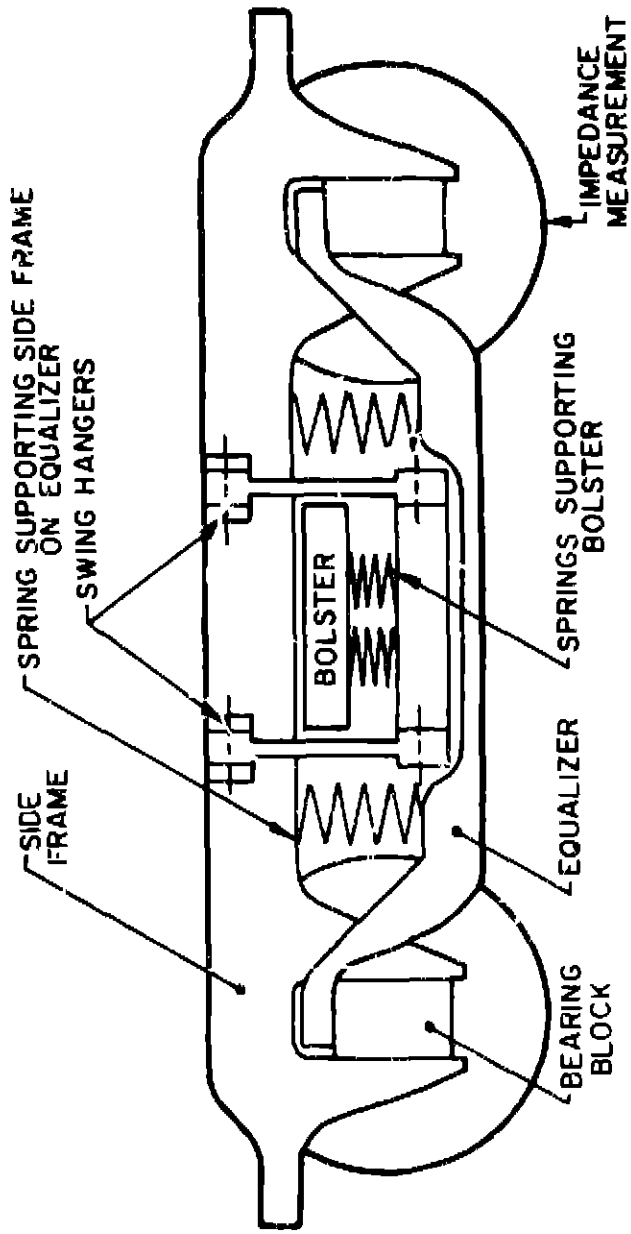
FIG. 2.1-8 SCHEMATIC OF THE PASSENGER CAR TRUCK ON WHICH WHEEL IMPEDANCE
MEASUREMENTS WERE MADE

forced in the center of the face of the tread in the radial direction and at the side of the tread in the axial direction with a Goodman V-50 electromagnetic shaker. A stud connected the shaker to a small (½ × 1 × ¼ in. thick) (12.5 × 25 × 6 mm) aluminum plate glued to the wheel. The measurement setup was exactly the same as the rail impedance measurement setup shown in Fig. 2.1-3.

The results of the radial and axial impedance measurements are shown in Figs. 2.1-9 and 2.1-10, respectively. Two observations are readily apparent. First, there is a substantial reduction in the radial (vertical) wheel impedance at ~1000 Hz, due to an apparent decoupling of the tread from the web and hub. Second, there is significant modal character in the axial impedance (many resonances and antiresonances), much more than in the radial impedance. This is particularly interesting because squeal noise, which will be discussed in later sections, is known to be composed of pure tones. The strongly resonant character of the wheel under axial forcing, seen in Fig. 2.1-10, is consistent with the view that squeal noise is excited by crabbing, as described in Sec. 1 (which would result in axial forces being applied to the wheel tread). On the other hand, roar noise, which is known to be broadband in character, is believed to be excited by the roughness on the wheels and rails, which would result mainly in radial forcing. The more smoothly varying impedance of Fig. 2.1-9 helps to explain why if the wheel contributes to roar noise no pure tones are present as with squeal.

The low-frequency (<1000 Hz) character of the radial wheel impedance is relatively easy to model. The impedance rises as ω to the first power, which is definitely mass-like. If we examine the track in Fig. 2.1-6, we find that the wheel
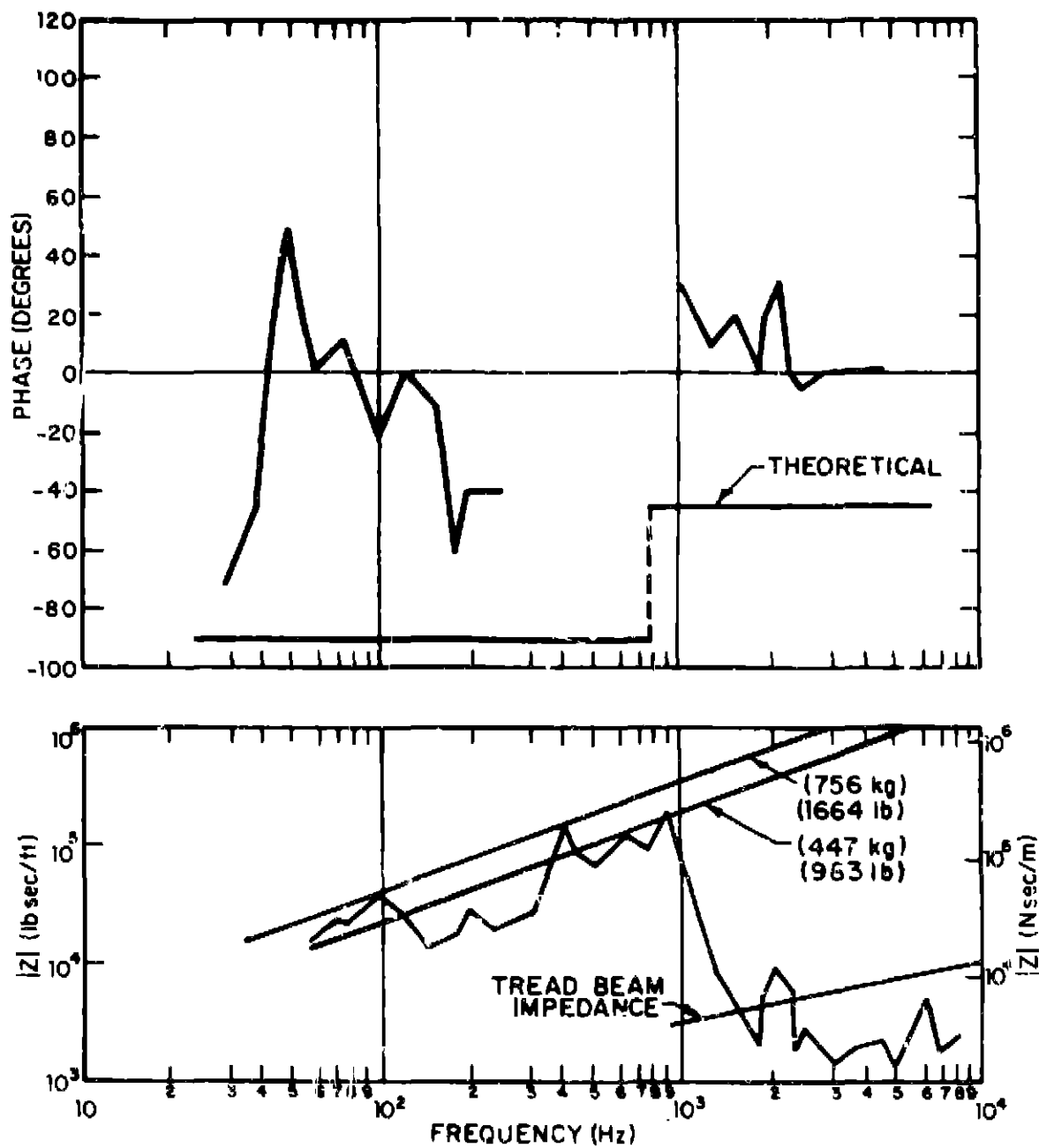
FIG. 2.1-3 RADIAL IMPEDANCE OF A 36 IN. (.91 m) DIAMETER
RAILROAD WHEEL.
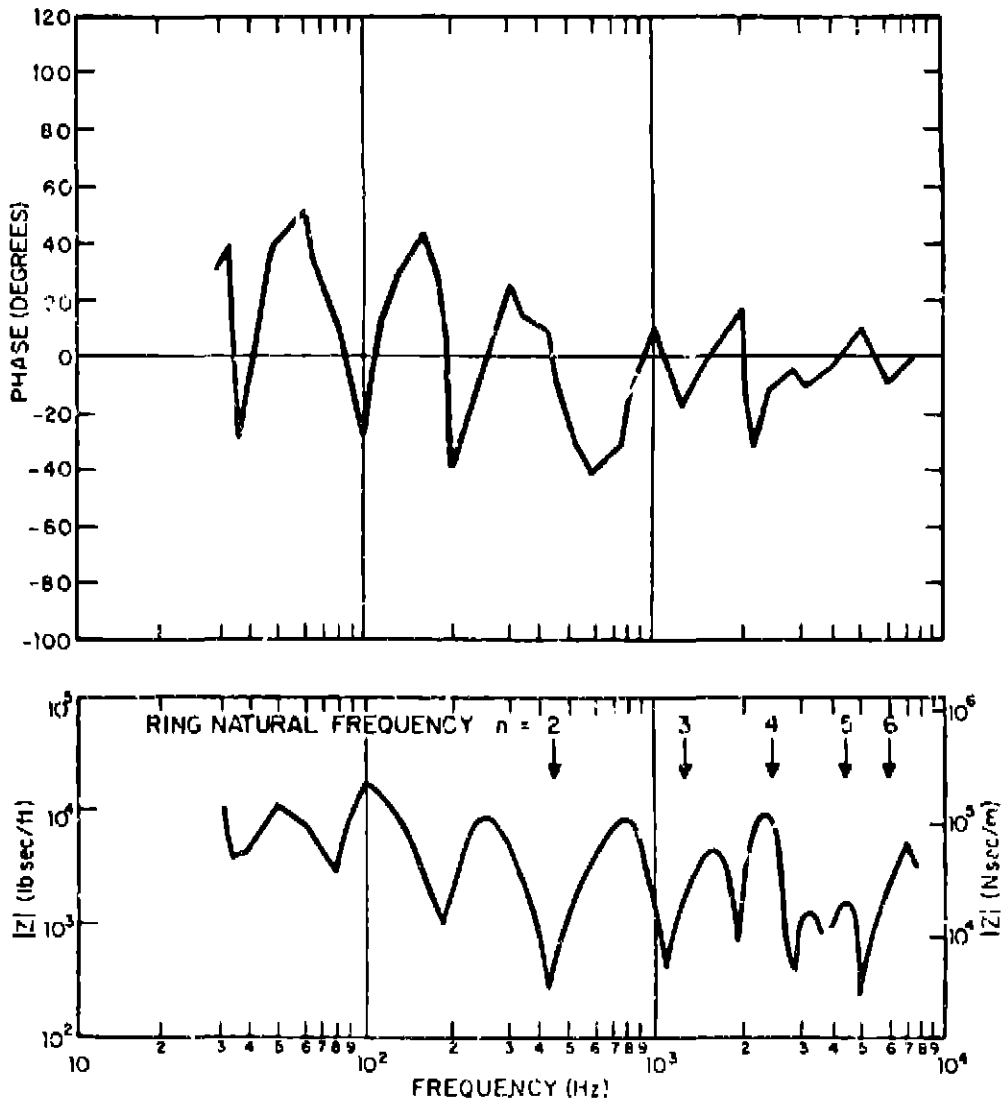
FIG. 2.1-10 AXIAL IMPEDANCE OF A 36 IN. (.91 m) DIAMETER RAILROAD WHEEL

(-750 lb; -340 kg) is attached to an axle (700 lb; 318 kg), a
bearing box (375 lb; 170 kg), and an equalizer bar (950 lb;
430 kg). The total effective mass* of 1664 lb (756 kg) results
in too high an impedance. If we take just the mass of the
wheel and 1/3 of the axle mass (983 lb; 447 kg), this figure
fits the data quite well. Apparently the bearing provides some
isolation between the wheel and the bearing box and equalizer
at high frequency.

The radial impedance above 1000 Hz is more difficult to
model. In fact, the radical change in impedance caused suffi-
cient concern that the measurement was repeated on a 14 in.
(0.35 m) running tread diameter wheel. The wheel was rested on
its hub on a metal block and the impedance measured by the same
method used to measure the larger wheel. Figure 2.1-11, which
shows the resulting impedance, is remarkably similar in charac-
ter to Fig. 2.1-9, except that the drop in radial impedance
occurs at a slightly higher frequency. This difference is con-
sistent with the fact that the 14-in. (0.35 m) diameter wheel
is smaller and stubbier than the 36-in. (0.91 m) diameter wheel.

We are confronted with two difficulties concerning the
measured radial impedance above 1000 Hz: first, in explaining
and predicting the occurrence of the sudden drop in impedance;
second, in predicting the magnitude of the impedance after the
drop. What appears to be happening is that the tread becomes
decoupled from the web and hub. This decoupling does not ap-
pear to be associated with any circular plate resonance of the
web of the wheel, since the break frequency[†] changes only by

_____ ____

*Since the axle and equalizer are fixed at the ends, not at-
tached to the driven wheel, their effective mass is only 1/3
of their true mass.

[†]The break frequency is the frequency at which the wheel imped-
ance abruptly drops.
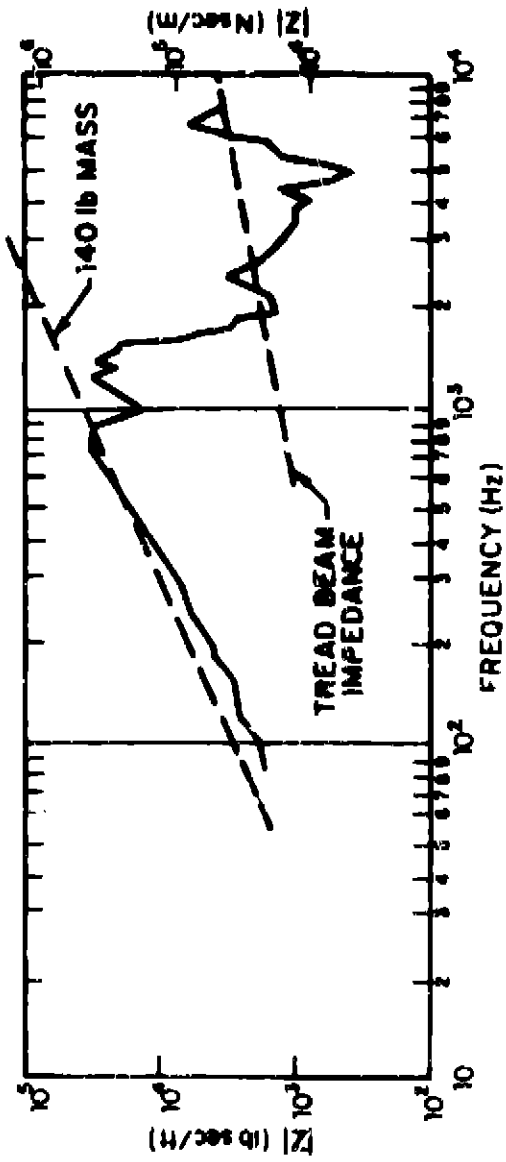
FIG. 2.3-11 RADIAL IMPEDANCE OF A 14 IN. (.35 m) DIAMETER RAILROAD WHEEL.

about 50% for a factor of 2.5 change in radius of the wheel.* However, since the break frequency changes so little for large changes in wheel size, it is reasonable as a first approximation simply to take the break frequency as ~1000 Hz for all standard size transit car wheels.

Analytically modeling the radial impedance above 1000 Hz presents some problems. In the limit at very high frequency, one would expect the impedance to approach that of an infinite beam with the same cross section as the tread; i.e.,

$$Z_W = \rho_\ell (\omega \kappa c_\ell)^{\frac{1}{2}} (1-j) , \qquad (2.1-4)$$

where c_ℓ is the compressional wavespeed in the material and κ is the radius of gyration. This formula gives predictions of the impedance amplitude that are at least the same order of magnitude as the data in Figs. 2.1-9 and 2.1-11[†], although the phase in Fig. 2.1-9 is poorly matched by this model. We will use this simple model in future calculations as a first approximation, bearing in mind that at certain frequencies some discrepancy between impedance prediction and measurement may exist.

The highly resonant character of the wheel makes the axial impedance quite difficult to model analytically, since a

---

*The web thickness of the 14 in. (0.35 m) and 26 in. (0.91 m) diameter wheels are nearly the same.

[†]The 14 in. (0.35 m) diameter wheel I studied has having a rectangular tread cross section of 4 in. (10 cm) wide by 1 in. (2.54 cm) thick. The 26 in. (0.91 m) diameter wheel I modeled as having rectangular cross section 4 in. (10 cm) wide by 1.5 in. (3.8 cm) thick. Note that standard 26 in. (0.91 m) diameter wheels have a 2.75 in. (7 cm) tread width. The 1.5 in. (3.8 cm) dimension was derived from a part drawing of the wheel in question.

detailed knowledge of the damping would be required for accurate
prediction at resonances. In addition, the geometric complex-
ity of most transit wheels makes prediction of their mechanical
response quite difficult. Stappenbeck (1954) has shown that
the resonance frequencies of a wheel vibrating in the axial
direction will have the same relation to one another as the
resonance frequencies of a ring vibrating out of its plane.
The resonance frequencies of a ring are given by

$$\omega_{ring} = \frac{\kappa c_\ell}{a^2} \sqrt{\frac{n(n^2 - 1)}{n^2 + 1 + \mu}}$$

where a is the ring radius, κ its radius of gyration, μ Poisson's
ratio, c_ℓ the compressional wavespeed in the material, and
n the circumferential wavenumber. Taking the ring cross section
to be a 5.5 in.× 1.5 in. (14 cm × 3.8 cm) rectangle approximat-
ing the tread cross section of the 36 in. (0.91 m) diameter
wheel, we obtain the ring natural frequency predictions shown
in Fig. 2.1-10. Unfortunately, many natural frequencies are
not predicted by this technique and at high frequencies the
predictions differ significantly. Fortunately, the axial im-
pedance is of importance primarily in regard to squeal and, as
we shall see in later sections, detailed predictions of the
wheel impedance are not required in order to predict squeal
noise.

2.1.2 Response

As mentioned previously, one must determine how the vari-
ous parts of the geometrically complex wheel and rail respond
if one is to predict the noise radiated by the wheel and rail.
For the rail one must also know the length of rail that

participates in the vibration in order to calculate the attenuation of vibration with distance from the point of excitation.

Railroad Rails — Head, Web, and Foot Response

To examine the rail response to point excitation such as occurs in its interaction with a wheel, we performed measurements on a 20-ft (6.1 m) section of AREA-100 rail. The rail was supported every 2 ft (0.61 m) along its length by resilient pads which in turn rested on a concrete floor. No attempt was made to simulate the stiffness of resilient fasteners used in transit authority operations, because in the frequency range of interest for acoustic radiation, the rail responds essentially independently of the fastener stiffness. The rail was excited by a 50-lb (225 N) capacity electronic shaker attached to the rail head. First, the shaker was oriented so as to force the rail vertically (to simulate the force one would expect from microroughnesses or impact at joints). Then, by attaching the shaker to the side of the rail head, we excited the rail horizontally (to simulate the force from crabbing or flange impact). The rail response was measured at five positions on the head, five positions on the web, and five positions on the foot by means of an accelerometer.

The rail response (a 5-point spatial average) on the head, web, and foot* for vertical excitation is shown in Fig. ...-12a. Only relative acceleration levels are important here, because the shaker force was not kept constant as the frequency load changed. The vertical acceleration of the head and foot are

---

*For all measurements the accelerometer was located in the center of the web for web acceleration and halfway between the web and the edge of the foot for the foot accelerations.
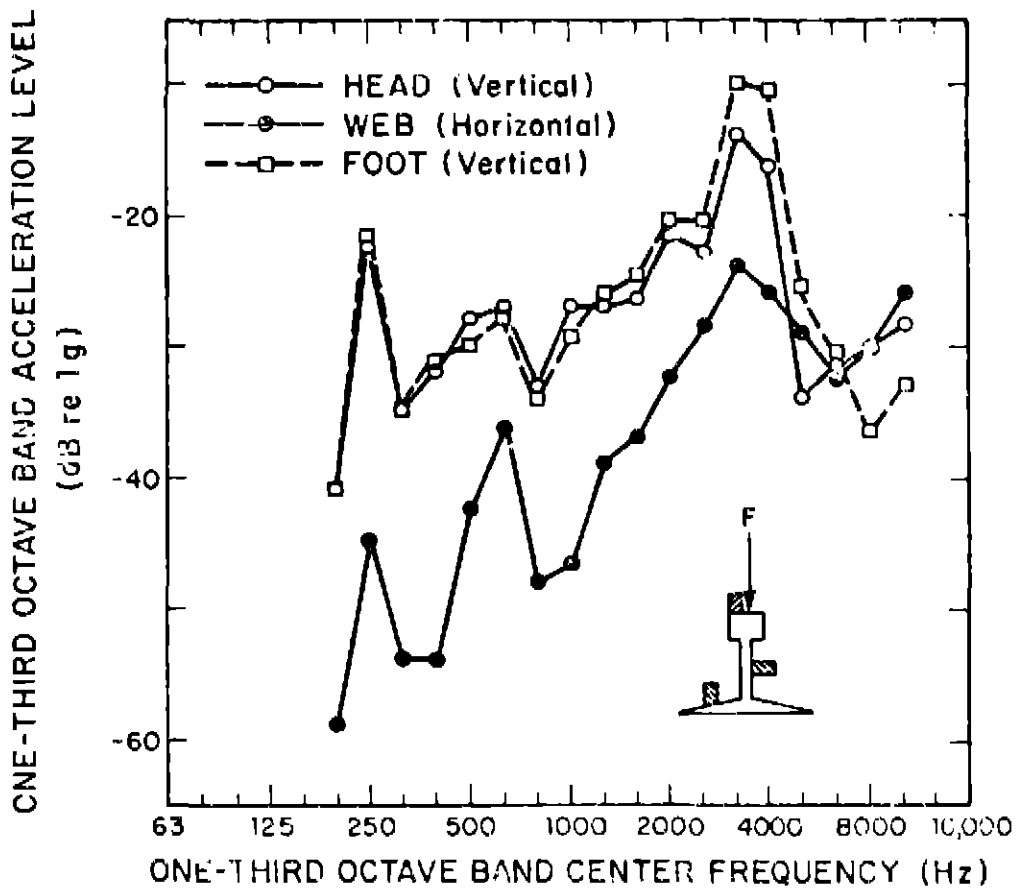
FIG. 2.1-12a. RAIL RESPONSE TO VERTICAL EXCITATION.

essentially the same up to 3000 Hz and the web acceleration in
the horizontal direction normal to the plane of the web is
negligible to beyond 4000 Hz. This behavior implies that the
rail moves essentially as a simple beam. At about 3000 to
4000 Hz, there is an apparent resonance of the foot on the web
stiffness in which the foot response exceeds the head response
by about 5 dB.

The rail acceleration response for horizontal excitation
of the rail head is shown in Fig. 2.1-12b. The horizontal ac-
celeration of the head and the web are essentially the same up
to 2500 Hz and the vertical acceleration of the foot is
negligible up to about 2000 Hz. Except for a peak at 3150 Hz,
where the foot response dominates, the head, web, and foot re-
spond almost identically from 2500 to 5000 Hz where the web
begins to dominate the response. This response pattern is some-
what more complicated than for vertical forcing; however, at
low frequencies the pattern is what one would expect if the
rail were moving as a simple beam in the horizontal direction.

Railroad Rails – Attenuation of Vibration Along Their Length

The attenuation of vibration along the length of a rail as
a function of distance away from the point of excitation has
been measured by Haake (1963) on the rail described in Table
2.1 resting on ties and ballast with a tie spacing of 2.1 ft
(0.65 m). Additional attenuation measurements were performed
during the course of this program on the tie and ballast sup-
ported rail at the Pullman Standard test track at the Champ
Carry Technical Center, Hammond, Indiana (see Sec. 3). A
straight section of jointed rail with a tie spacing of 2 ft
(0.61 m) was excited by an electromagnetic shaker driven with
broadband noise. For vertical excitation the entire
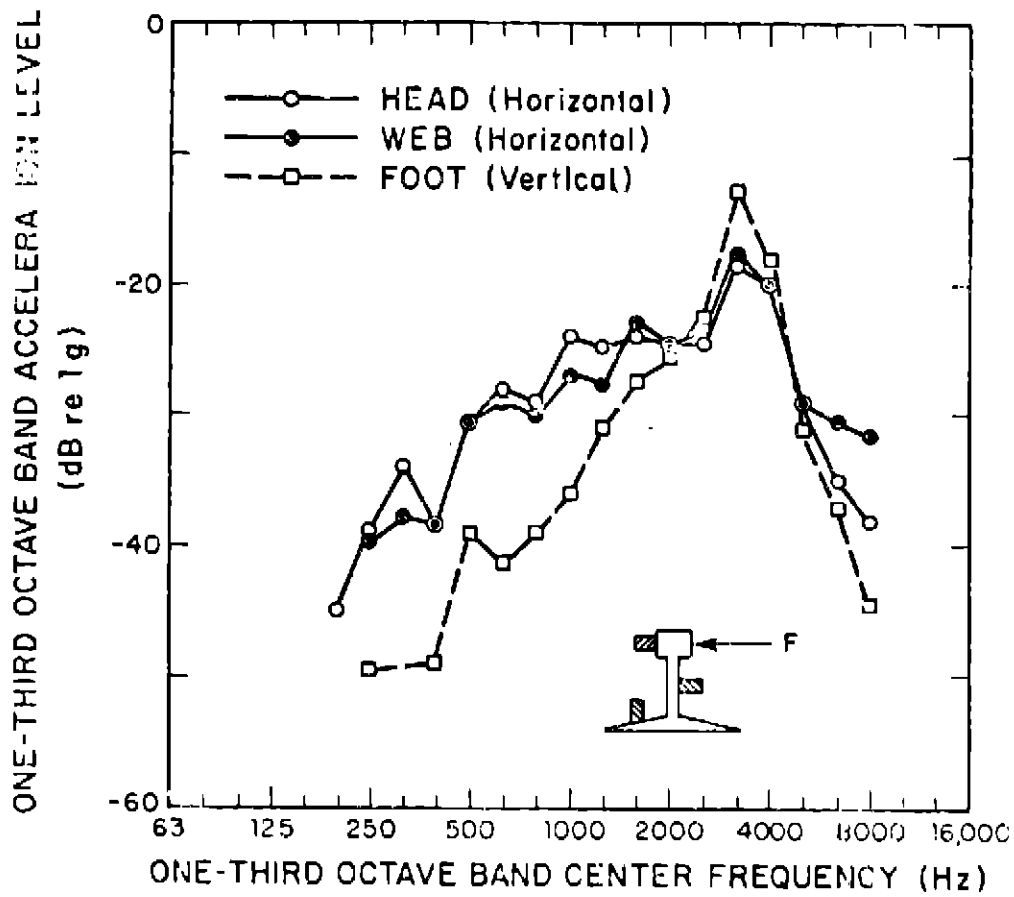
FIG. 2.1-12b RAIL RESPONSE TO HORIZONTAL EXCITATION

acceleration on the rail head was measured at several distances
from the shaker up to and across a rail joint. For horizontal
excitation similar measurements of the horizontal acceleration
of the rail head were made. The decrease in the octave band
level along the rail relative to that level at the shaker is
shown in Figs. 2.1-13 and 2.1-14. The last point in those
figures, at 16 ft (4.9 m), is at the rail joint on the excita-
tion side.

For those cases in which a linear approximation to the
data can be made, i.e., in dB/m, the results are plotted in
Figs. 2.1-15 and 2.1-16 for comparison with Naake's results.
The vertical attenuation at low frequencies (Fig. 2.1-15)
agrees well with Naake's results, but at high frequencies (be-
tween 1 and 2 kHz) the results from the Pullman test track do
not show the increasing attenuation with frequency found by
Naake. The attenuation of horizontal vibration in Fig. 2.1-16
was difficult to compare with Naake's results since above 500
Hz (see Fig. 2.1-14) the data are not easily fitted by a
straight line.* We should point out, though, that Naake per-
formed his measurements over a very long length of rail (over

_____ _____

* It is curious to note that, in all the cases shown, the accel-
eration level at the rail joint is higher than one would ex-
pect with a straight-line approximation to the decay of the
vibration. It appears as though the end of the rail at the
joint were like the free end of a beam. This is consistent
with the large attenuation across the rail joint shown in
Table 2.3, suggesting that the two rails are essentially de-
coupled at their ends. The fact that the rail impedance
measurements did not show this across the joint, the impedance
at a rail joint is essentially the same as the impedance at
the center of the rail, may be due to the fact that the mas-
sive joint bar increases the impedance at the joint suffi-
ciently so that the change of impedance in frequency that one
would expect at the rail joint were more like that in the center of the
rail (i.e., the rail acts like an oh and appears to be a semi-
infinite beam rather than an infinite beam) is obscured.
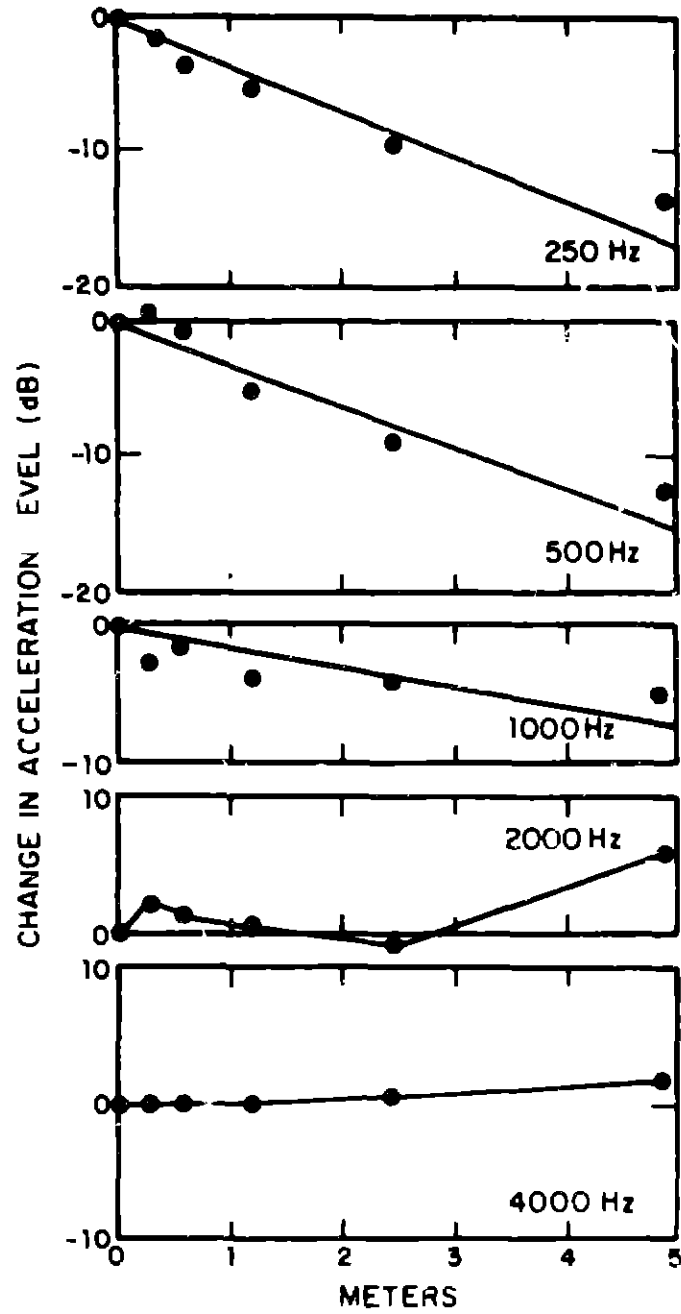
FIG. 2.1-13   OCTAVE BAND VIBRATION LEVEL VS DISTANCE ALONG
A RAIL EXCITED VERTICALLY
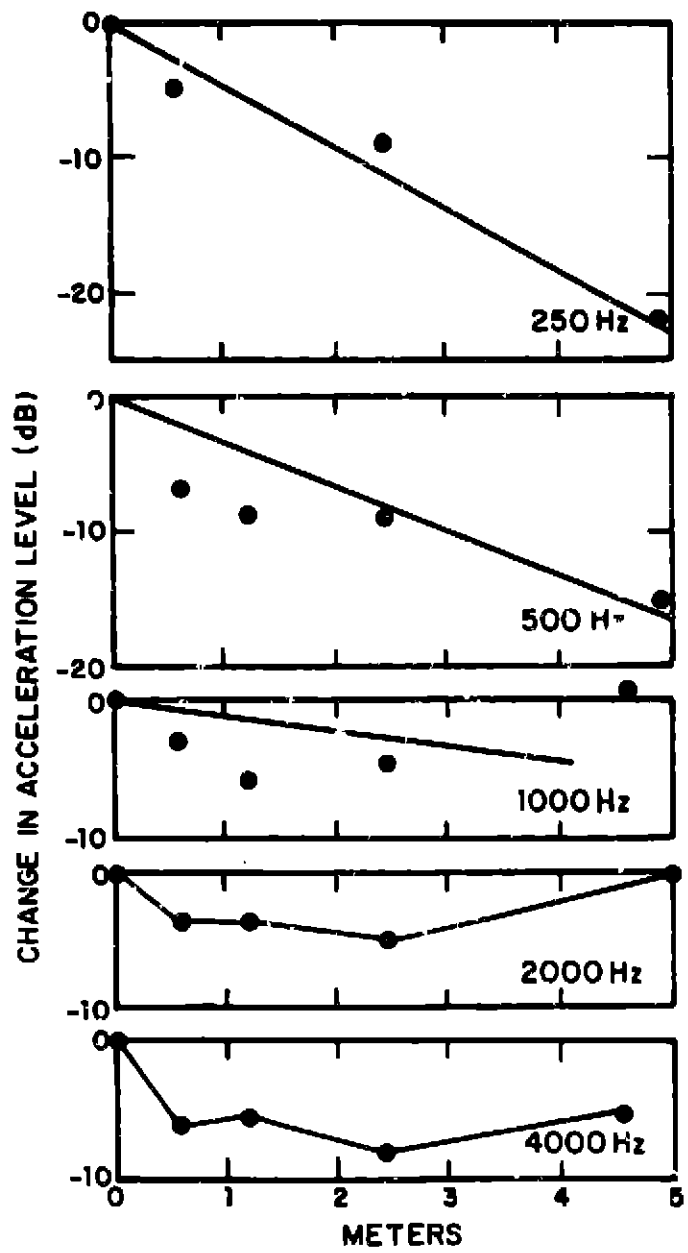
FIG. 2.1-14   OCTAVE BAND VIBRATION LEVELS VS DISTANCE ALONG
A RAIL EXCITED HORIZONTALLY
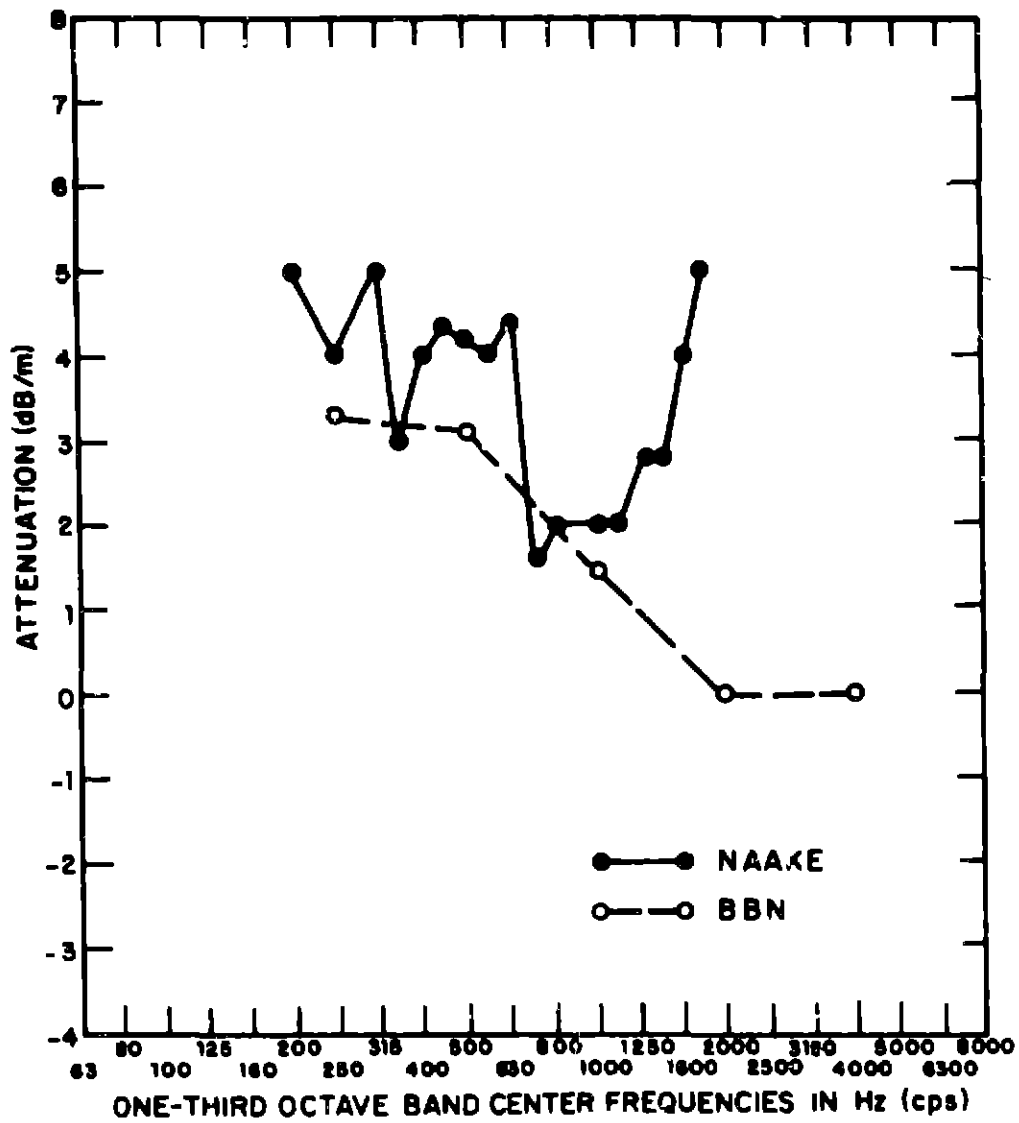
FIG. 2.1-15 VIBRATION ATTENUATION WITH DISTANCE ALONG A SINGLE
LENGTH OF JOINTED RAIL EXCITED VERTICALLY

41
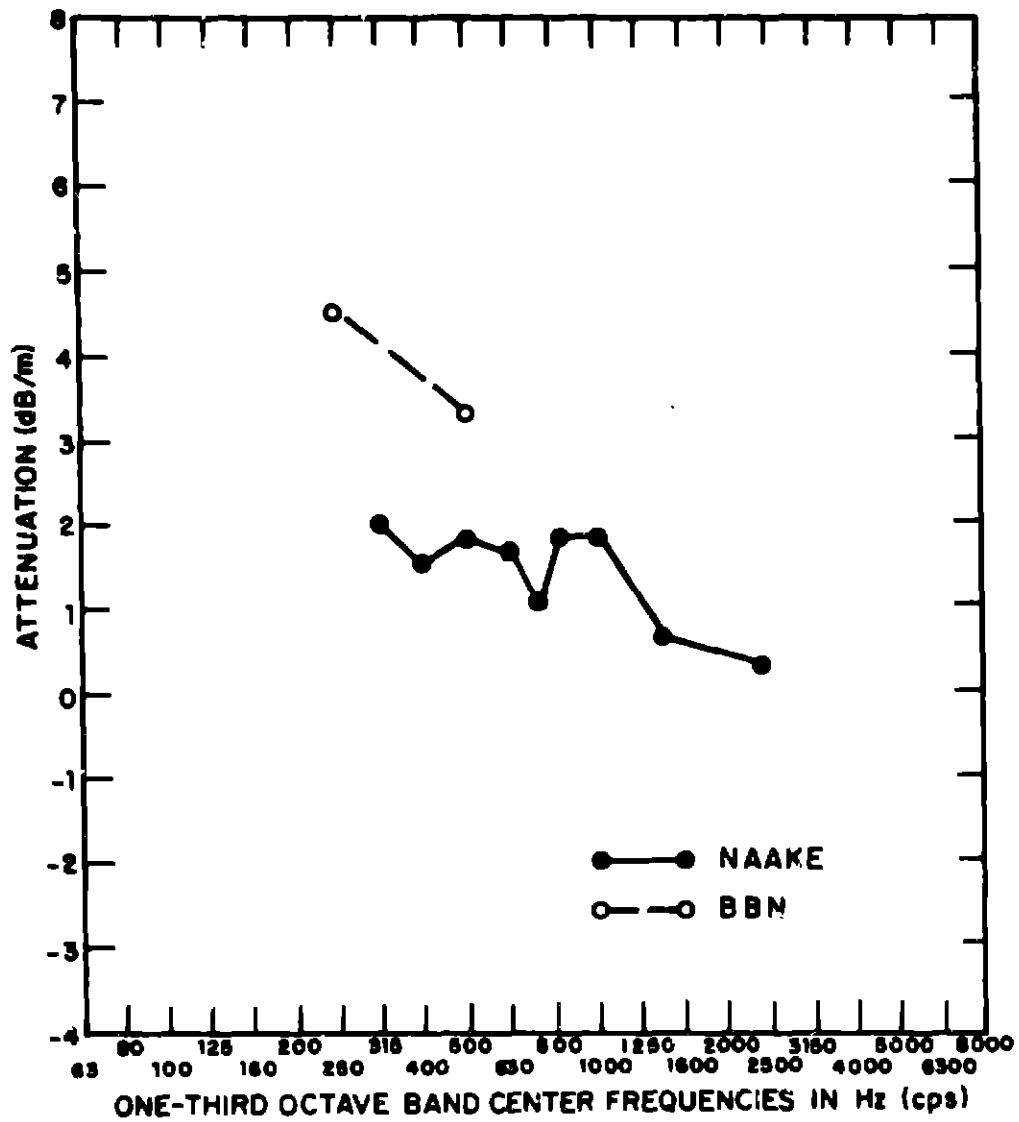
FIG. 2.1-16 VIBRATION ATTENUATION WITH DISTANCE ALONG A SINGLE
LENGTH OF JOINTED RAIL EXCITED HORIZONTALLY

98.3 ft (30 m)] and scatter of the points in excess of 5 dB
about the straight line approximation was common. If one allows
for that much scatter, a straight line could easily be fitted
to the data at frequencies above 500 Hz in Fig. 2.1-14. For
example, at 1000 and 2000 Hz one would obtain an attenuation of
around 1 dB/m, which agrees well with Naake's results in Fig.
2.1-16. Unfortunately, though, the low-frequency results at
the Pullman Standard test track show considerably more attenua-
tion than Naake measured. In all likelihood discrepancies such
as these are due to differences in the two track beds.

Both Naake's data (except the vertical attenuation data in
the 1000 to 1700 hz range) and the data in Figs. 2.1-13 and
2.1-14 suggest that below 1000 Hz rail vibration is confined to
a region of 10 ft (~3 m) to each side of the excitation point
and that above 1000 Hz (to within an accuracy of about 5 dB)
the attenuation can as a first approximation be neglected on
the approximately 50 ft (15.3 m) length of rail confined between
the two bogies supporting a typical transit car.

In cases in which rail joints are present, additional at-
tenuation can occur across the joint. Table 2.3 gives Naake's
results for the attenuation of horizontal vibration across a
joint in the rail of Table 2.1 mounted on tie and ballast, as
well as results for the attenuation of vertical and horizontal*
vibration across a rail joint measured at the Pullman Standard
test track. In general terms, below 1000 Hz the attenuation
across the joint is negligible; above 1000 Hz but below 8000 Hz,
it may be significant. *This high attenuation across rail joints*

---

*Because of instrumentation problems, data for the attenuation
 of horizontal vibration across the joint were obtained at only
 a few frequencies.

TABLE 2.3.   VIBRATION ATTENUATION ACROSS A RAIL JOINT.

Horizontal Vibration   (Naake, 1953)

Frequency (Pure Tone)	Attenuation
430 Hz	~ 0 dB
1500 Hz	12 dB
2350 Hz	22 dB

Vertical Vibration   (Pullman Standard Test Track)

Frequency (Octave Band)	Attenuation
250 Hz	~2.5 dB
500 Hz	~1.5 dB
1000 Hz	4 dB
2000 Hz	12 dB
4000 Hz	8 dB
8000 Hz	6.5 dB

Horizontal Excitation (Pullman Standard Test Track)

Frequency (Octave Band)	Attenuation
1000 Hz	10 dB
2000 Hz	15 dB
4000 Hz	11 dB
8000 Hz	4 dB

*at high frequency and the large attenuation of vibration with
distance along the rail at low frequencies imply that on jointed
rail vibration is confined to the excited rail.*

Railroad Wheels — Tread and Web Response

To examine the relative response of the tread and web of a
railroad wheel to axial and radial excitation at the tread
face, such as would occur when the wheel rolls on the rail, we
took measurements on a wheel set [two wheels and an axle with
30 in. (0.76 m) diameter wheels] supported by resilient pads
at two points on the axle and the tread. One wheel was excited
with an electromagnetic shaker driven with broadband noise.
The shaker was attached to a stud that was glued to the center
of the face of the tread for radial excitation and to the side
of the tread for axial excitation. The acceleration was re-
corded at five points on the face of the tread in the radial
direction, at five points on the side of the tread in the axial
direction, and at five points in the center of the web in the
axial direction, all under the same forcing. The average ac-
celeration in 1/3-octave bands on each of these three parts of
the wheel is plotted in Fig. 2.1-17 for radial forcing and
Fig. 2.1-18 for axial forcing. Note that it is only the rela-
tive accel   .tion levels in these figures that are of interest
because the applied force was not held constant as a function
of frequency.

In Fig. 2.1-17 the most striking result is that the aver-
age acceleration levels resulting from radial forcing are es-
sentially equal on the face of the tread and the center of the
web. This result greatly simplifies the calculation of wheel
response or radiation due to radial forcing, since once the
acceleration levels at the face of the tread are known, the
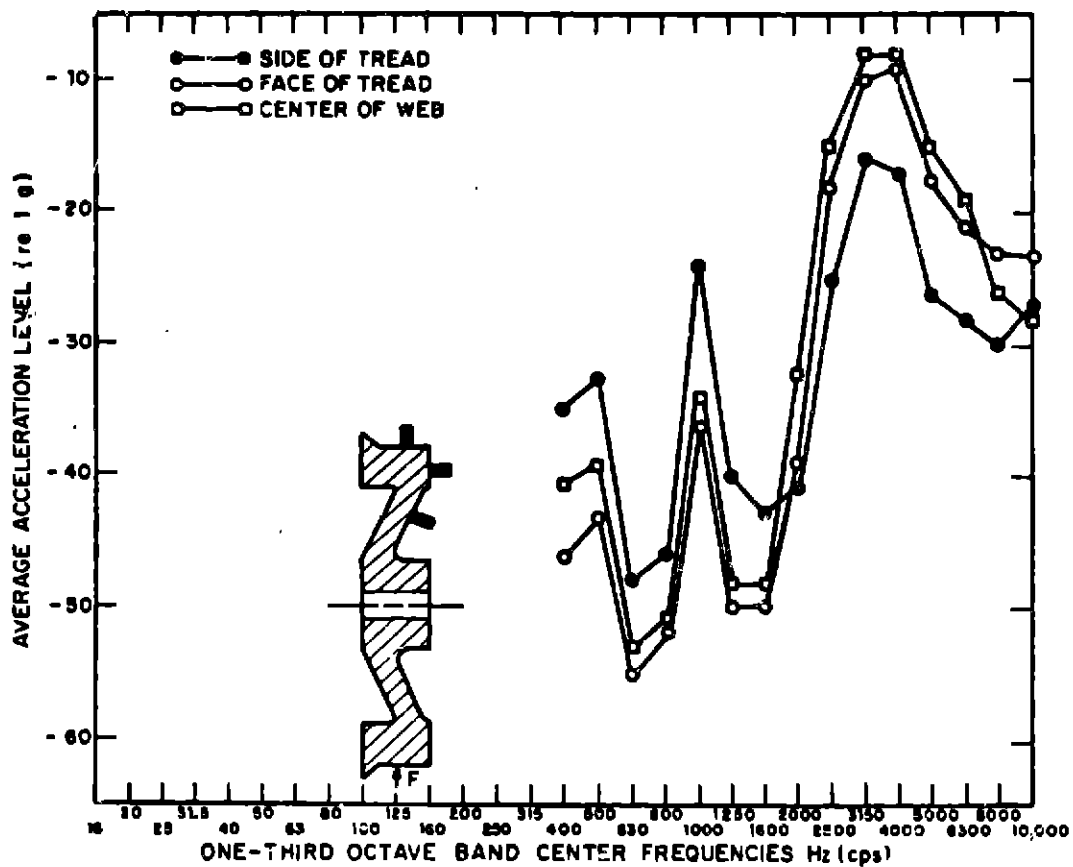
FIG. 2.1-17   WHEEL RESPONSE TO RADIAL FORCING
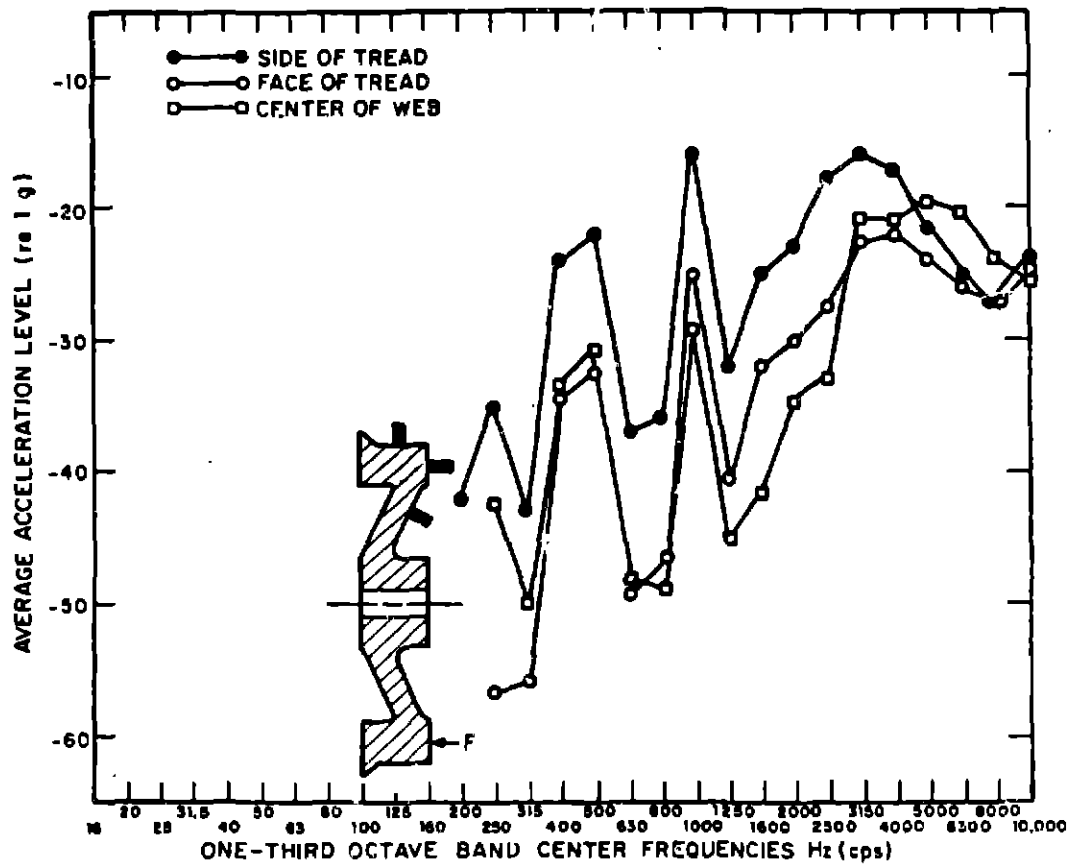
FIG. 2.1-18 WHEEL RESPONSE TO AXIAL FORCING

levels on the web (the part of the wheel with the greatest
radiating area) are also known. Figure 2.1-17 also shows that
the acceleration levels on the side of the tread in the axial
direction (at right angles to the forcing direction) are higher
than the levels on the face of the tread up to about 2000 Hz.
This result implies that the tread is rocking considerably,
which would also account for the close coupling between the
tread and the web.

The response shown in Fig. 2.1-18 to axial forcing cannot
be so simply modeled as the response to radial forcing. Again
it is apparent that the center of the web and the face of the
tread have approximately the same acceleration levels, but the
side of the tread where the wheel is forced has 7 to 10 dB
higher acceleration levels than the center of the web. This
result suggests a cantilever-like motion of the wheel disk about
its hub. For example, the static deflection at the center of
a cantilever beam due to a force applied to its free end is
about 10 dB below the deflections at the free end.

2.1.3 Radiation efficiency

To predict the transformation of the mechanical response
of the wheel or rail into acoustic radiation, it is necessary
to know the radiation efficiency, σ, of each. Knowledge of the
radiation efficiency allows one to predict the sound power
radiated W as

$$W = \sigma \rho c A < v^2 > , \qquad (2.1-5)$$

where ρc is the acoustic impedance of air, A is the radiating
area of the body in question, and $<v^2>$ is the velocity squared
of the body averaged over time and A. In this section we

describe a number of measurements and analytical models for de-
fining σ for railroad wheels and rails.

Railroad Rails

Analytical calculation of the radiation efficiency of a
structure with as complicated a cross section as a rail would
be an extremely difficult task. However, rails do have several
characteristics that allow us to make a number of simplifica-
tions. First, the coincidence frequency of most rails of in-
terest is low, below 100 Hz; second, rails are generally long
compared to an acoustic wavelength for the frequency range of
interest here; and, lastly, the response results of Sec. 2.1.2
suggest that at least at low frequency the rail responds like
a simple beam to both vertical and horizontal excitation.

By treating the rail as a cylindrical beam, we may use an
existing analytical formulation (see Bailey and Fahy, 1972) for
the radiation efficiency under the assumptions that the beam is
above coincidence and long compared to an acoustic wavelength.
The expression that results for the radiation efficiency is

$$\sigma(r) = \frac{W}{\rho c(2r)L\langle v^2 \rangle} = \{kr[\,|J_1'(kr)|^2 + |Y_1'(kr)|^2]\}^{-2} \, , \quad (2.1-6)$$

where r is the beam radius, L is the length, k is the acoustic
wavenumber, J_1 and Y_1 are Bessel functions of the first and
second kind respectively of order 1, and

$$J_1'(z) = \frac{\partial}{\partial z} J_1(z) \, , \text{ etc.}$$

We apply Eq. 2.1-6 to calculate the rail radiation effi-
ciency for the horizontal forcing of the rail by taking the

cylinder diameter equal to the rail height (Eq. 2.1-6 with
r = rail height/2). For the vertical forcing of the rail, we
model the rail as two cylinders vibrating independently and with
the same amplitude such that the power radiated is the sum of
that radiated from each. The diameter of one cylinder equals
the rail head width and the diameter of the second equals the
rail foot width.

The resulting expression for the radiation efficiency be-
comes

$$\sigma_{\substack{\text{vertical}\\\text{forcing}}} = \frac{\sigma(r_H)r_H + \sigma(r_F)r_F}{r_H + r_F} , \qquad (2.1\ 7)$$

where $\sigma(r_F)$ and $\sigma(r_H)$ are Eq. 2.1-6 evaluated for $r = r_F$ and
r_H respectively, where r_H is one-half the rail head width and
r_F is one-half the rail foot width. Since these analytical
models are only approximations, it is essential that we compare
them with measurements to validate their use.

We measured the rail radiation efficiency on the same 20-ft
(6.1 m) section of AREA-100 rail mounted as described in Sec.
2.1.2 in a reverberant chamber (~3100 cu ft; 86 8 m³). The
chamber was calibrated so that the power radiated by the rail
could be inferred from measurements of the sound pressure level
in the chamber. The rail was excited as described in Sec. 2.1.2
at the rail head in both the vertical and horizontal directions.
The sound pressure level in the room was monitored at three
positions and a rotating vane was employed to enhance spatial
averaging of the sound pressure in the room. The origi al rail
was too long (39 ft; 11.9 m) and had to be cut to fit into the
reverberant chamber. However, its resulting length (~20 ft;
6.1 m) was greater than an acoustic wavelength at the lowest

frequency of interest and, hence, this shortening should have no effect on the radiation efficiency. The fact that the rail response is quite narrowband (distinct resonances can be seen in the rail response up to about 4 kHz with 1/10-octave band analysis) does lead to some uncertainties in the resulting measurement of sound power when only three microphones are used. We anticipate uncertainties of no more than ±5 dB at around 500 Hz to no more than ±2 dB at 2000 Hz in our measurements of the power radiated.

The use of an electronic shaker to excite the rail requires quieting of the shaker so as to ensure that the power radiated is primarily from the rail itself. To do this we enclosed the shaker in a plywood box with 3/4 in. (1.9 cm) thick walls and lined the interior with a 2 in. (5 cm) thick layer of fiberglass. We checked the effectiveness of this treatment by attaching the shaker to a block of lead, enclosing the shaker and lead in the box, and driving the shaker with the same current levels used to excite the rail. We then measured the sound power level (PWL) and compared it with the PWL measured when the rail was excited.* Above 200 Hz the noise from the shaker was on the order of 10 dB or more below the noise from the rail.

In order to reduce the data by means of Eq. 2.1-5, we require the mean square rail velocity $<v^2>$, the time-averaged sound power radiated W, and an appropriate measure of the radiating area of the rail. For both vertical and horizontal forcing of the rail, we take $\sqrt{<v^2>}$ to be the mean-square space-averaged rail head velocity. For vertical excitation, the area

---

*The average of the sound pressure level at the three microphone positions corrected for the room characteristic.

51

A is taken as the sum of the rail head and rail foot widths times the rail length, and for horizontal excitiation A is the rail height times the rail length. A comparison of these measurements with the analytical prediction described above is shown in Figs. 2.1-19 and 2.1-20.

For vertical excitation, the agreement between theory and measurement in Fig. 2.1-19 is quite good, except in the vicinity of 5000 Hz where the fact that the foot response dominates the head response tends to make measured estimates of σ_R based on the head response too high. Note that at high frequency the theoretical estimate of 10 log σ_R tends to be 2 dB (the cylinder radiates from both sides) and that in general the measured radiation efficiency is somewhat greater than the theoretical estimates, suggesting that the theory would tend to underestimate the rail radiation.

For horizontal excitation, the agreement in Fig. 2.1-20 between theory and measurement is again good. In the 2500 to 4000 Hz range, the measured values are high, because the foot response dominates at these frequencies and basing the calculation of σ on the head response tends to overestimate the radiation efficiency.

We see then that rails are very efficient radiators of acoustic energy above 500 Hz, coinciding well with those frequencies to which the ear is sensitive.

Railroad Wheels

Like rails, railroad wheels hav a very complex geometry that makes the analytical calculations of their radiation efficiency quite difficult. Fortunately, as with the rail, the
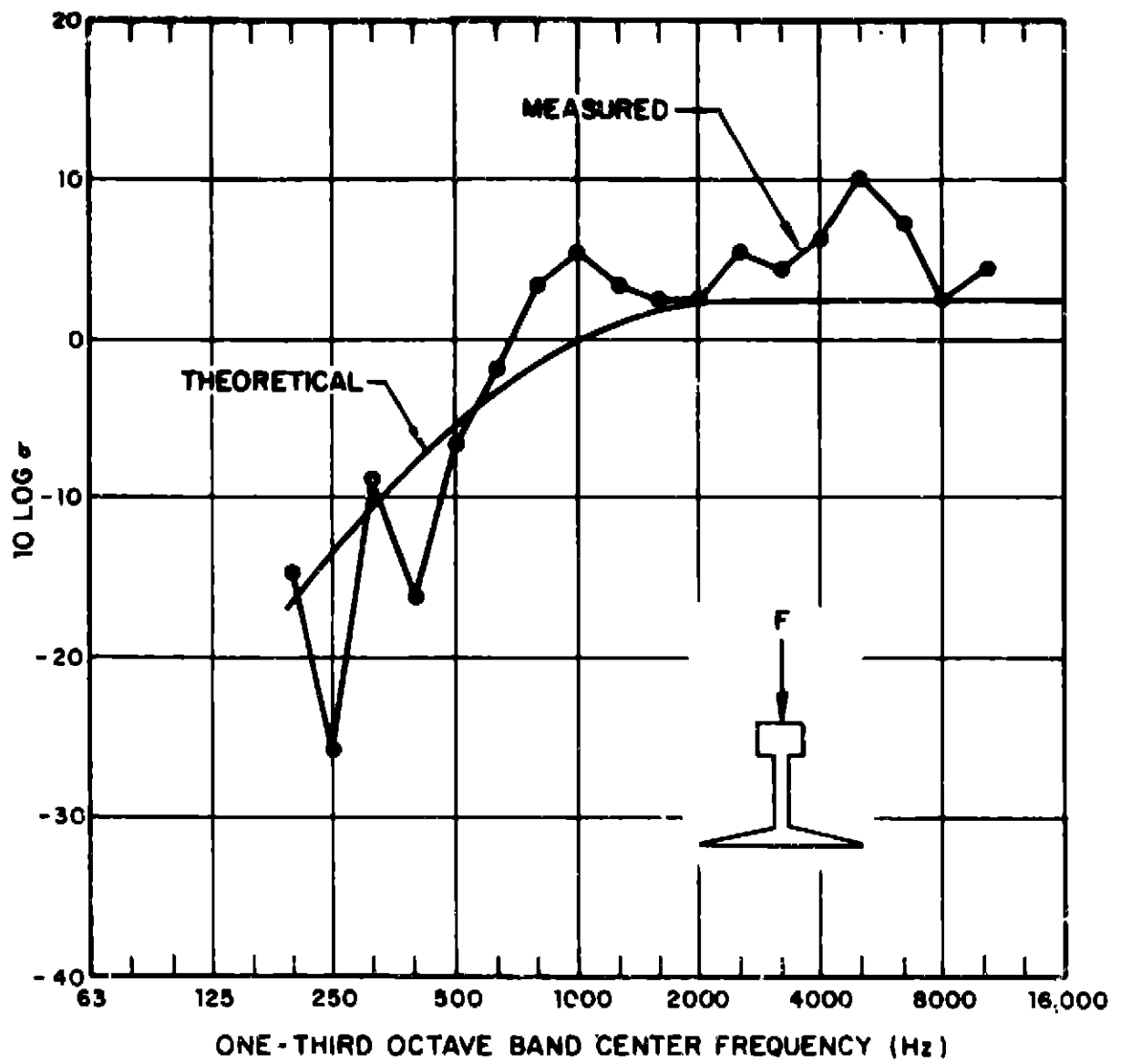
FIG. 2.1-19. RAIL RADIATION EFFICIENCY FOR VERTICAL EXCITATION.

53
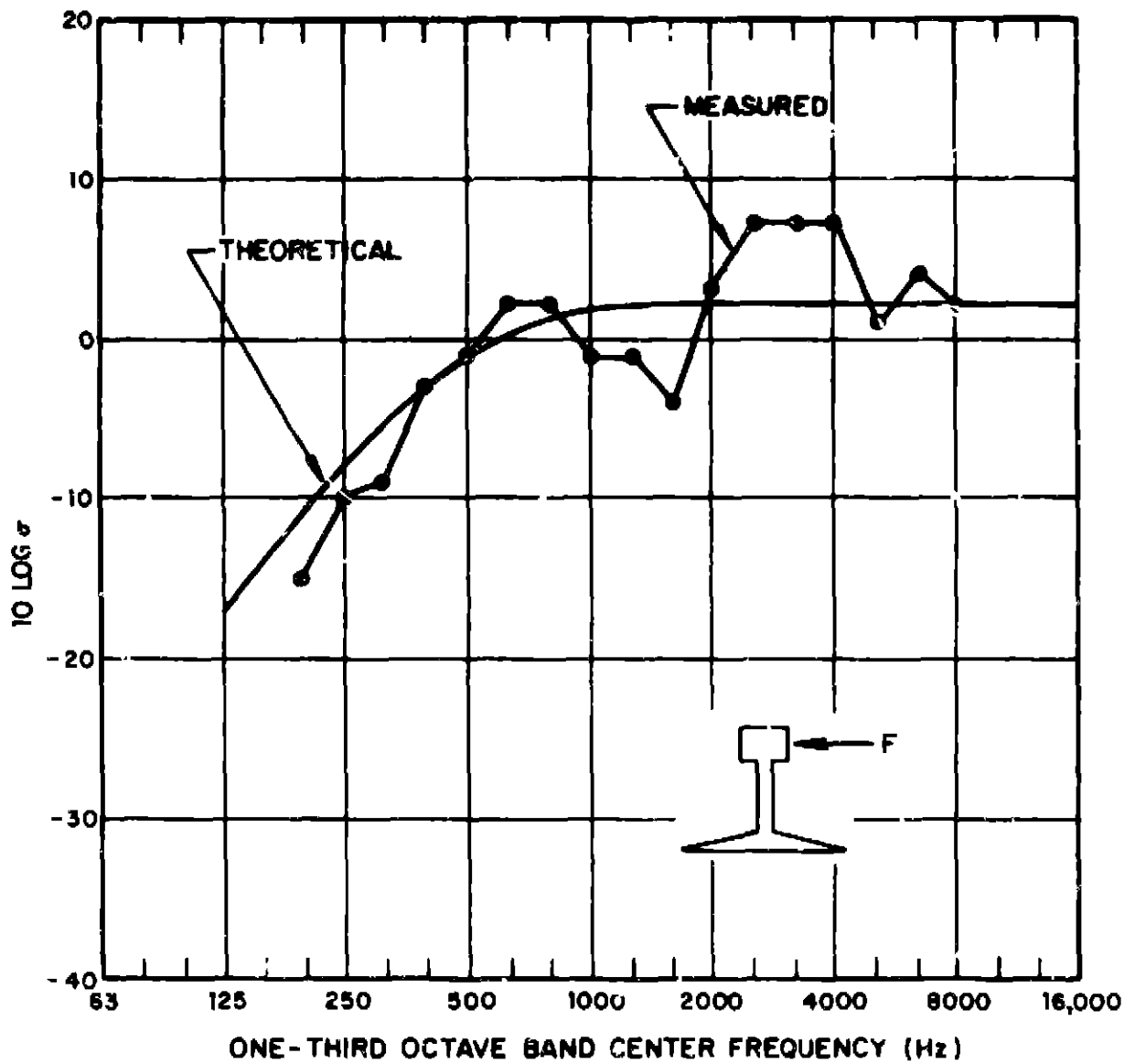
FIG. 2.1-20.   RAIL RADIATION EFFICIENCY FOR HORIZONTAL
EXCITATION.

wheel has some characteristics that allow a number of simpli-
fications to be made so that the radiation efficiency can be
calculated approximately. First, from the results of Sec.
2.1.2, it is known that the wheel moves significantly in the
axial direction for both axial and radial forcing, suggesting
that modeling the wheel as a disk might be appropriate. Sec-
ond, the coincidence frequency of the wheel is low (less than
100 Hz)[*], further suggesting that modeling the wheel as a rigid
unbaffled disk might be appropriate for estimating the radia-
tion efficiency. For a rigid unbaffled disk, the radiation
efficiency can be calculated for two limiting cases (see Morse
and Ingard, 1968)

$$\sigma_W \cong 2 \qquad , \qquad ka \gg 1$$

$$\sigma_W \cong 3(ka)^4 , \qquad ka \ll 1 , \qquad (2.1-8)$$

where k is the acoustic wavenumber and a the radius of the
disk. Note that if one uses Eq. 2.1-8 in Eq. 2.1-5 to estimate
the radiated power, the area A in the latter equation is πa^2.
The "2" in Eq. 2.1-8 for $ka \gg 1$ (one would ordinarily expect σ
not to exceed 1) indicates simply that the disk radiates from
both sides. For a 30 in. (0.76 m) diameter wheel, $ka \sim 2$ at
350 Hz, implying that for most of the frequency range of inter-
est here, $\sigma \cong 2$.

---

*This statement is based on the fact that vibration of the
wheel appears to be controlled by motion of the tread of the
wheel as if the wheel were a ring having the same cross sec-
tion as the tread. The web simply goes along for the ride.
The tread if modelled as a beam or ring in bending has a very
high wavespeed since it is very thick.

The above formulation is quite approximate and verification measurements of the wheel radiation efficiency are required. Such measurements were performed on a wheel set with 30 in. (0.76 m) diameter wheels. The axle of the wheel set was resiliently mounted at 2 points and placed in a semireverberant room (~10,000 cu ft) at the Pullman Standard Champ Carry Technical Center. The acceptance testing of the room is discussed in Appendix A.

The wheel was excited in the radial direction with an electromagnetic shaker attached to the tread face by means of a glued-on stud and in the axial direction with the shaker attached by the same means to the side of the tread. The shaker was enclosed in a plywood box with 3/4 in. (1.9 cm) thick walls lined with 2 in. (5 cm) of fiberglass to prevent radiation from the shaker itself contaminating the radiation from the wheel. To determine the contribution of the shaker to background levels, we attached the shaker to a block of steel, enclosed both in the box, drove the shaker with the same current used to excite the wheel, and measured the sound pressure level (SPL). The sound pressure level was negligible compared to the levels generated when the wheel was excited. The major problem with the wheel measurements at low frequency proved to be the high background sound levels, even though all measurements were performed at night. The major difficulty was that we could not excite the wheel sufficiently to produce high enough levels of noise to exceed the background levels at all frequencies of interest.

Four microphone positions in the room were used to obtain an average SPL (from which the power radiated could be calculated from the room calibration), and the average velocity level on the wheel was obtained from acceleration measurements at five positions on the web, face of the tread, and the side of the tread as described in Sec. 2.1.2.

Reducing the measured data to the radiation efficiency by means of Eq. 2.1-5 requires a radiating area and an average velocity of that radiating area. For radial forcing of the wheel, the average vibration level on the face of the tread was used for the velocity and πa^2, where a is the wheel radius, was used as the radiating area.[*] Although it would have been more consistent to use the average level on the web, the measurements of Sec. 2.1.2 show that head and web levels are essentially equal under radial forcing. Also, as we will show in later sections, the wheel and rail impedance will be used to predict the response at the wheel/rail interface. Consequently, it is convenient to relate the radiation efficiency to the response at the face of the tread.

Figure 2.1-21 shows the agreement of the measured data with the theory of Eq. 2.1-8. Below 400 Hz high background noise prevented our taking any reliable data.[†] Also, at several higher frequencies the presence of dips in the power radiated from the wheel (probably due to antiresonances in the wheel response) caused the background to be within a few dB of the measured levels from the wheel. In general, the data agree well with the theory, and a radiation efficiency equal to 2 appears valid throughout the frequency range of interest.

For axial forcing the wheel radiating area is again chosen to be πa^2 and the average velocity is taken to be that at the side of the tread. Although the results of Sec. 2.1.2 suggest

---

[*]Acceleration levels on the adjacent nonexcited wheel were sufficiently below the excited wheel levels that ignoring them introduces negligible error in the frequency range of interest here.

[†]Under axial forcing the wheel could be made to produce sufficient noise that levels well above the background could be obtained down to 250 Hz.
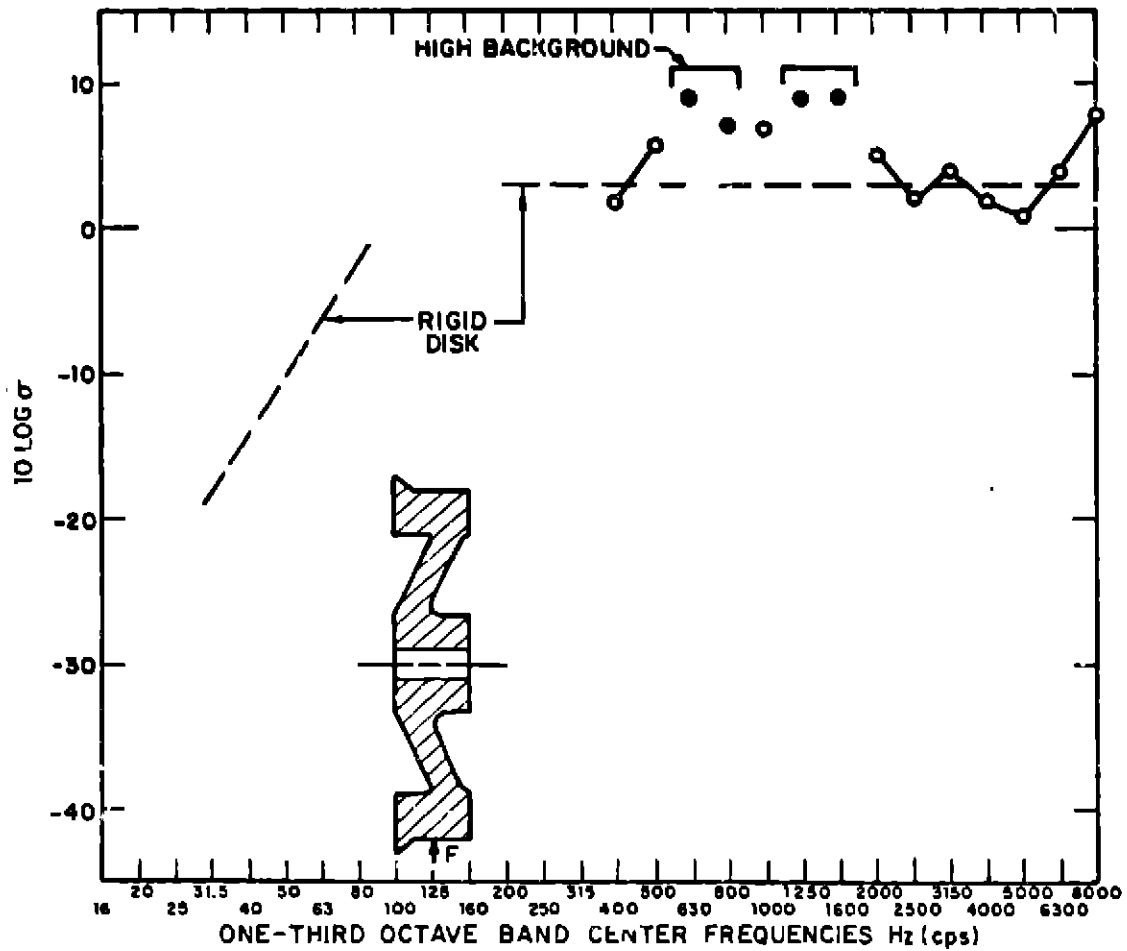
FIG. 2.1-21. WHEEL RADIATION EFFICIENCY FOR RADIAL FORCING.

that this velocity will overestimate the velocity on the web of the wheel due to the apparent cantilever-like motion of the tread and web about the hub, we find the agreement in Fig. 2.1-22 between the data and simple theory of Eq. 2 1-8 to be acceptable.

The above analyses and experiments result in a radiation efficiency model of the wheel that is quite convenient. With the average velocity of the wheel taken to be that of the wheel/rail interface and the radiating area taken to be πa^2, where a is the wheel radius, the radiation efficiency for the frequency range of interest here is simply

$$\sigma_W = 2 \ . \tag{2.1-9}$$

2.1.4 Directivity

Accurate calculation of the sound pressure level at a given distance R from a source requires a knowledge of the dire .ivity of the power radiated from the source, i.e., the variation of intensity with direction. If the source is an omnidirectional point source near the ground, then the mean square pressure $<p^2>$ at distance R from the source is easily related to the radiated power W by

$$<p^2> = \frac{\rho c W}{2\pi R^2} \ . \tag{2.1-10}$$

If the source is directional and we define a directivity function

$$D(\theta) = \frac{I(\theta)}{I_0} \ , \tag{2.1-11}$$

59
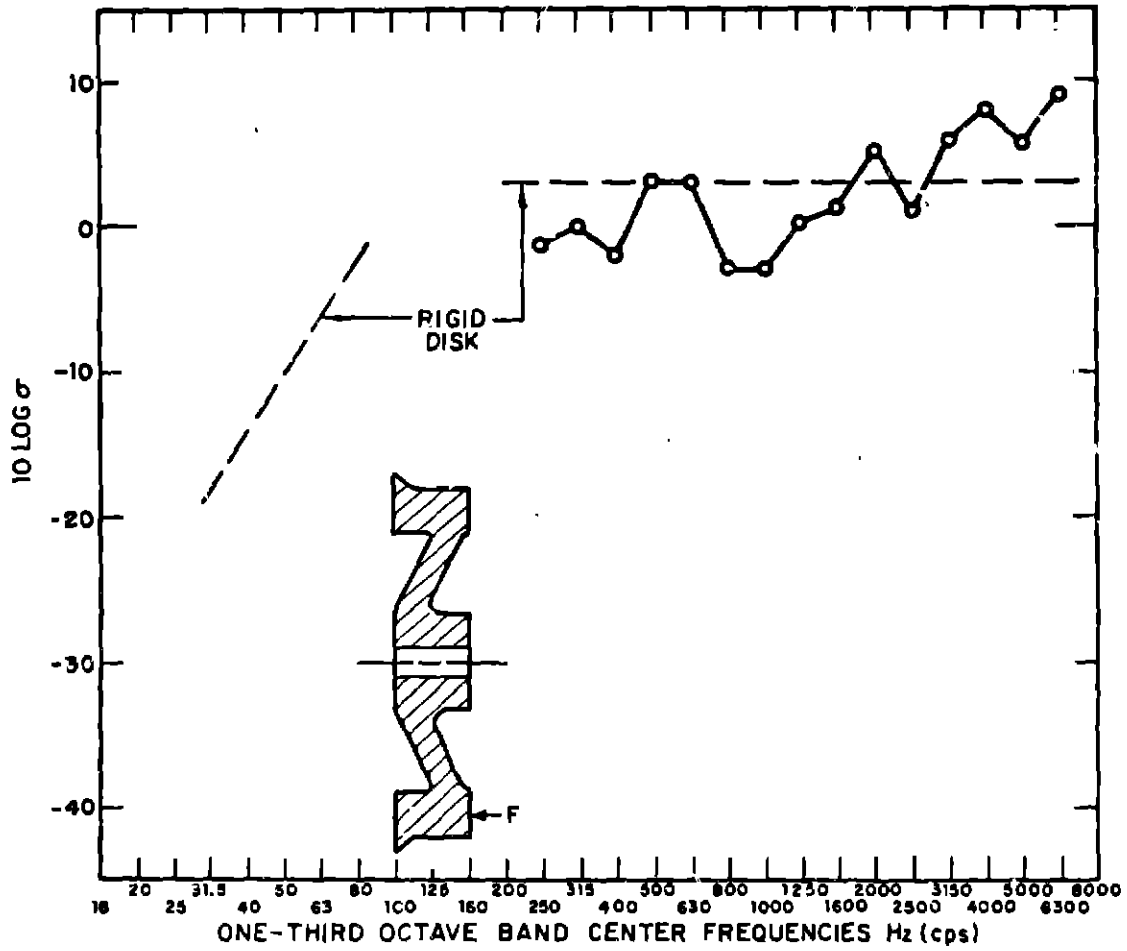
FIG. 2.1-22.   WHEEL RADIATION EFFICIENCY FOR AXIAL FORCING.

where $I(\theta)$ is the intensity in direction θ* and I_0 is a reference intensity equal to $W/2\pi R^2$, then the mean square pressure in direction θ becomes

$$\langle p^2(\theta) \rangle = \frac{\rho_0 W}{2\pi R^2} D(\theta) .$$ (2.1-12)

Railroad Wheels

We performed a number of measurements of wheel directivity at the Pullman Standard test track in Hammond, Indiana, in the center of the test track, a large, flat, open area with no reflecting surfaces within several hundred feet of the test area. A wheel set with 30 in. (0.76 m) diameter wheels was raised off the ground and supported at the axle on rubber pads on two steel horses. The only way we could obtain sufficient signal level (to overcome the background) was to strike the wheel with a hammer and simultaneously measure the resulting SPL by recording the output of two B&K 4133 1/2-in. (1.25 cm) microphones on a Kudelski Nagra IV stereo tape recorder. One microphone was placed at a reference point on the axis of the wheel 10 ft (3.1 m) from the face and the other microphone at various positions 10 ft (3.1 m) from the face in a horizontal plane at the height of the wheel axle above the ground at varying angles from the wheel axis. We reduced the resulting data by finding those 1/3-octave bands (using a General Radio 1564a Sound and Vibration Analyzer) in which the greatest response was measured and then using a sound level meter that holds peaks (General Radio 1566a) to ascertain the peak SPL in those

---

*In general the directivity will require two angles in spherical coordinates to define it. We restrict ourselves here to one for simplicity of notation.

1/3-octave bands at the reference point and at a simultaneously recorded point at a given angle from the wheel axis. Comparison of the two levels yields a measure of directivity. In performing the measurements, we struck the wheel three times on the face of the tread in the radial direction at the top of the wheel and three times on the flange at the top of the wheel in the axial direction. By taking the difference between the level measured at six angular positions (every 15°) around the wheel and the level at the reference point and plotting this difference relative to the average of this difference for all six angles, one can generate the directivity function of Eq. 2.1-11. The results are plotted in Figs. 2.1-23 and 2.1-24. These figures show effectively the difference between the measured level and what one would obtain if the wheel were an omnidirectional source radiating equally in all directions. These data show that within ±5 dB the wheel does radiate equally in all directions.

These results are not consistent with data obtained by Ungar *et al* (1970) who measured the directivity of sound radiated from a wheel screeching in a retarder in the vertical plane perpendicular to the rail. The level in 1/3-octave bands at 20° from the wheel axis was 15 dB below the level measured on the axis in the 1 kHz to 3 kHz range. One would expect results like Ungar's for radiation from a rigid unbaffled disk (Morse and Ingard, 1968, Chap. 7.4), but the railroad wheel is a far more complicated structure than a disk. In fact, the tread of the wheel has a total surface area nearly 3/4 of the area of the circle formed by the tread of the wheel (i.e., the web area). Since the vibration levels on the tread are comparable to those on the web, the power radiated by the tread should be on the order of that radiated from the web. This of course
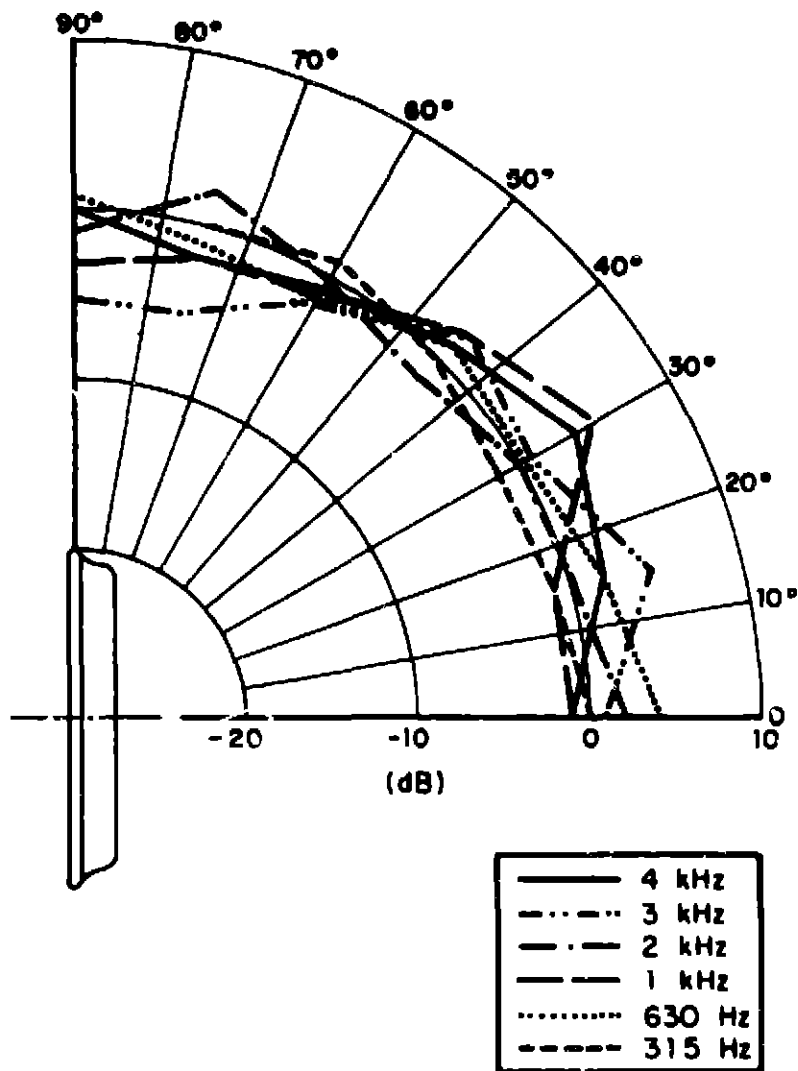
FIG. 2.1-23   ONE-THIRD OCTAVE BAND WHEEL DIRECTIVITY UNDER
               AXIAL FORCING

63
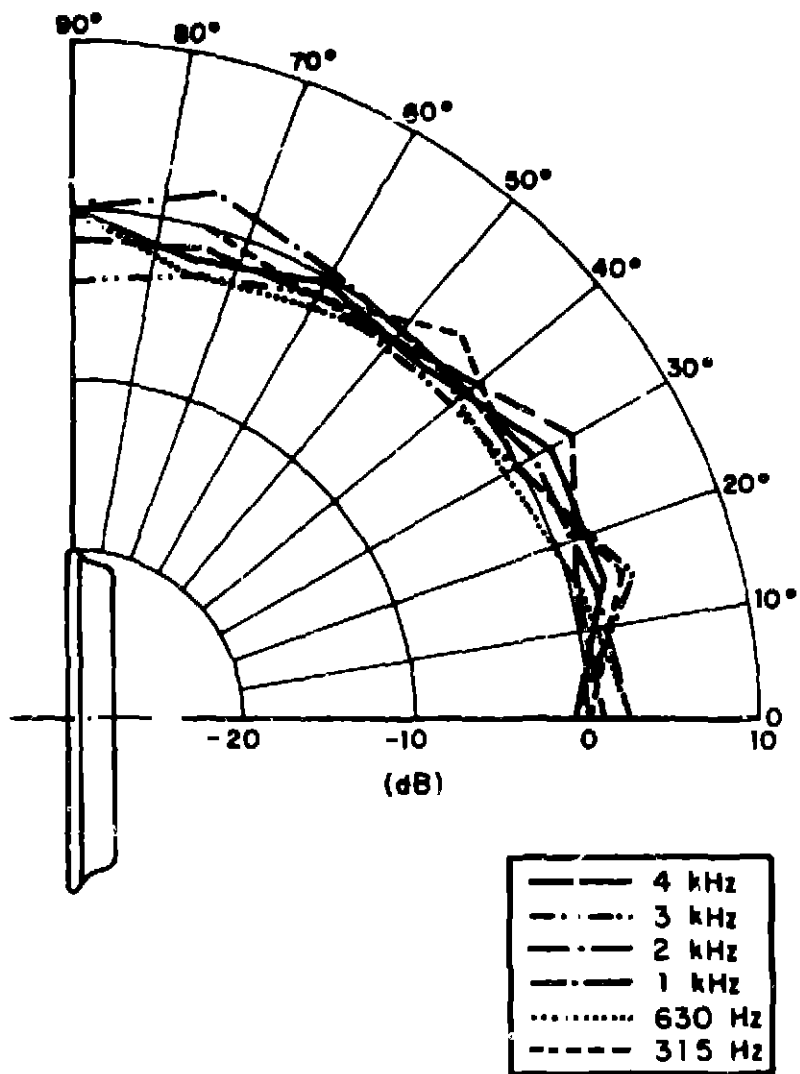
FIG. 2.1-24 ONE-THIRD OCTAVE BAND WHEEL DIRECTIVITY UNDER RADIAL
FORCING

64

assumes that the radiation efficiencies of the two surfaces are
comparable, which is reasonable since the wave speeds in the
wheel are generally well above coincidence. One would expect
the web to radiate primarily in the axial direction and the
tread to radiate primarily in the plane of the wheel. Such
radiation implies a relatively uniform directivity pattern with
the levels in the plane of the wheel being on the order of 2 dB
lower than levels on the axis. The measurements of Figs. 2.1-23
and 2.1-24 generally support the model. The discrepancy between
these results and Ungar's may be due to a number of causes. For
example, Ungar measured the directivity of essentially pure-tone
wheel response, which is more susceptible to multipath inter-
ference. Also, the geometry was certainly quite different. The
measurements here were from a wheel suspended above the ground.
Ungar's measurements were of a wheel on a rail in a retarder
with the rest of the car structure present.

The results in Figs. 2.1-23 and 2.1-24 show how much one
would underpredict the SPL at a given angle assuming the direc-
tivity to be uniform; from these results it is apparent that
treating the wheel as having uniform directivity will provide
adequate prediction of the SPL radiated by the wheel, especially
in the axial direction.

Railroad Rails

For most applications a railroad wheel can be thought of
as a point source for which the simple model of Eq. 2.1-11
applies. A railroad rail, however, can be considered anything
from a point to a line source, depending upon how uniform the
radiated acoustic power is along the length of the rail. If
the rail is modeled as a line of incoherent sources and if the
radiated power per unit length is $W(x)$ and x is the distance

65

along the rail, then the sound pressure level at a perpendicular distance R from the rail can be written

$$<p^2(\phi)> \; = \; \frac{\rho c}{\pi} \int_0^\infty \left[\frac{W(x)dx}{R^2+x^2} \right] D(\phi) \; ,$$

where ϕ is the angle between a line perpendicular to the rail and the ground plane and $D(\phi)$ the directivity. If we assume that the rail acts like a line of monopoles, then the above equation becomes

$$<p^2(\phi)> \; = \; \sigma_R(r_H + r_F) \left[\frac{(\rho c)^2}{\pi} \int_0^\infty \frac{v^2(x)dx}{R^2+x^2} \right] D(\phi) \; ,$$

where σ_R is given by Eq. 2.1-7 and $v(x)$ is the velocity on the rail as a function of position. From the data in Sec. 2.1.2, it is apparent that the rail vibration can be modeled as decaying like $e^{-\eta x}$. Substituting $<v_R>^2 \, e^{-\eta x}$ for $<v^2(x)>$ in the above equations yields

$$<p^2(\phi)> \; = \; \sigma_R(r_H + r_F) \; \frac{(\rho c)^2}{\pi} \; \frac{1}{R} \; f(\eta R)D(\phi)v_R^2 \; , \quad (2.1-13)$$

where $<v_R^2>$ is the time-averaged rail velocity at the excitation point and

$$f(\eta R) \; = \; \sin\eta R \; Ci(\eta R) \; - \; \cos\eta R \left[Si(\eta R) \; - \; \frac{\pi}{2} \right] \; ,$$

where $Ci(\;)$ and $Si(\;)$ are the cosine and sine integrals respectively. The function $f(\eta R)$ is shown in Fig. 2.1-25. It is apparent that for ηR small, $f(\eta R) \sim 1$ and the rail is a line source. For ηR large, $f(\eta R) \sim 1/\eta R$ and the rail is a point source radiating from a length of $1/\eta$. We approximate this

66

dependence by the dotted curve in Fig. 2.1-25 which is

$$f(\eta R) = 1 \quad , \qquad \eta R < 1$$

$$f(\eta R) = \frac{1}{\eta R} \, , \qquad \eta R > 1 \ .$$

Typical values of η for the attenuation measured at the Pullman Standard test track and values of R for $\eta R = 1$ are shown in Table 2.4.

TABLE 2.4.   RAIL ATTENUATION VALUES BASED ON
PULLMAN STANDARD TEST TRACK DATA.

Frequency	η	R For Which $\eta R = 1$
250 Hz	$0.23 \ ft^{-1}$ $(0.073 \ m^{-1})$	4 ft (1.2 m)
500 Hz	$0.23 \ ft^{-1}$ $(0.073 \ m^{-1})$	4 ft (1.2 m)
1000 Hz	$0.12 \ ft^{-1}$ $(0.037 \ m^{-1})$	8 ft (2.4 m)
2000 Hz	very small	--
4000 Hz	very small	--

The directivity of the rail in the plane parallel to its length can be inferred from the above information and will be dealt with in Sec. 2.4 in terms of a source being located not opposite the receiver but at some distance down the track. However, information is still required for the directivity of the rail in the plane *perpendicular* to its length.   We took
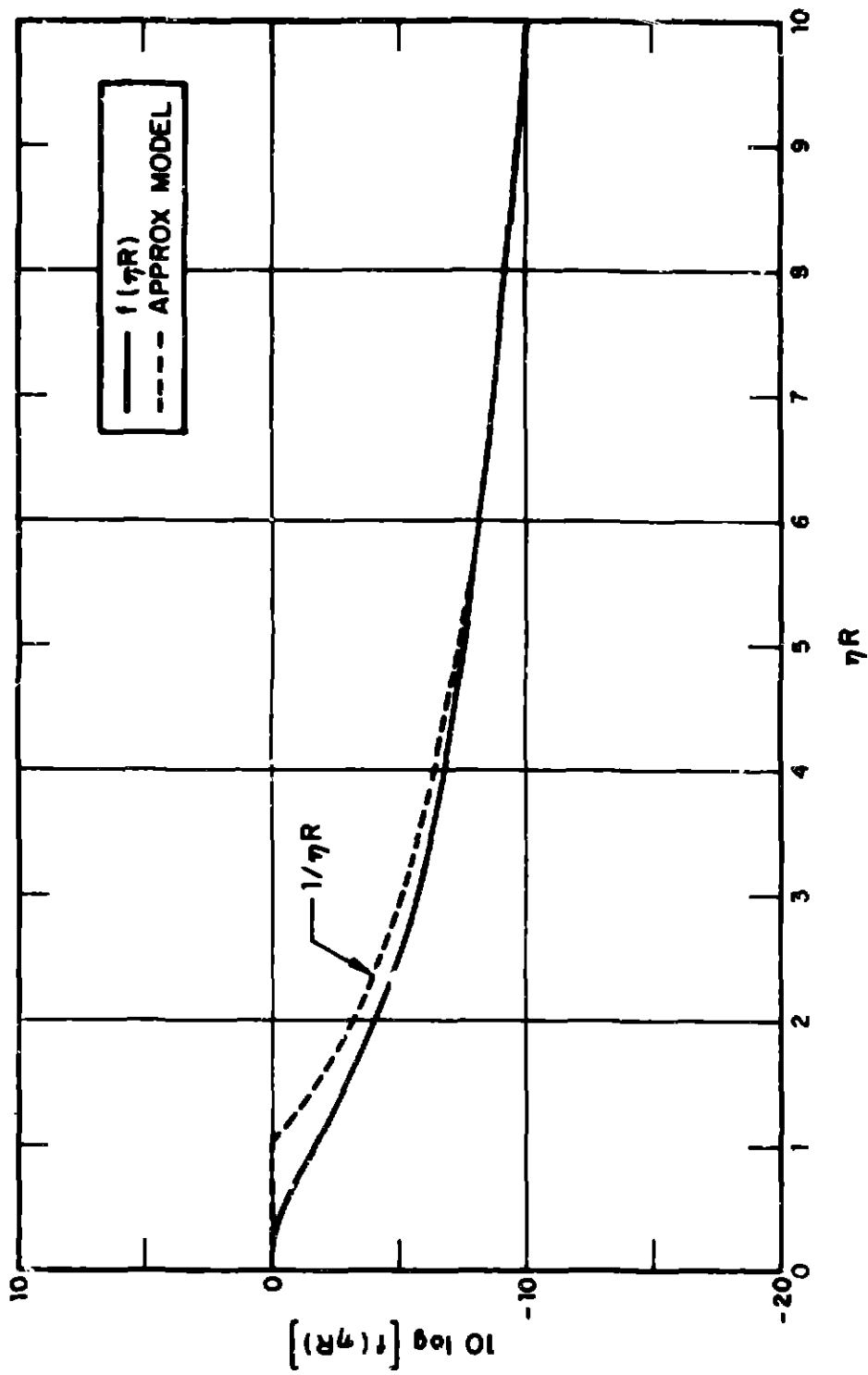
FIG. 2.1-25 DEPENDENCE OF THE MEAN SQUARE RADIATED PRESSURE ON THE DISTANCE FROM THE RAIL

68

measurements of this directivity on a 20 ft (6.1 m) section of
AREA 100 lb/yd (49 kg/m) rail. The rail was set on rubber pads
that were laid every 2 ft (0.61 m) on the ground in a dirt
parking lot. There were no reflective surfaces within 50 ft
(15.3 m) in the direction of the rail axis or within 100 ft
(30.5 m) in the direction perpendicular to the axis.
Measurements showed a 1/R dependence of the 1/3-octave band
SPL out to 8 ft (2.4 m) from the rail and a $1/R^2$ dependence of
the SPL from 8 ft (2.4 m) to 32 ft (9.8 m) from the rail. The
rail was excited at the head both vertically and horizontally
with a Goodman V-50 electromagnetic shaker enclosed in a 3/4 in.
(1.9 cm) thick plywood box lined with 2 in. (5 cm) of fiber-
glass* and driven with white noise filtered in 1/3-octave bands.
Constant excitation in a given 1/3-octave band was maintained
by monitoring the current into the shaker. Measurements of the
SPL using a B&K 1/2 in. (1.25 cm) microphone were made at 6 ft
(1.8 m) from the rail at various angles in the plane perpendic-
ular to the rail. The measured SPL at a given angle minus the
average SPL for all angles, i.e., $D(\phi)$ in Eq. 2.1-13, is plotted
in Figs. 2.1-26 and 2.1-27.

On a theoretical basis, by treating the rail as a uniformly
vibrating rigid cylinder, one would expect the directivity for
horizontal excitation to be of the form $2 \cos^2\phi$, where ϕ is the
angle from the ground plane (see Bailey and Fahy, 1972). As
seen in Fig. 2.1-26, this theoretical curve agrees quite well
with the data in the 500-Hz band. At high frequencies the rail
ceases to move like a single beam (the head, web, and foot be-
gin to vibrate independently of one another) and this simple
model no longer applies.

---

*Previous measurements taken in a reverberant room confirmed
the effectiveness of the box in suppressing noise from the
shaker.
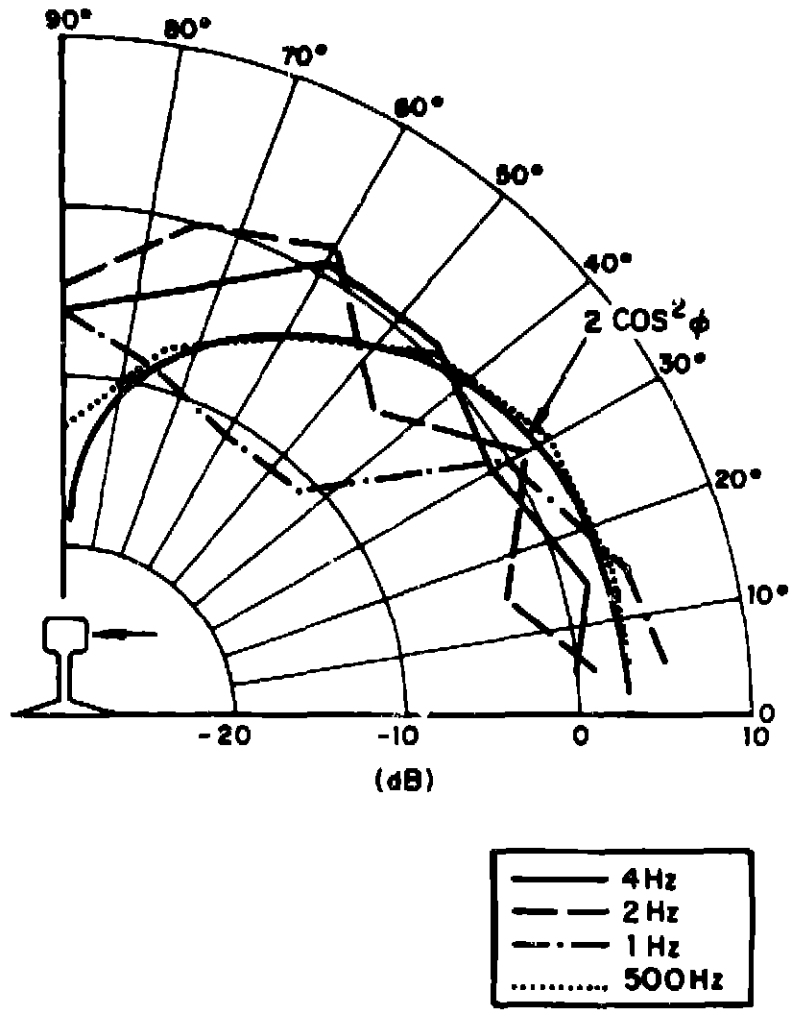
FIG. 2.1-26   ONE-THIRD OCTAVE BAND RAIL DIRECTIVITY FOR
HORIZONTAL EXCITATION
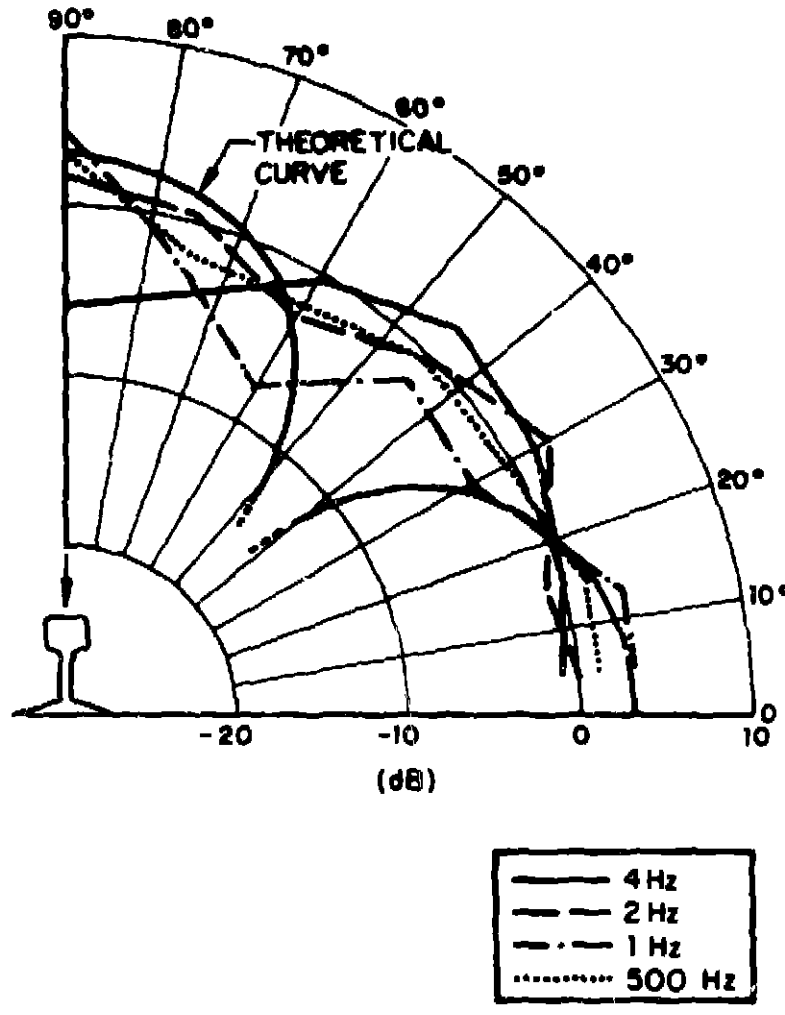
FIG. 2.1-27 ONE-THIRD OCTAVE BAND RAIL DIRECTIVITY FOR
VERTICAL EXCITATION

71

If there were no reflecting surface beneath the vertically excited rail, the rail would have a theoretical directivity pattern (based on modeling the rail as a uniformly vibrating rigid cylinder) of the form $2\sin^2\phi$. The presence of a perfect reflecting plane beneath the idealized rail would change this directivity pattern to $2\cos^2 2\phi$. This latter pattern is plotted in Fig. 2.1-27. As can be clearly seen, it predicts equivalent levels above the rail and to the side which fit the general trend of the data. Of course, the shape of the pattern is strongly influenced by the reflectivity of the plane under the rail; e.g., the strong null at 45° requires that the plane be perfectly reflecting.

Because we are uncertain both of the reflectivity of the surface on which the rail may be mounted and of the complexity of the rail vibration at high frequencies, we make the approximation in the work to follow that the rail directivity is uniform [i.e., $D(\phi) = 1$] for both vertical and horizontal excitation. Figures 2.1-26 and 2.1-27 show that this approximation will lead to only slight underestimation of the SPL from the rail at low angles.

2.2 Wheel Squeal Predictive Formulas

It is generally accepted that a "stick-slip mechanism," is responsible for squeal, i.e., as a force on the wheel tends to make it slide, static friction tends to make the wheel stick on the rail. As the sliding force increases, it eventually exceeds the static friction force and the wheel starts to slide. Since static friction is generally greater than sliding friction, the wheel will continue to slide until the force which causes the sliding drops to the sliding friction value.

72

Static friction will then build until the wheel sticks again. This sticking and sliding occurs in very rapid succession.

Three different ways have been identified in which the wheel can slide resulting in three models for the mechanism of wheel squeal: differential slip between inner and outer wheels on a solid axle; rubbing of the wheel flanges against the rail; and crabbing of the wheel across the top of the rail. When two wheels on the same axle go round a curve and the inner wheel has to travel less distance and hence rotate slower than the outer wheel *differential slip* can occur. The resulting torque on the wheel tends to make it slip on the rail. *Flange rubbing* occurs when the wheel flange rubs against the outside rail. The sliding of the flange against the rail provides an opportunity for sticking and slipping to occur. *Wheel crabbing* occurs on transit cars having trucks, with two parallel axles. When the truck enters a curve, the parallel axles cannot both lie upon the radius of the curve. As a result, the wheel must not only roll around the curve, they must also slide across the rail, again with the possibility of inducing squeal. This crabbing motion is solely a consequence of the finite wheel base length of the truck, and a truck with a single axle would not crab.

Remington *et al* (1974) considered these three mechanisms. The fact that lubrication of the outer rail alone does not always eliminate squeal tended to rule out the first two mechanisms. In addition, the fact that a differential axle does not prevent squeal also tends to rule out the first mechanism. Further, it was shown that the elastic deformation of the wheel tread was sufficient to compensate for the different distances that the inner and outer wheels have to travel.

73

It will be shown that the stick-slip mechanism can be
described as a negative damping. If this negative damping ex-
ceeds the natural positive damping in the wheel, then any small
vibration, once initiated, will grow and produce the intense
squeal that is heard. The phenomenon is one of instability of
the wheel vibration rather than of resonant amplification:
there is only a limited range of conditions under which the
vibration is unstable and, hence, under which squeal can occur.
Our intent is to develop a model to identify these conditions,
to predict the sound pressure levels to be expected for squeal,
and to predict the changes in parameters (such as the amount of
damping required) to avoid squeal.

2.2.1 Detailed wheel squeal model

Stability Criterion

Let us define the modal mass of the wheel m by

$$m = \frac{\text{mean kinetic energy of vibration}}{\text{the mean square velocity of vibration at the rail}} .$$

For a simple spatially sinusoidal motion, m would be half the
mass of the wheel. In reality some parts of the wheel (web) do
not move as much as others (tread) and, hence, the modal mass
is nearer a third the mass of the wheel. The modal mass will
tend to vary slightly with the mode and, hence, with the fre-
quency of the vibration. Let us define also a modal stiffness
K by

$$K = \frac{\text{mean bending energy of vibration}}{\text{the mean square displacement of vibration at the rail}} .$$

74

Let us also define a damping constant for the wheel, C, and the negative damping due to stick-slip, $-\ell$. Then we can write down a generalized relation between the force F applied to the wheel and its velocity v of vibration at a frequency ω.

$$F = (imw + C + \frac{K}{i\omega} - \ell)v \ .$$

For a self-sustained oscillation $F = 0$. Hence $v = 0$ or

$$im\omega + C + \frac{K}{i\omega} - \ell = 0$$

$$m\omega^2 + i(C-\ell)\omega - K = 0$$

$$\omega = \frac{1}{2m} [i(C-\ell) \pm \sqrt{4mK - (C-\ell)^2}]$$

or if damping is small, i.e., $(C-\ell)^2 \ll 4mK$,

$$\omega \approx \pm \sqrt{\frac{K}{m}} + \frac{i(C-\ell)}{2m} \ .$$

The solution for the motion of the wheel with an initial velocity v_0 is

$$v = v_0 \exp\left(\pm i \sqrt{\frac{K}{m}} t\right) \exp\left(- \frac{C-\ell}{2m} t\right) .$$

If $C > \ell$ then the motion is a decaying sinusoid, but if $C < \ell$ then the motion grows exponentially. Thus, a sufficient condition for the vibration of the wheel to go unstable is that $C < \ell$ and the frequency of the instability is the natural resonance frequency of the wheel.

Magnitude of Negative Damping

By definition $\ell = - \Delta F/\Delta V$, where ΔF is change in frictional force and ΔV is change in wheel sliding velocity. Now $\Delta F = P\Delta\mu$, where P is wheel loading and $\Delta\mu$ is change in friction coefficient. Furthermore, we shall call $\Delta V/V = \Delta\xi$ the creep, where V is the rolling velocity of the wheel. This formulation assumes that the friction is a function only of the creep rather than of the absolute sliding velocity. This assumption is known to be true for elastic deformations, but it is not clear if it applies to gross sliding. Hence,

$$\ell = - \frac{P}{V} \frac{\Delta\mu}{\Delta\xi} .$$

Let us now call $\Delta\mu/\Delta\xi = \nu$, the slope of the friction vs creep curve. ν is typically of order of magnitude -10 or less. Thus

$$\ell = - \frac{P\nu}{V} .$$

The loss factor for stick-slip η_{ss} is given by

$$\eta_{ss} = \frac{\ell}{m\omega} = - \frac{P\nu}{m\omega V} .$$

Radiated Sound Power

The sound power radiated from the wheel is given by

$$W_{sound} = \sigma\rho c \frac{A v^2}{2} ,$$

where σ is radiation efficiency (≈ 1 at frequencies of interest), ρc is the characteristic impedance of air A is the area of the wheel, and v is the velocity amplitude of the vibrations.

The power dissipated in a dashpot is

$$W = (1/2)Cv^2 .$$

Hence, the equivalent damping constant of the acoustic radiation is

$$C_{rad} = \sigma\rho cA$$

and the equivalent loss factor is

$$\eta_{rad} = \frac{\sigma\rho cA}{m\omega} .$$

Loss Factor Due to Internal Damping

The material from which the wheel is made has its own damping that is characteristic of the material. For steel the internal loss factor $\eta_{int} \simeq 3 \times 10^{-4}$.

This loss factor can clearly be increased by applying damping treatment to the wheel.

Stable Amplitude

Once the wheel vibrations have become unstable, their amplitude will grow until nonlinearities in the system limit them. These nonlinearities occur in the stick-slip mechanism. The slope of the friction vs creep curve changes for finite amplitude vibrations and reduces the effective magnitude of the negative damping. For a stable amplitude of vibration,

$$\eta = -\ell = \frac{P\bar{v}}{V} ,$$

where $\bar{v}$ is some average value of v taken over a whole cycle.

77

$\overline{\nu}$ is dependent upon the amplitude of the vibration. Now C is given by the sum of the acoustic and the internal damping:

$$C = n_{int}m\omega + \sigma\rho cA \quad .$$

Hence, for the stable squeal amplitude

$$n_{int}m\omega + \sigma\rho cA = \frac{P\,\overline{\nu}}{V} \quad .$$

Calculation of $\overline{\nu}$

$\overline{\nu}$ is related to the work put into the wheel during one cycle. Hence, we can define it as

$$\overline{\nu} = \frac{\oint \nu v^2 dt}{\oint v^2 dt} \quad ,$$

where $\oint$ indicates the integration over one cycle, and where v is the vibration velocity, since $\nu V/V$ is equal to the driving force and $\nu v^2/V$ is the rate at which work is done. For a sinusoidal oscillation $v = v_0 \sin\omega t$

$$\overline{\nu} = 1/2 \oint \nu\left(\frac{V}{2}\right) \sin^2\omega t \; dt \quad .$$

We cannot proceed any further without some information about the variation of ν with the slip velocity. The form of the variation of the coefficient of friction μ with the creep ξ is that for small ξ, μ is proportional to ξ; μ then reaches a maximum μ_0, after which it decreases.
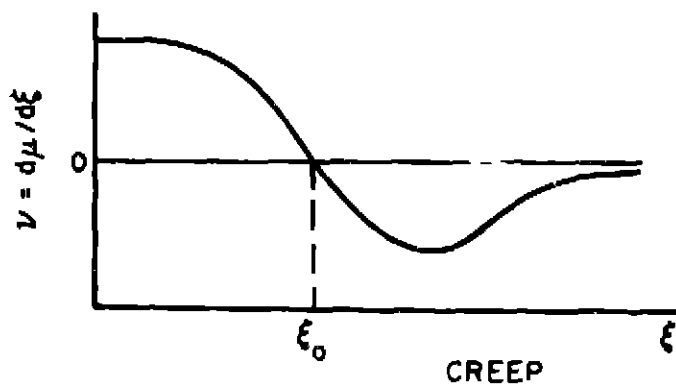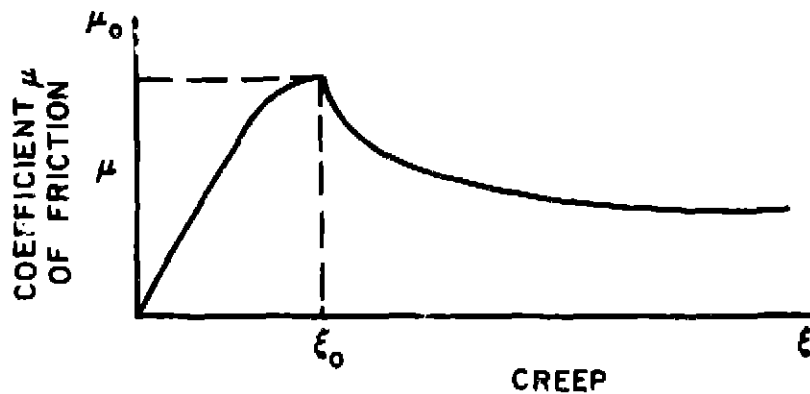
We shall now try and get a feel for $\bar{\nu}$ by taking the simplest analytical expression which has this form. Hence, let us assume

$$\mu = \mu_0 \; \frac{\xi}{\xi_0} \; \exp \left(1 - \frac{\xi}{\xi_0} \right).$$

This expression is probably very different from a real stick-slip curve (for example, $\mu \rightarrow 0$ as $\xi \rightarrow \infty$), but it possesses all the essential features and can be used as an example. Let us

call $\xi/\xi_0 = \theta$, where ξ_0 is the creep for the maximum friction μ_0. Then

$$\mu = \mu_0 \, \theta \, \exp(1 - \theta)$$

and

$$\nu = \frac{d\mu}{d\xi} = \frac{\mu_0}{\xi_0} (1 - \theta) \exp(1 - \theta) \ .$$

Now let

$$\theta = \bar{\theta} + \theta' \sin\omega t \ ,$$

where $\bar{\theta}$ is mean creep$/\xi_0$, θ' is $v/V\xi_0$, and v is the velocity amplitude. Hence,

$$\bar{\nu} = \frac{\mu_0}{\pi\xi_0} \oint [(1-\bar{\theta}-\theta') \sin\omega t] \exp[(1-\bar{\theta}-\theta') \sin\omega t] \sin^{-2}\omega t \, dt \ .$$

Now we can expand the exponential as a series in $\sin\omega t$ and integrate the terms separately. Odd powers of $\sin\omega t$ go to zero, giving

$$\bar{\nu} = \frac{\mu_0}{\xi_0} e^{1-\bar{\theta}} \left[(1-\bar{\theta}) + \frac{3}{8} (3-\bar{\theta})\theta'^2 + \frac{5}{192} (5-\bar{\theta})\theta'^4 \cdots \right]$$

$$= \frac{\mu_0}{\xi_0} \exp(1-\bar{\xi}/\xi_0) \left[(\xi_0-\bar{\xi}) + \frac{3}{8} (3\xi_0-\bar{\xi}) \frac{\xi'^2}{\xi_0^2} \right.$$

$$\left. + \frac{5}{192} (5\xi_0-\bar{\xi}) \frac{\xi'^4}{\xi_0^4} \cdots \right] \ .$$

Let us now consider three ranges of $\bar{\xi}$ = V sliding/V wheel.

1. $\bar{\xi} < \xi_0$. $\bar{v}$ is always positive; hence, the system has no negative damping and squeal cannot occur.

2. $3\xi_0 > \bar{\xi} > \xi_0$. $\bar{v}$ is negative for small amplitudes of vibration (ξ') but decreases in magnitude as the amplitude increases. Thus, the amplitude of squeal stabilizes at some finite amplitude.

$$3\xi_0 > \bar{\xi} > \xi_0$$
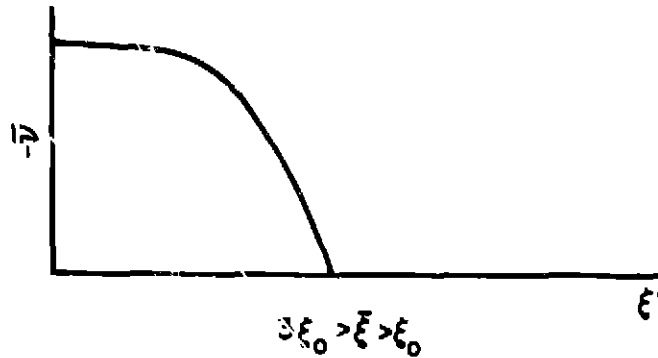
3. $\bar{\xi} > 3\xi_0$. $\bar{v}$ initially goes more negative as the amplitude increases, but at larger amplitudes decreases in magnitude again. This means that if the amount of negative damping needed for squeal is in the dotted region of the figure below, then the vibrations would be stable for small amplitudes, but unstable only for some finite amplitude. This means that the wheel might need a finite sized "kick" to start squeal but would then maintain itself.

81

$$\bar{\xi} > 3\xi_0$$
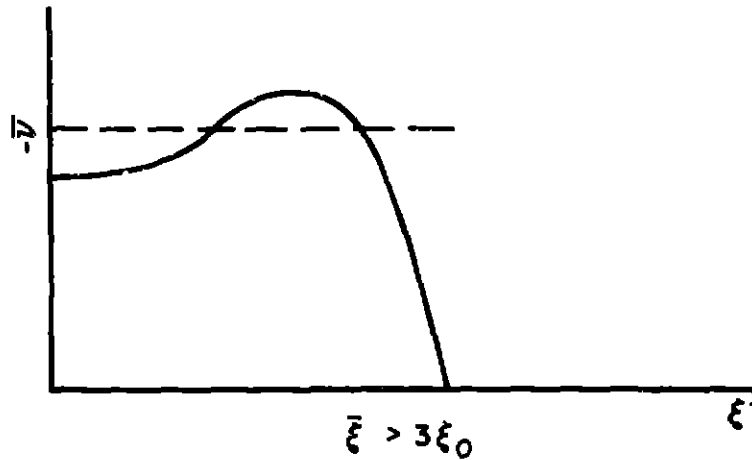
Calculation of Stable Amplitude

We repeat the expression for negative damping due to stick-slip for a stable amplitude of vibration:

$$\eta_{int} m\omega + \sigma\rho cA = \frac{P\,\bar{\nu}}{V} .$$

Applying the expression for $\bar{\nu}$ from above gives

$$\eta_{int} m\omega + \sigma\rho cA = \frac{P}{V}\ \frac{\mu_0}{\xi_0^2}\ \exp(1-\bar{\xi}/\xi_0)\ \left[(\xi_0-\bar{\xi}) + \frac{3}{8}\,(3\xi_0-\bar{\xi})\,\frac{\xi'^2}{\xi_0^2}\right.$$

$$\left. + \frac{5}{192}\,(5\xi_0-\bar{\xi})\,\frac{\xi'^4}{\xi_0^4}\right] .$$

If $\xi' < 2\xi_0$, we can neglect the last term. Then

$$\frac{3}{8}\,(3\xi_0-\bar{\xi})\,\frac{\xi'^2}{\xi_0^2} = \frac{V\xi_0^2}{Wg\mu_0}\ \exp\!\left(\frac{\bar{\xi}-\xi_0}{\xi_0}\right)\,(\eta_{int} m\omega + \sigma\rho cA)\ + (\bar{\xi}-\xi_0) .$$

For small damping we can neglect the first term on the right-hand side and

$$\xi' = \xi_0 \left[\left(\frac{8}{3}\right) \frac{\overline{\xi}-\xi_0}{3\xi_0-\overline{\xi}} \right]^{\frac{1}{2}}$$

$$\approx 1.15 \, (\overline{\xi}-\xi_0)^{\frac{1}{2}} \qquad \text{for} \qquad \overline{\xi}/\xi_0 - 1 << 1 \ .$$

Thus, for small squeal amplitudes, the velocity of the squeal vibration is just a little larger than the square root of the amount by which the mean creep exceeds the creep for maximum friction.

Order of Magnitude of Quantities of Interest

Maximum coefficient of friction (μ_0):	from 0.15 to 0.6; typical value is 0.3.
Creep for maximum friction (ξ_0):	0.5% for 4-ton (3630 kg) wheel loading to 1% for 20-ton (18,200 kg) wheel loading; typical value is 0.7%.
Creep on rounding curve $(\overline{\xi})$:	≈ 0.7 L/R where L is length of truck and R is radius of curve.
For squeal to occur:	0.7 L/R > .7%, R < 100L $\approx$ 700 ft (214 m).
Typical velocity amplitude of squeal:	$1.15 \left\| \left(\frac{.7L}{R} - \frac{.7}{100}\right) V \right\|^{\frac{1}{2}}$
	where V is speed of train.

Sound Pressure Level of Squeal

From the previous equation for radiated sound power, the sound pressure level of squeal from a single wheel at 50 ft (15.2 m) is given by

83

$$L_p = 10 \log \sigma\rho c A v^2 + 88 \text{ dB re } 0.0002 \text{ } \mu\text{bar}$$

$$= 10 \log \sigma A v^2 + 114 \text{ dB re } 0.0002 \text{ } \mu\text{bar} .$$

Setting $v = \xi' V$

$$L_p = 10 \log (\sigma A) V \left(\frac{L}{R} - \frac{1}{100} \right) + 113 \text{ dB} .$$

Typical values are

$$\sigma A \simeq 0.5 \text{ m}^2$$

$$V \simeq 15 \text{ mph } (24 \text{ km/h})$$

$$L \simeq 7 \text{ ft } (2.13 \text{ m})$$

$$R \simeq 300 \text{ ft } (91.5 \text{ m}) .$$

Substituting these values into the above expression for SPL gives

$$\text{SPL} = 95 \text{ dB re } 0.0002 \text{ } \mu\text{bar at } 50 \text{ ft } (15.2 \text{ m}) .$$

2.2.2 Magnitude of damping required to eliminate squeal

For the relatively large amounts of damping needed to eliminate squeal, we can neglect the damping due to acoustic radiation. Then, the loss factor needed to avoid squeal is

$$\eta_{int} > \frac{P v_{max}}{m \omega_{min} V} .$$

Let us take typical values of P = 10,000 lb (44,500 N), m = 200 lb (91 kg), ω_{min} = 3,000 rad/sec, and V = $\sqrt{aR}$, where a = lateral acceleration of car (about 3% of g) and R = radius of

curve. Then

$$n_{int} > \frac{\nu_{max}}{2\sqrt{R}} \cdot$$

ν_{max} will vary with the amount of transverse creep on the curve
and will typically be a maximum when macroscopic slipping just
starts. Then ν is typically about 30 and R is about 700 ft
(214 m) in which case

$$n_{int} = 0.6 \cdot$$

In this case the damping ratio relative to critical damping is
30%. If we have a damping ratio of 30%, squeal will not occur
on any curves. However, for a curve radius of 200 ft (61 m) with
a considerable amount of slippage, the value of ν is greatly re-
duced to about 2 or so, and a value of damping that is 3% of
the critical damping will eliminate squeal.

In summary, damping equal to 3% of critical damping may
eliminate squeal on tight curves, but *more* damping will be
needed on *larger* curves, up to the maximum radius at which
squeal can occur.

2.2.3 Conditions under which squeal can occur

It was shown above that for squeal to occur

$$n_{int}m\omega + \sigma\rho cA < \frac{P\nu(\xi)}{V} ,$$

where the creep ξ is approximately given by 0.7 L/R, L is the
length of the truck, and R is the radius of curve. If we take
a given curve, the amount of creep is approximately defined

and then the occurrence of squeal is a function of the wheel
loading P, the velocity of the car V, and the frequency ω.
The frequency ω can take on only certain well-defined values
corresponding to the resonant modes of the wheel. For each
mode there is then a minimum value of the ratio P/V which will
produce squeal. Thus, there is a *minimum* wheel loading for a
particular velocity or a *maximum* velocity for a particular
wheel loading which will produce squeal. These relations are
shown in the sketch below.
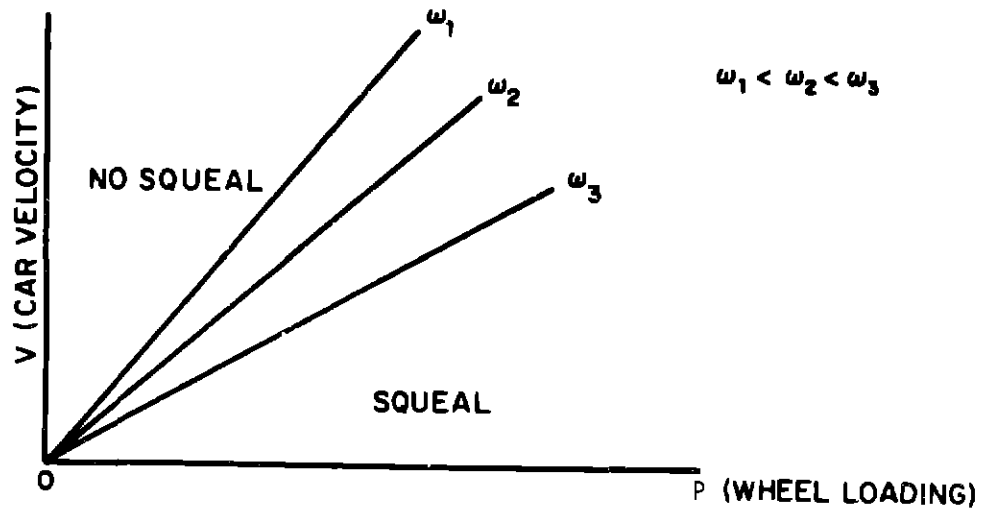
Squeal Occurrence Diagram for Given Curve Radius
(Squeal occurs to the right of the lines drawn above)

If we keep the wheel loading constant and vary the curve
radius and speed, then the squeal occurrence diagram looks like
the one below.
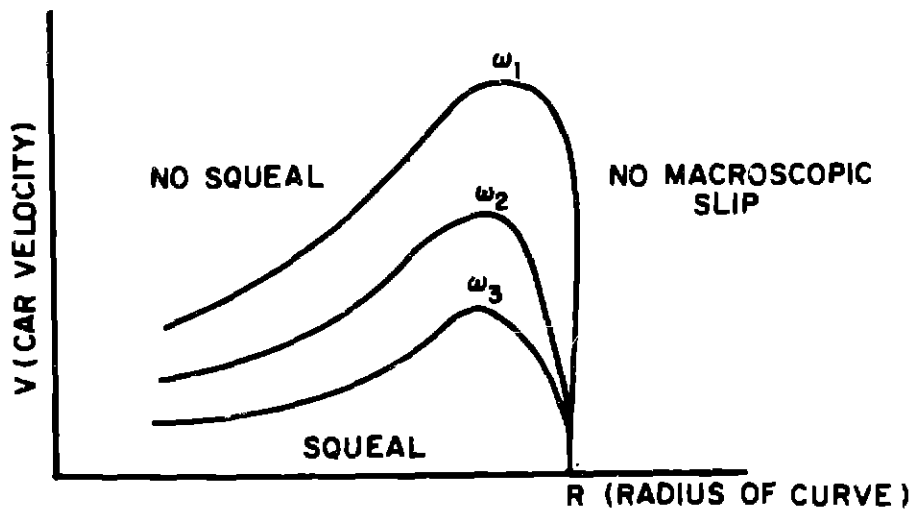
Squeal Occurrence Diagram for Constant Wheel Loading
(Squeal occurs below the lines drawn above)

For an undamped wheel, the theoretical values of the maximum velocities for squeal tend to be so high that they give unacceptably high lateral accelerations on passengers. Hence, these maximum velocities are not observed in practice, and squeal occurs over the whole range of velocities employed.

Sometimes a minimum velocity for squeal can be found. This situation generally occurs when a car is close to the squeal boundary. Increasing the speed will increase the wheel loading on the outer wheels, by weight transfer, and at the same time reduce the creep, and hence increase v as a result of centrifugal forces. These combined effects can cause a car to cross the squeal occurrence boundary from the no squeal to the squeal region.

2.2.4 Predictions of squeal levels

Figures 2.2-1 and 2.2-2 show the predicted intensities of squeal as a function of curve radius. The first figure predicts the levels of squeal for different lateral accelerations in the curve and a 7 ft (2.13 m) wheelbase truck. It will be noted that there is not a very large difference in levels for the two speeds. The second figure predicts the levels of squeal for different truck wheelbases. The shorter trucks do not squeal as loudly or on as large a radius curve as do the longer trucks.

2.2.5 Information on the friction-creep curve

The ability of this model to predict the occurrence of wheel squeal depends upon a detailed knowledge of the friction-creep curve. Very little experimental information is currently available on this phenomenon. All the information for this report comes from just two references [Barwell and Woolacott (1963) and Friedrich (1970)], and one of these references considers longitudinal creep rather than the transverse creep we are concerned with. There has been much work conducted on transverse creep without macroscopic slip but practically none on transverse creep with some slip. A thorough, careful experimental study needs to be conducted into the exact variation of friction with creep, as slipping starts. The effects of humidity, surface roughness, and lubrication need to be found.

Many of the predictions of wheel squeal, such as the maximum radius for squeal, are based upon a value of 0.7% for the "break" point at which macroscopic sliding starts. There is very little experimental evidence to support this value and accurate predictions of the levels of squeal as well as the likelihood of its occurrence require that this evidence be obtained.
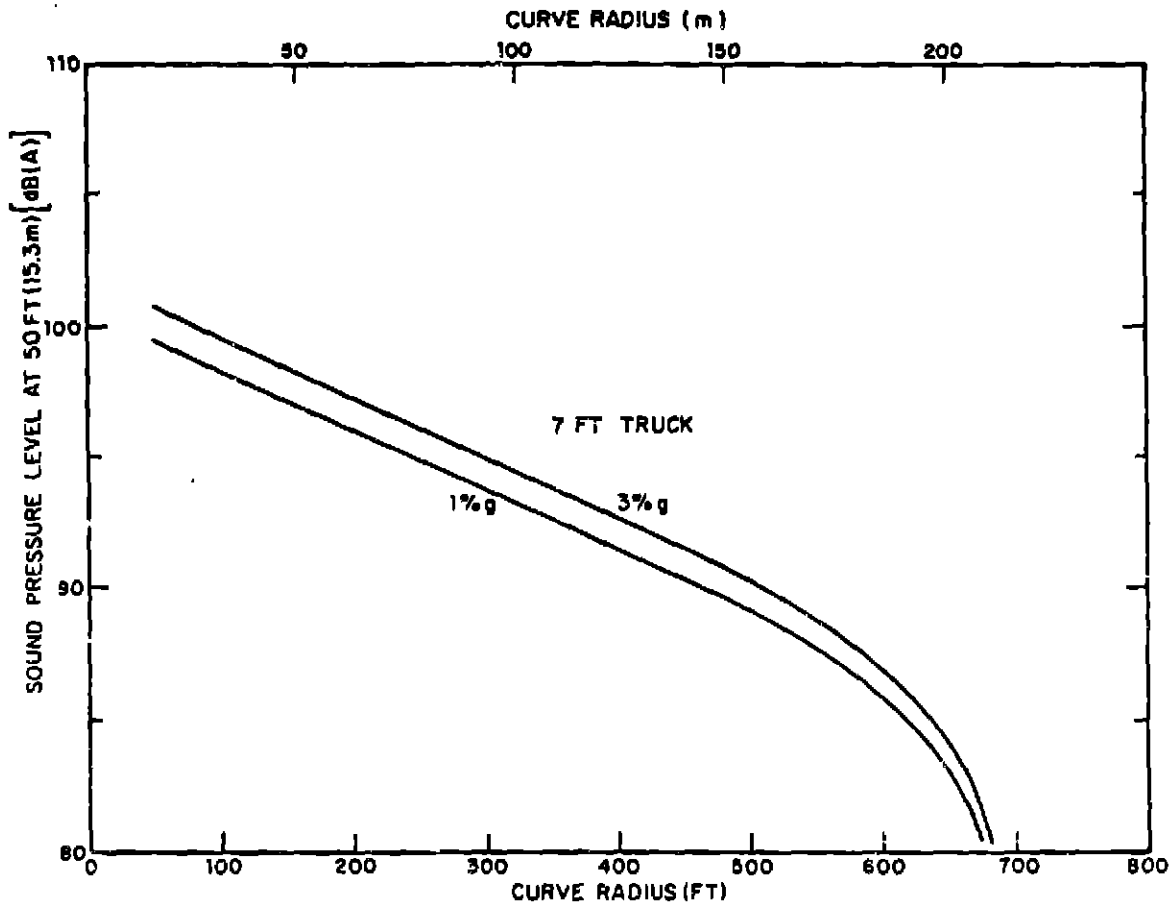
FIG. 2.2-1   SOUND LEVELS OF SQUEAL VS CURVE RADIUS FOR TWO
             LATERAL ACCELERATIONS
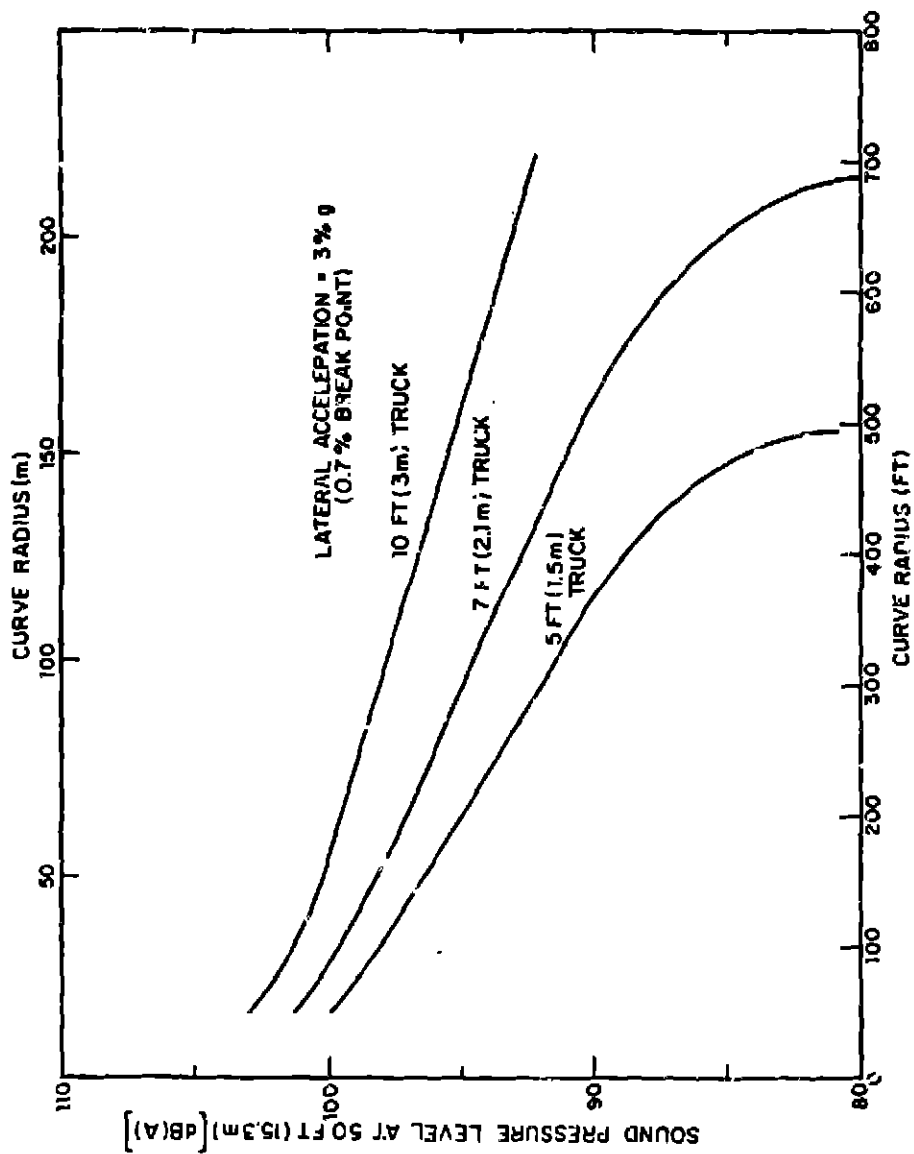
FIG. 2.2-2. SOUND LEVELS OF SQUEAL.

2.2.6 Minimum curve radius to avoid wheel squeal

This model of wheel squeal predicts that the smallest
radius curve that a train can traverse without the wheel squeal-
ing is considerably tighter than the 2000-ft (608 m) radius
at which wheel flanging occurs. Estimates, based upon scarce
data, indicate that the tightest curve is about 100 truck wheel-
bases or 700 ft (213 m). However, this minimum radius can be
affected by the state of the rail and also by the amount of
gage relief employed on the curve. Employing gage relief
actually increases the minimum radius which avoids wheel squeal.
Therefore, this technique is not suitable for noise control.

2.2.7 Preliminary verification of squeal levels on subway systems

Figure 2.2-3 compares the measured sound levels on various
subway systems to the sound levels predicted by the theory.
The curve radius was well documented and varied from 50 ft
(15.2 m) to 500 ft (152 m). However, the speed of the train
in the curve was not well documented. For reasons of passenger
comfort, the lateral acceleration around a curve is generally
kept below about 6% g, with a typical value of 3%. Accordingly,
we calculated the theoretical squeal levels, assuming a speed
such as to give a lateral acceleration of 3% g. The length of
the truck varies from system to system, with a value of 7 ft
(2.13 m) being typical.

The predicted squeal levels appear to correspond to a
maximum of those observed. The explanation could be that the
trains round the curves even more slowly than assumed or that
the stick-slip condition is less severe than assumed in the
model.
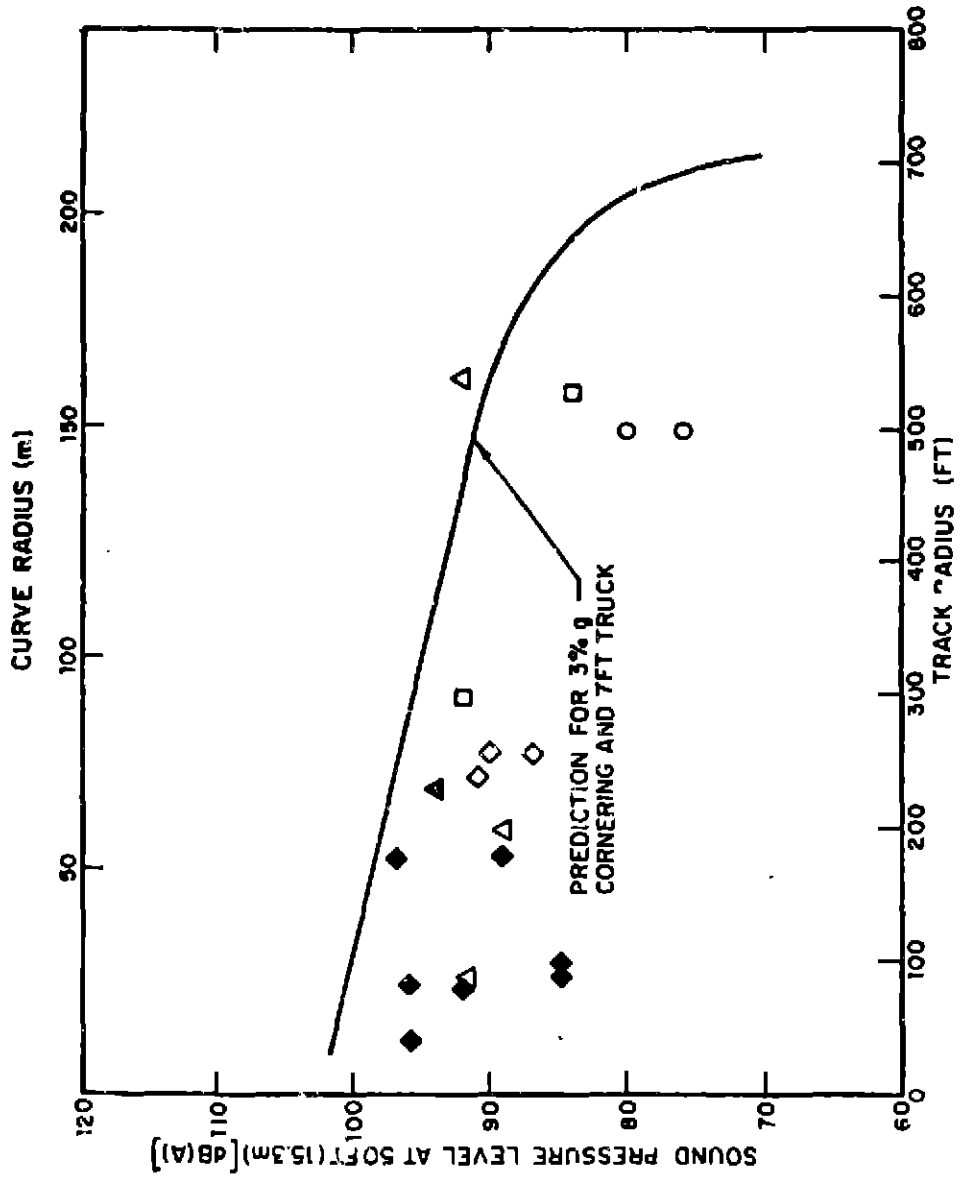
FIG. 2.2-3.   NORMALIZED SQUEAL DATA FROM NINE SYSTEMS.   REMINGTON *et al* (1974).

92

2.3 Impact Noise Predictive Formulas

Impact excitation of the wheel and rail occurs if the contact surface of the rail and/or the wheel has discontinuities. The wheel does not need to separate from the rail to generate impact noise. The impulse excitation response for the sound radiation is characterized by a very short dynamic interaction between the wheel and rail. The duration of the force pulse is controlled by the mass of the wheel, the equivalent mass of the rail, and the Hertzian contact stiffness of the wheel and rail. This impulse force, characterized by the total change in momentum of the impacting wheel and rail, acts simultaneously on both rail and wheel, which respond to this excitation and radiate impulsive noise according to their respective dynamic and acoustic properties.

The dynamics of the rail-wheel impact depends strongly upon whether or not the rail is rigid or resilient. Accordingly, the rigid and resilient rail case will be handled separately. The rigid rail case is less complicated and thus can help to prepare the reader for the more complex resilient rail case.

2.3.1 Rigid rail case

In the case of a rigid rail, by definition, the rail head is not capable of moving and the wheel must either follow the discontinuities of the contact surface or separate temporarily from the rail. Since the magnitude of the generated impact force follows completely different laws depending on whether or not the wheel is separated, we will first establish the criteria for separation.

Criteria for Loss of Contact

Generally, the wheel will separate from the rail whenever the vertical forces (i.e., gravitational and spring forces) acting on the wheel are not capable of producing the vertical acceleration needed to follow the irregularities.

If the vertical position of the rigid rail head y as a function of the distance x along the roadway is described by the function y(x), then, for a constant train speed V, the vertical position of the wheel contact point as a function of time is given by

$$y(x) = y(x = Vt) \; . \qquad (2.3\text{-}1)$$

The separation criterion, based on the fact that the force keeping the wheel in contact with the rail is the wheel loading $P = Mg$ and gravity acting on the wheel mass m, is given by

$$\frac{d^2y}{dt^2} = V^2 \frac{d^2y}{dx^2} \; , \qquad (2.3\text{-}2)$$

$$d^2y/dt^2 = g\left(1 + \frac{M}{m}\right) \; , \qquad (2.3\text{-}3)$$

yielding the critical train speed in general form:

$$V_c = \left[\frac{g(1+M/m)}{d^2y/dx^2}\right]^{\frac{1}{2}} \; . \qquad (2.3\text{-}4)$$

If the rail irregularity has a harmonic spatial variation of the form $A_1 \cos k_1 x = A_1 \cos(2\pi/\lambda_1)x$, Eq. 2.3-4 takes the form of

$$V_c = \frac{\lambda_1}{2\pi} \left|g\left(1 + \frac{M}{m}\right)/A_1\right|^{\frac{1}{2}} \; . \qquad (2.3\text{-}5)$$

Note that for lightly loaded cars, the wheel separation occurs at a lower train speed than for fully loaded cars.

As an example, let us evaluate Eq. 2.3-5 for $\lambda_1 = 0.4$ m (1.3 ft), $A_1 = 2 \times 10^{-3}$ m, and $M/m = 8$, which yield

$$V_c = (0.4/2\pi) (9.81 \times 9 \times 10^3 \times 0.5)^{\frac{1}{2}} = 48 \text{ km/h} = 30 \text{ mph} .$$

This example indicates that for rigid rails even a gently curved rail irregularity of small amplitude can cause wheel separation at reasonably low train speeds.

In the case of a level or step-down rail joint, the wheel may separate from the "upstream" rail end before it impacts on the "downstream" rail. Separation will occur at and above a certain critical train speed $V = V_c$, where the vertical wheel acceleration required to keep the wheel in contact with the upstream rail end cannot be produced by the gravitational and spring forces acting on the wheel. This critical train speed V_c is determined from the kinematics and dynamics of the wheel motion. First, we will determine the vertical component of the wheel velocity and wheel acceleration required to keep the wheel in contact with the downstream rail end as a function of the train speed. The criterion for separation is that the combined gravitational and spring forces acting on the wheel are no longer sufficient to bring about the vertical acceleration required to keep the wheel in contact with the downstream rail.

The kinematic model of the situation is illustrated below:
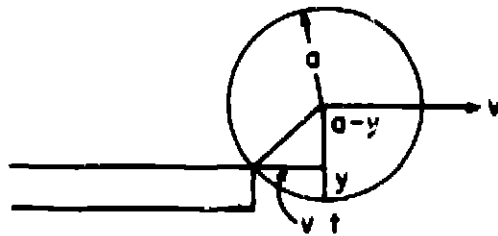
The vertical displacement of the wheel required to maintain contact with the downstream rail as a function of time is given by

$$y(t) = a - (a-y) = a - (a^2-V^2t^2)^{\frac{1}{2}} . \qquad (2.3-6)$$

The vertical velocity is

$$\frac{dy(t)}{dt} = V^2t(a^2-V^2t^2)^{-\frac{1}{2}} \qquad (2.3-7)$$

and the vertical component of the wheel acceleration is

$$\frac{d^2y(t)}{dt^2} = V^2 \frac{1 + \dfrac{V^2t^2}{a^2-V^2t^2}}{(a^2-V^2t^2)^{\frac{1}{2}}} . \qquad (2.3-8)$$

The wheel acceleration in the vertical direction at $t = 0$ is the acceleration that the gravitational and spring forces must be capable of producing to avoid immediate separation. This critical acceleration is given by

$$a_c \equiv d^2y/dt^2(t=0) = \frac{V^2}{a} . \qquad (2.3-9)$$

Since for every practical rail joint the gap w is always negligibly small compared with the wheel radius (i.e., Vt << a), Eq. 2.3-8 can be simplified to

$$\frac{d^2y}{dt^2}(t) \simeq \frac{V^2}{a} \qquad \text{for } 0 < t < w/V \quad . \qquad (2.3-10)$$

Equation 2.3-8 indicates that the vertical acceleration required for retaining contact does not increase significantly from its initial value at t = 0 during the time interval required for the wheel to cross over a typical rail joint. Accordingly, for all practical purposes, the width of the gap w does not influence the critical train speed where separation will occur.

The vertical acceleration that the wheel can achieve is governed by its mass and the gravitational and spring forces acting on it; namely,

$$a_w = g\left(1 + \frac{M}{m}\right) , \qquad (2.3-11)$$

where g is acceleration of gravity, M is the portion of the spring mounted car and truck mass supported by a wheel, and m is the mass of the wheel.

The critical train speed where the wheel will separate from the downstream rail is obtained by equating the two accelerations given in Eqs. 2.3-9 and 2.3-11 respectively and solving for $V = V_c$, yielding

$$V_c = \left| ga\left(1 + \frac{M}{m}\right) \right|^{\frac{1}{2}} . \qquad (2.3-12)$$

97

Equation 2.3-12 indicates that the critical speed increases
with increasing wheel radius and with increasing mass ratio
M/m.

As an example, assume a mass ratio of M/m = 8 and a 15 in.
(37 cm) wheel radius. The speed for separation is

$$V_c = \sqrt{9.81 \frac{m}{sec^2} \, 0.38 \; m(1+8)} = 5.8 \; m/sec$$

$$= 21 \; km/h = 13 \; mph \; .$$

Vertical Wheel Velocity at Impact

For a level joint, the vertical speed of the wheel when
it impacts on the upstream rail is obtained by different
methods below and above critical train speed.

Level joint, below critical train speed

Below the critical train speed, the wheel remains in con-
tact with the downstream rail end as it rolls into the gap.
The axle of the wheel moves on the perimeter of an imaginary
circle of radius a centered on the downstream end of the rail
joint. At the moment of impact, the rail will, for ᵃ ᵛᵉry
short time, have contact with both rail ends. The ᵛl
component of the wheel velocity at the moment of iᵤ an be
calculated from the geometry and from the train speed as shown
schematically in the sketch below.
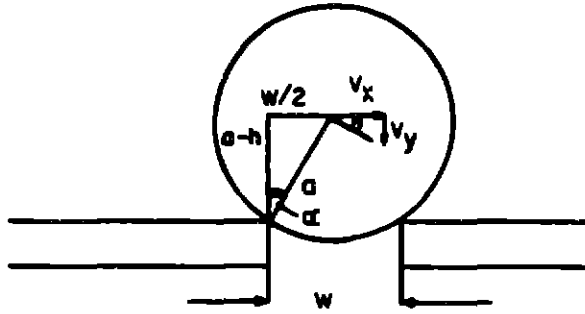
The geometrical similarity of triangle v_x, v_y, v and triangle (a-h), w/2, a provides the needed relationship between v_x and v_y. From the velocity vector triangle, we obtain

$$v_y = v_x tg\alpha \qquad (2.3\text{-}13)$$

and from the geometry we find that

$$tg\alpha = (w/2)/(a-h) . \qquad (2.3\text{-}14)$$

Furthermore, there exists a fixed relationship between a, w, and h, namely:

$$a-h = \left(a^2 - \frac{w^2}{4}\right)^{\frac{1}{2}} . \qquad (2.3\text{-}15)$$

Combining Eqs. 2.3-13, 2.3-14, and 2.3-15, one obtains the vertical velocity of the wheel at the time of impact:

$$v_y = v_x(w/2)\left(a^2 - \frac{w^2}{4}\right)^{-\frac{1}{2}} . \qquad (2.3\text{-}16)$$

Since w/2 << a, for all practical purposes Eq. 2.3-16 can be well approximated by

$$v_y = V \frac{w}{2a} . \qquad (2.3\text{-}17)$$

Note that we have substituted the train speed V for v_x and that v_y increases with increasing train speed and gap width and decreases with increasing wheel diameter.

Level joint, above critical train speed

Above critical train speed, the wheel immediately separates from the downstream end of the rail and takes on a trajectory until it impacts on the upstream rail. The trajectory is determined by the constant train speed V in the horizontal direction and the parabolically increasing vertical velocity due to the action of the gravitational and spring forces acting on the wheel in the vertical direction, namely.

$$v_y(t) = g\left(1 + \frac{M}{m}\right)t \equiv g't \ . \qquad (2.3\text{-}18)$$

The time of impact is obtained from geometrical considerations as shown in the sketch below.
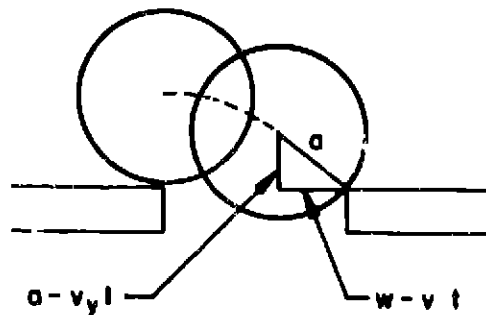
Observing the above sketch, one notes the following relationship at the moment of impact:

$$a^2 = \left(a - \frac{g't^2}{2}\right)^2 + (w\text{-}Vt)^2 \ . \qquad (2.3\text{-}19)$$

Solving Eq. 2.3-18 for t and inserting this value into
Eq. 2.3-19 yields the following relationship between the verti-
cal component of the wheel velocity at the impact (v_y) and the
train speed:

$$v_y^4 \frac{1}{4g'^2} + v_y^2 \left(\frac{V^2}{g'^2} - \frac{2a}{g'} \right) - v_y \left(\frac{2wV}{g'} \right) + w^2 = 0 \ . \qquad (2.3-20)$$

This equation can be solved for particular values of V, a, and
w, but it is not very useful in providing a general overview.

An approximate relationship between v_y and V can be ob-
tained by assuming that the transit time of the wheel is
$t \approx w/V$. With this value of t, Eq. 2.3-18 yields the approxi-
mate vertical velocity of the wheel at the moment of impact:

$$v_y \leq g \left(1 + \frac{M}{m} \right) \frac{w}{V} \ . \qquad (2.3-21)$$

Equation 2.3-21 indicates that v_y increases with increasing gap
width but decreases with increasing train speed. The decrease
of v_y with increasing train speed is attributable to the fact
that the time available for the wheel to gather a vertical
speed due to the gravitational and spring forces acting on it
during its "flight" over the rail joint decreases with increas-
ing train speed.

Since observations indicate that the impact noise at rail
joints increases rather than decreases with increasing train
speed, one can draw the following conclusions.

1. Rail joints should be maintained as level as possible
to reduce impact noise.

2. Most probably the lack of leveling is responsible for
the impact noise at practical rail joints.

101

Accordingly, the next sections of our investigation will deal
with the analytical modeling of rail joints which are not level.

Step-down joint

For a step-down joint, as sketched below, the wheel will
roll down the joint at low train speeds and will take on a tra-
jectory when the train speed exceeds the critical train speed.
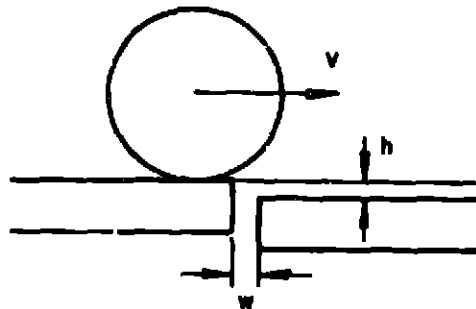
Step-down joint, above critical train speed

If the train speed exceeds the critical speed given in
Eq. 2.3-12, the wheel immediately separates from the downstream
rail and its vertical velocity at the impact is determined by
the action of the gravitational and spring forces which accel-
erate the wheel during its fall. The vertical velocity of the
wheel is given by

$$v_y(t) = a_w t = F\left(1 + \frac{M}{m}\right)t \ , \qquad (2.3\text{-}22)$$

where $t = 0$ corresponds to the time when the axle is exactly
above the upstream rail end. The average velocity i

$$\bar{v}_y(t) = \frac{1}{2} F\left(1 + \frac{M}{m}\right)t \ . \qquad (2.3\text{-}23)$$

The time of impact is given by

$$t_{imp} = \frac{h}{\bar{v}_y} = \sqrt{\frac{2h}{g(1 + M/m)}} \ . \tag{2.3-24}$$

The combination of Eqs. 2.3-23 and 2.3-24 yields the vertical velocity of the wheel at the time of impact:

$$v_y = \sqrt{2hg(1 + M/m)} \ . \tag{2.3-25}$$

Note that v_y increases with increasing vertical rail displacement h and with increasing axle load M, but that it is independent of the train speed.

In deriving Eq. 2.3-25 we have assumed that the width of the gap w is small enough that the wheel completely "jumps" the gap. It is easy to show that this is always the case if train speed obeys the relationship given in Eq. 2.3-26:

$$V \geq w\sqrt{\frac{g\left(1 + \frac{M}{m}\right)}{h}} \ . \tag{2.3-26}$$

At and above the critical train speed $V = V_c$ as given in Eq. 2.3-12, Eq. 2.3-26 yields the following geometrical requirement:

$$h \geq \frac{w^2}{a} \left(\frac{V_c}{V}\right)^2 \qquad \text{for} \quad V \geq V_c \ . \tag{2.3-27}$$

For a typical gap width of 0.25 in. (.635 cm) and a typical wheel radius of 15 in. (37 cm), at critical speed Eq. 2.3-27 requires that the step-down height h must be larger than 0.004 in. (0.1 mm). Accordingly, for all joints which

may be classified as step-down joints, one can apply Eq. 2.3-25 to calculate the vertical velocity of the wheel at the time of impact for all train speeds which exceed the critical train speed.

Equation 2.3-27 also indicates that for speeds above critical speed, very small height differences are sufficient to yield a complete jump of the wheel over the joint.

Step-down joint, below critical train speed

If the train speed is below the critical speed required for immediate separation of the wheel from the downstream rail end, the kinematics of the situation can be described as follows: The wheel starts to roll down the rail downstream of the joint, retaining contact until it separates from the upstream rail and takes on a trajectory before the impact. Whatever the case, the vertical speed of the wheel at the time of impact is always smaller than that given in Eq. 2.3-25 for the critical speed.

For small gaps where $w < (2ah-h^2)^{\frac{1}{2}}$, the vertical velocity of the wheel at the time of impact can be calculated from the geometry and from the train speed as shown schematically in the sketch below.
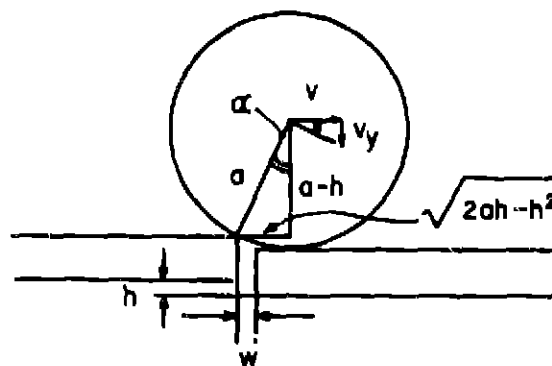
The sketch indicates that

$$v_y = V tg\alpha = V \frac{\sqrt{2ah-h^2}}{a-h} .$$ (2.3-28)

Since $h \ll a$, Eq. 2.3-28 simplifies to

$$v_y \approx \sqrt{\frac{2h}{a}} V \qquad \text{for } V < V_c .$$ (2.3-29)

To gain some insight into the relative importance of the rolling and separated wheel traverse in respect to the vertical velocity achieved by the wheel at the time of impact, let us consider the ratio of these vertical speeds for rolling and for traverse at the critical train speed as given in Eq. 2.3-12:

$$\frac{v_{y_R}(V = V_c)}{v_{y_T}} = \frac{\sqrt{\frac{2h}{a}} \sqrt{ag\left(1 + \frac{M}{m}\right)}}{\sqrt{2hg\left(1 + \frac{M}{m}\right)}} ,$$ (2.3-30)

yielding

$$\frac{v_{y_R}(V = V_c)}{v_{y_T}} = 1 ,$$ (2.3-31)

indicating a smooth transition from rolling to separation.

Step-up joint

The geometry of a rigid step-up rail joint and the vector components of the wheel velocity at the moment of impact are illustrated in the sketch below.
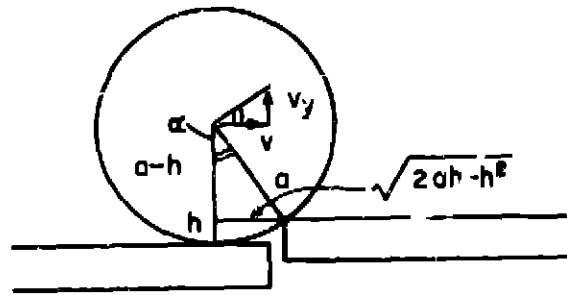
The velocity vector triangle indicates that at the moment of impact, the wheel has to have a vertical velocity v_y to roll up on the upstream rail end:

$$v_y = \text{vtg}\alpha = v\,\frac{\sqrt{2ah-h^2}}{a-h}\,.\tag{2.3-32}$$

Considering that a >> h, Eq. 2.3-32 simplifies to

$$v_y \approx v\,\sqrt{\frac{2h}{a}}\,.\tag{2.3-33}$$

Note that this velocity equals in magnitude the vertical wheel velocity acquired by the wheel when it rolls down a step-down joint of the same height difference when the wheel retains contact with the downstream rail end (see Eqs. 2.3-28 and 2.3-29). The basic difference is that for a step-down joint, at low train speeds, the vertical speed of the wheel increases gradually until it reaches its maximum value at the event of impact, while in the case of a rigid step-up joint, the wheel would be required to change its vertical velocity suddenly from zero to the value given in Eq. 2.3-33 at the moment when the wheel impacts on the upstream rail end. As indicated in the sketches below, this sudden change of vertical speed would require a semi-infinite wheel acceleration.

v_y

$v \sqrt{2h/a}$

t

a_y

$\delta(t) \, v \sqrt{2h/a}$

t

$\sqrt{2ah - h^2}/v$
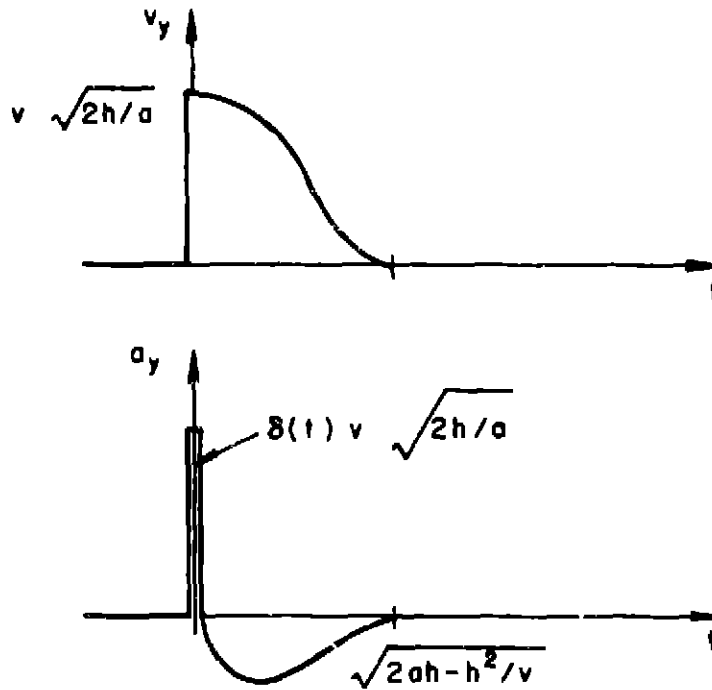
Since the rail is not infinitely rigid, it will deform to
at least partly accommodate the impacting wheel mass, and the
change in the vertical velocity of the wheel will be fast but
not discontinuous. One would thus expect the time history of
the vertical wheel velocity to have a finite initial slope.

The relative importance of the height difference and gap
width can be found by taking the ratio of the impact velocities
as given in Eq. 2.3-17 and 2.3-13 respectively, which yields

$$\frac{\dot{y}_{level}}{\dot{y}_{step}} = \frac{w}{(2ah)^{1/2}} \qquad (2.3-34)$$

Equation 2.3-34 indicates that in order to produce the same im-
pact velocity, the gap of a level joint and the height differ-
ence of a step-up joint must satisfy Eq. 2.3-34:

164

$$h = \frac{w^2}{8a} \ . \qquad\qquad (2.3\text{-}35)$$

For example, a step-up joint with a height difference of
$h = 5 \times 10^{-4}$ in. (.012 mm) produces an impact velocity which is
equivalent to a gap of $w = 0.25$ in. (0.635 cm) of a perfectly
level joint. This example clearly indicates the predominant
nature of the height differences as compared with the gap width
of a level joint.

Based on Eq. 2.3-35, one can safely conclude that as long
as the joined rails are aligned, the gap widths usually found
in practice have a negligible effect on the noise generation.
Practically always, the lack of vertical and/or horizontal
alignment is responsible for the impact noise generated by rail
discontinuities. The horizontal misalignment of the joined
rail ends may contribute to the vertical impact because of the
conical shaping of the wheel tread. Since horizontal misalign-
ments are especially dangerous for ride stability, railroads
usually have tight specifications for this type of misalignment,
so that their contribution to vertical impacts may be negli-
gible.

Wheel flats

The impact behavior of wheel flats is similar to that ob-
served for rigid step-down rail joints. At low train speeds,
the upstream end of the flat, designated 1 in the sketch
below, retains contact with the rail and the wheel axle moves
on a circular path of radius a centered on contact Point 1
until the other end of the flat, designated by 2, impacts on
the rail. From this moment on, the wheel takes on another
circular path of radius a centered around contact Point 2 until

the center line of the wheel axle passes over this contact point. After this, the round portion of the wheel comes into contact with the rail while the axle position remains level.
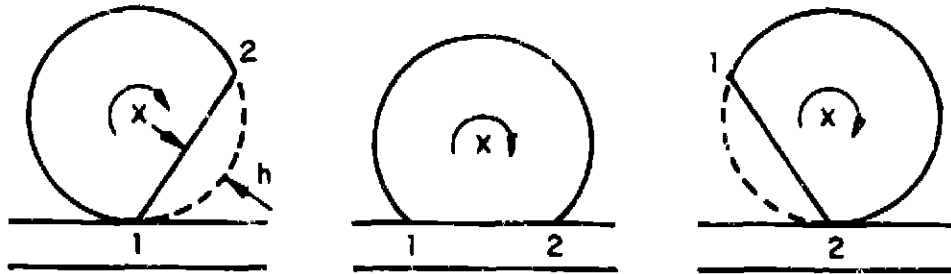
below the critical train speed given in Eq. 3.2-12, the wheel remains contact with the rail. The vertical wheel velocity at impact v_y is obtained from comparison of the two equal-angle triangles shown in the sketch below, yielding

$$v_y = V (2h/a)^{\frac{1}{2}} \qquad \text{for} \quad V \leq V_c . \qquad (3.3-36)$$
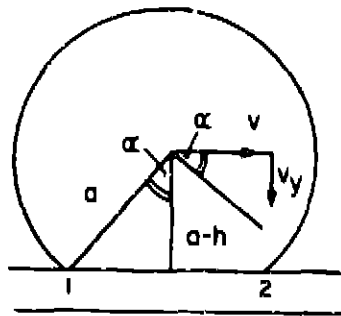
At the instant when Point 2 contacts the rail, the velocity of the wheel center point changes direction from downward to upward. The total change of wheel velocity is according to twice

the impact velocity of the wheel given above. Accordingly, the total change in momentum is given by

$$mdv_W = 2mv_y = 2mV \, (2h/a)^{\frac{1}{2}} \qquad \text{for} \quad V \leq V_c \, . \quad (2.3\text{-}37)$$

Above the critical train speed, the wheel immediately loses contact with the rail when the flat is reached, and the rotating wheel takes on a trajectory determined by the train speed and the spring-and-inertia forces acting on the wheel. Both the time of the impact and the impact velocity will depend not only on the flat height h, the wheel radius a, and the axle loading, but also on the angular position of the wheel at the end of the separation time.

After a straightforward but lengthy calculation, one can show that above the critical speed the total change in momentum is given by

$$mdv_W = 2mV_c \qquad \text{for} \quad V \geq V_c \, , \qquad (2.3\text{-}38)$$

where V_c is the critical train speed given in Eq. 2.3-12. It is interesting to note that the increase of impact due to the higher rotation rate is exactly compensated for by the shorter separation time, which reduces the vertical velocity the wheel gathers during its separation because of the gravitational and spring forces acting on it.

2.3.2 Resiliently supported rail

The resilient support of the rail by an elastic ballast bed or by elastic rubber mounts is of primary importance in reducing the dynamic loading of both the rail and wheel. It has been shown that the static and dynamic behavior of rail

mounted on tie and ballast as well as resiliently mounted rail can be well described by a beam resting on an elastic foundation (Timoshenko, 1926; Dörr, 1948; Crandall, 1959).[*] The differential equation describing the free rail motion is given by (Timoshenko, 1926)

$$EI \frac{d^4 y}{dx^4} + \rho_\ell \frac{d^2 y}{dt^2} + Ky = 0 , \qquad (2.3-39)$$

where y is the vertical rail displacement, x is the distance along the rail, E is the Young's modulus and I the moment of inertia of the rail cross section, ρ_ℓ is the mass of rail per unit length, and K is the force per unit rail length required to produce unit rail displacement. The last quantity is often referred to as the foundation modulus in railroad engineering terminology.

The form of rail displacement due to a static force of F_0 acting at $x = 0$ on the rail is given by (Timoshenko, 1926)

$$y(x) = \frac{F_0 \beta}{2K} e^{-\beta x} (\cos\beta x + \sin\beta x) , \qquad (2.3-40)$$

where

$$\beta = \left(\frac{K}{4EI} \right)^{\frac{1}{4}} . \qquad (2.3-41)$$

The frequency of free rail vibrations is

$$\omega_0 = \left(\frac{K}{\rho_\ell} \right)^{\frac{1}{2}} . \qquad (2.3-42)$$

---

[*]Section 2.1 shows that at high frequency the rail can be modeled even more simply as an infinite beam.

For sinusoidal forcing the rail displacement can be obtained by replacing the static foundation modulus by its dynamic equivalent:

$$K_d = K\left(1 - \frac{\omega^2}{\omega_0^2}\right) . \qquad (2.3\text{-}43)$$

Equation 2.3-43 indicates that below the resonance frequency ω_0 the rail displacement is controlled by the foundation stiffness and that well above ω_0 the rail acts like an infinite beam.

Critical Train Speed

The vertical acceleration needed to overcome the curvature of the loaded rail is obtained by inserting $x = Vt$ into Eq. 2.3-40 and differentiating it twice in respect to t, yielding

$$\frac{d^2 y}{dt^2} = \frac{F_0}{K} \beta^3 V^2 e^{-\beta Vt} (\sin\beta Vt - \cos\beta Vt) . \qquad (2.3\text{-}44)$$

The initial vertical acceleration needed for the wheel to follow this curvature of the rail is obtained by combining Eqs. 2.3-40 and 2.3-44, resulting in

$$\ddot{y}_c(t=0) = -y_0 \beta^2 V^2 , \qquad (2.3\text{-}45)$$

where $y_0 = F_0 \beta/(2K)$ is the static deflection of the rail under the static load F_0. The initial vertical acceleration of the rail when it is suddenly freed from the static load can be approximated by

$$\ddot{y}_R(t) \cong \omega_0^2 y_0 \ .$$

If a perfectly round wheel travels over an elastically supported rail with a rail head irregularity characterized by the radius of curvature, d^2y/dx^2, the wheel will separate from the rail when the upward acceleration $(d^2y/dx^2)V^2$ becomes equal to the sum of the downward wheel accelerations due to the gravity and spring forces $g(1 + M/m)$, the upward acceleration of the suddenly freed rail $\omega_0^2 y_0$, and the upward acceleration of the wheel needed to overcome the "uphill" deformation of the rail due to the static load; namely, if

$$g(1 + M/m) + \omega_0^4 y_0 + 2y_0 \beta^2 V^2 = V^2(d^2y/dx^2) \ . \quad (2.3\text{-}46)$$

Solving Eq. 2.3-46 for V yields the critical train speed for the elastically supported rail:

$$V_{CE} = \left[g(1+M/m) \bigg/ \frac{d^2 y}{dx^2} \right]^{1/2} \left[\frac{1 + \frac{m}{\rho_\ell} \frac{\beta}{2}}{1 - \frac{2y_0 \beta^2}{d^2y/dx^2}} \right]^{1/2} \ . \quad (2.3\text{-}47)$$

Note that the first term on the right side of Eq. 2.3-47 is exactly the critical speed for the equivalent rigid rail V_{CR} as given in Eq. 2.3-4. Since $d^2y/dx^2 > 2y_0 \beta^2$ is a necessary requirement for separation, the second term on the right side of Eq. 2.3-47 is always larger than unity. Accordingly, *the critical speed of an elastically mounted rail is always larger than that of an equivalent rigid rail.* Furthermore, one can show that for typical tracks the denominator in the second term of Eq. 2.3-47 does not differ much from unity and V_{CE} can be

well approximated by

$$V_{CE} \simeq V_{CR}\left(1 + \frac{m}{\rho_\ell}\frac{\beta}{2}\right)^{\frac{1}{2}},$$ (2.3-48)

where V_{CR} is given in Eq. 2.3-4.

Evaluating Eq. 2.3-48 for $m = 880$ lb (400 kg), $\rho_\ell = 100$ lb/yd (50 kg/m), $k = 8.5 \times 10^5$ lb/ft² (3.5×10^7 N/m²), $E = 30 \times 10^6$ lb/in.² (2.18×10^{11} N/m²), a.id $I = 49$ in.⁴ (2×10^{-5} m⁴) yields $V_{CE} = 2.2 V_{CR}$, indicating a more than twofold increase in critical speed from rigid to resilient rail.

The critical train speed for step-down rail joints and flat wheels is obtained by replacing $V^2(d^2y/dx^2)$ on the right side of Eq. 2.3-46 by V^2/a and solving for V, yielding

$$V_{CE} = [ga(1+M/m)]^{\frac{1}{2}}\left(1 + \frac{m}{\rho_\ell}\frac{\beta}{2}\right)^{\frac{1}{2}}.$$ (2.3-49)

Here again, the first term on the right side of the above equation is exactly the critical speed for the equivalent rigid rail case, V_{CR}, as given in Eq. 2.3-12. The second term, which indicates the extent of increase in critical speed for the elastically supported rail above the critical speed of the equivalent rigid rail, is the same as in Eq. 2.3-48.

Wheel Impact

Below critical speed the wheel retains contact with the rail. In contrast to the rigid rail case, where the wheels have to follow the shape of the irregularity, in the case of an elastically supported rail both wheel and rail deform and

move up or down in order to follow the shape of the disconti-
nuity. The degree to which each deforms or moves out of the way
depends on their relative impedances. It was shown in Sec. 2.1
that below 1000 Hz the wheel impedance is much greater than
the rail impedance. In addition, as will be shown in Sec. 3.2,
the duration of the impact is generally on the order of a few
milliseconds, implying that most of the frequency content is
below 1000 Hz. As a result, one would expect that during im-
pact the wheel virtually retains the vertical position while
the more deformable rail is pushed down (or permitted to lift
up).

Although Sec. 2.1 has shown that the rail is best modeled
as a beam above the resonance frequency ω_0, considerable sim-
plification with minimal loss in accuracy can be obtained by
modeling the rail with an equivalent mass. Accordingly, the
formulas describing the impact caused by the various disconti-
nuities for elastically supported rail are obtained by replac-
ing the wheel mass m by the equivalent impact mass of the rail
m_{eq} in the corresponding formulas derived for the rigid rail
case.

The equivalent impact mass of an elastically supported rail
has been calculated by Jenkins (1974) as

$$m_{eq} = \rho_\ell [\Gamma(0.75)\Gamma(1.25)\sqrt{2}]^{7/3} \left(\frac{4EI}{k_H}\right)^{1/6} , \qquad (2.3\text{-}50)$$

where k_H is the Hertzian contact stiffness. For typical values
of k_H and EI, Eq. 2.3-50 yields (Jenkins, 1974)

$$m_{eq} = 0.4 \; \rho_\ell , \qquad (2.3\text{-}51)$$

where ρ_ℓ is the mass of one meter length of rail.

Above the critical speed given in Eqs. 2.3-47 and 2.3-49, the wheel will separate from the rail. To restore the rail deformation caused by the formerly applied static load, the rail moves upwards with initial velocity which can be approximated by

$$v_r(t) = y_0 \omega_0 \ . \tag{2.3-52}$$

Assuming that the heavy wheel will not change its vertical position during the short time of separation and that the height difference h is small compared with the static deflection of the rail y_0, the time of separation t_{imp} can be calculated as

$$\int_0^{t_{imp}} v_r(t)dt = h = -y_0(1 - \cos\omega_0 t) \ , \tag{2.3-53}$$

yielding

$$t_{imp} = \frac{1}{\omega_0} \left(\frac{2h}{y_0}\right)^{\frac{1}{2}} \ . \tag{2.3-54}$$

Inserting this value of t into Eq. 2.3-52 yields the rail speed at instant of impact:

$$v_r(t_{imp}) = y_0 \omega_0 \left[1 - \left(1 - \frac{h}{y_0}\right)^2\right]^{\frac{1}{2}} \ . \tag{2.3-55}$$

At the time of impact, the rail and wheel have momentums which are approximately of the same magnitude but opposite in phase. Accordingly, both bodies virtually lose their velocity at the collision and the total change in momentum can be well approximated by

$$2v_r(t_{imp})m_{eq} \approx 2y_0 m_{eq}\omega_0 \left| 1 - \left(1 - \frac{h}{y_0}\right)^2 \right|^{\frac{1}{2}} . \qquad (2.3\text{-}56)$$

Combining Eqs. 2.3-40, 2.3-41, 2.3-42, and 2.3-56, one can
show that the total change in momentum is

$$2v_r(t_{imp})m_{eq} \doteq 2\sqrt{2hm_{eq}F_0} . \qquad (2.3\text{-}57)$$

*Accordingly, the impact sound generated increases with
increasing height difference, increasing impact mass of rail,
and increasing axle load. Since axle load and rail mass are
usually determined by static considerations, the only param-
eter available for controlling the impact noise at train speeds
above critical speed is the height difference h.*

The impact formulas for elastically mounted rail are sum-
marized in Table S.2 on page xxxiv.

2.3.3 Preliminary verification of impact formulas

Limited scale-model and full-scale experiments have been
carried out to verify the impact formulas presented in the
previous two sections. As discussed in deta in Sec. 3.3,
the results of these preliminary experiments indicate that the
analytical model properly describes the dependence of the peak
sound pressure caused by rail discontinuities on train speed,
geometry, and the dynamical characteristics of the wheel and
rail.

No experiments have been carried out to verify the impact
noise model for flat wheels. However, the close geometric
similarity between the wheel flats and step-down rail joints
makes it very likely that the analytical model for predicting
impact noise caused by flat wheels is also correct.

2.4 Roar Noise Predictive Formulas

Roar or rolling noise is the name given to the wheel/rail noise produced by the microroughnesses on wheels and rails. In this section, we analyze the vibration caused by these wheel and rail roughnesses and estimate the wheel response, rail response, and sound radiation, drawing heavily on the simple models and measurements described in Sec. 2.1.

2.4.1 Wheel/rail interaction and response

In order to determine how wheel and rail roughnesses generate vibration, consider a smooth wheel moving along a rail at constant velocity, V. If the wheel encounters a bump on the rail, the whe ι will be deflected upward and the rail downward by amounts that depend on the size of the bump and upon wheel and rail resistance to motion (impedance). If wheel/rail contact is maintained, the sum of wheel and rail displacements is equal to the height of the bump.

Figure 2.4-1 illustrates the general case of a rough wheel rolling with a speed V along a rough rail. The roughnesses of the wheel and rail are shown as (exaggerated) perturbations of a smooth circular wheel and smooth rail surface. At any instant, the vertical position of the wheel reference circle, y_w, depends on the position, $y_{\_}$, of the rail, and on the wheel and rail roughnesses, w and r, which are measured with respect to the smooth wheel and rail reference lines:

$$y_w = y_r + r + w .\qquad (2.4-1)$$

When both sides of Eq. 2.4-1 are differentiated with respect to time, wheel velocity v_w is defined as positive upward, and rail velocity v_r as positive downward, the following relationship
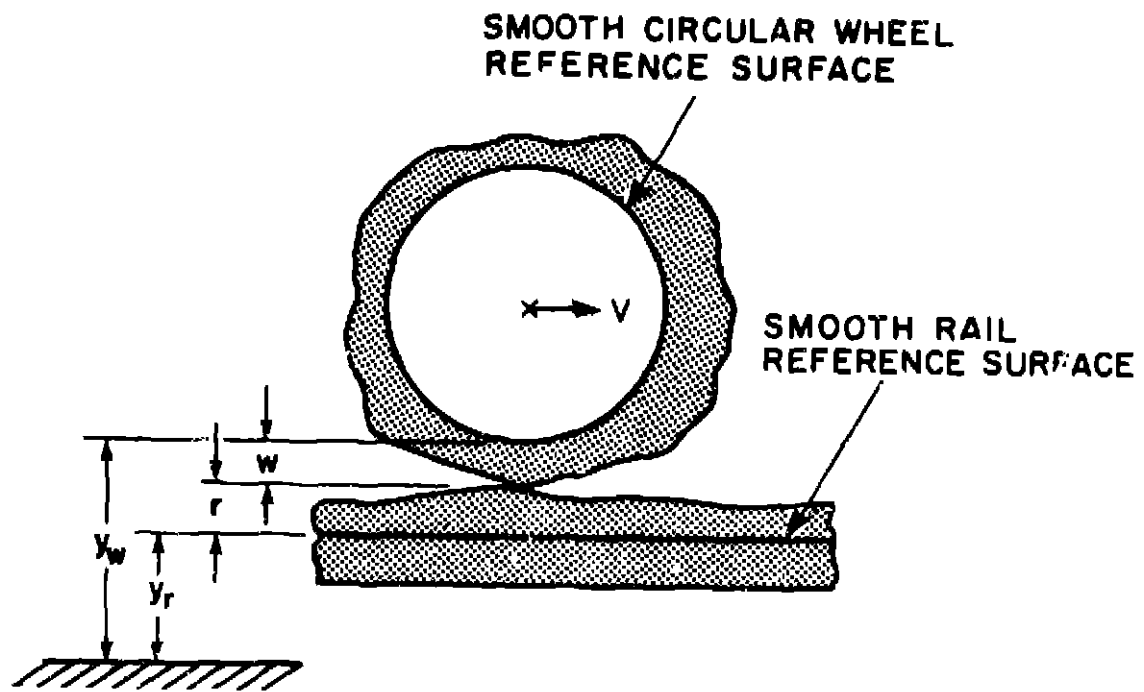
FIG. 2.4-1.   WHEEL/RAIL INTERACTION.

applies between wheel and rail velocity and the rate of change
of wheel and rail roughness due to motion of the contact point:

$$v_W + v_r = \dot{r} + \dot{w} . \qquad (2.4-2)$$

If the roughness of the wheel and rail is a sinusoidal function of
frequency ω, then the amplitude of the sinusoidal vertical force,
$F(\omega)$, at the wheel/rail interface can be related to the amplitudes
of the sinusoidal wheel and rail velocities V_W and V_r respectively
as

$$F(\omega) = Z_W V_W = Z_R V_r , \qquad (2.4-3)$$

where Z_W and Z_R denote the point impedances of the wheel (con-
nected to the vehicle) and rail (*in situ*) at frequency ω,
respectively.

When we solve Eqs. 2.4-2 and 2.4-3 for the interaction
force and resulting wheel and rail velocities at the contact
point in terms of the roughnesses, we obtain

$$F(\omega) = \frac{Z_R Z_W}{Z_R + Z_W} [\dot{r}(\omega) + \dot{w}(\omega)] , \qquad (2.4-4)$$

$$V_W(\omega) = \frac{Z_R}{Z_R + Z_W} [\dot{r}(\omega) + \dot{w}(\omega)] \qquad (2.4-5)$$

and

$$V_r(\omega) = \frac{Z_W}{Z_R + Z_W} [\dot{r}(\omega) + \dot{w}(\omega)] . \qquad (2.4-6)$$

In fact, the rail roughness is a random variable, and it may
justifiably be characterized as a stationary random process
with a wavenumber spectrum, $\phi_{rr}(k)$. Here, k denotes wavenumber.

More care must be exercised in characterizing the wheel roughness. If the roughness were uniform across the running surface but varied circumferentially, it would be characterized completely by a Fourier series. However, since lateral profile variations are significant, one would not expect the circumferential roughness pattern to be repetitive as the wheel oscillates laterally over a rail which also contains lateral irregularities. Accordingly, we can also model the wheel roughness as a stationary random function. By doing so, we can write a simple expression for the relationship between the frequency spectra of dependent variables involving interaction forces (e.g., wheel velocity and rail velocity) and of independent variables (e.g., wheel and rail roughness velocities).* However, the frequency spectra of wheel and rail roughness velocities depend on the speed with which the wheel travels over the rail. It is more convenient to deal with an invariant measure of the roughness. Such a measure is the wavenumber spectrum of the magnitude of the roughness.

The relation between a frequency and wavenumber spectrum is given by

$$\phi_{tt}(\omega)d\omega = \phi_{xx}(k)dk .\qquad (2.4-7)$$

Equation 2.4-7 reflects a requirement for equal mean-square values in corresponding frequency and wavenumber bands. Since $\omega = kV$,

---

*The spectrum, $\phi_{jj}(\omega)$, of a dependent variable is related to the spectrum, $\phi_{ii}(\omega)$, of an independent variable by $\phi_{jj}(\omega) = |H(\omega)|^2 \cdot \phi_{ii}(\omega)$, where $H(\omega)$ is the transfer function relating two variables. Equations 2.4-4, 2.4-5 and 2.4-6 provide the required transfer functions as ratios of the wheel and rail impedances.

$$\Phi_{tt}(\omega) = V^{-1}\Phi_{xx}(\kappa) \ .\qquad\qquad (2.4\text{-}8)$$

Since a velocity spectrum is simply ω^2 times the displacement spectrum, we may apply Eq. 2.4-8, along with the general relation between an input and output spectrum, to Eqs. 2.4-4 - 2.4-6 to obtain:

$$\Phi_{FF}(\omega) = \frac{\omega^2}{V}\left|\frac{Z_R Z_W}{Z_R + Z_W}\right|^2 [\Phi_{rr}(k) + \Phi_{WW}(k)] \ ,\qquad (2.4\text{-}9)$$

$$\Phi_{V_W V_W}(\omega) = \frac{\omega^2}{V}\left|\frac{Z_R}{Z_R + Z_W}\right|^2 [\Phi_{rr}(k) + \Phi_{WW}(k)]\qquad (2.4\text{-}10)$$

and

$$\Phi_{V_r V_r}(\omega) = \frac{\omega^2}{V}\left|\frac{Z_W}{Z_R + Z_W}\right|^2 [\Phi_{rr}(k) + \Phi_{WW}(k)] \ .\qquad (2.4\text{-}11)$$

While Eqs. 2.4-9 to 2.4-11 seemingly suggest that at a given frequency the force and velocity spectra decrease with increasing vehicle speed, this is not the case. Since $\kappa = \omega/V$, one can see that at a given frequency an increase in speed implies a decrease in wavenumber. As a result, the way the spectra of interaction force and wheel and rail velocities vary with train speed depends intimately on the character of the wheel and rail roughnesses.

If one were to measure wheel and rail roughness spectra and use Eqs. 2.4-9 - 2.4-11 to predict wheel and rail velocity and interaction force, he would be in considerable error at high frequencies. This error results from the fact that when

the wheel of a rapid transit car rests on the rail the contact
area between the two is finite in size. Consequently, those
components of the roughness spectrum that have wavelengths on
the order of the dimensions of the contact patch area are ef-
fectively filtered or averaged out. We discuss this concept
in more detail below.

Contact Patch Wavenumber Filtering

When a rapid transit car wheel rests on a rail, the local
elastic deformations on the surface of the wheel and rail pro-
duce a finite area over which the wheel and rail are in intimate
contact. The area of contact is usually an ellipse in shape,
the major and minor axes of which depend on the loading applied
to the wheel, P, the modulus of the materials in the wheel, E_w,
and rail, E_r, the radius of the wheel, a_w, and the radius of
curvature on the head of the rail, a_r. Formulas for calculat-
ing these axes can be found in Timoshenko and Goodier (1951,
Chap. 13, Article 125). The form of the equations for the
length of the axes of the ellipse is

$$\sqrt[3]{\frac{3}{2} P \frac{a_w a_r}{a_w + a_r} \left(\frac{1-\nu_w^2}{E_w} + \frac{1-\nu_r^2}{E_r} \right)}, \qquad (2.4-12)$$

which shows a weak dependence on all of the above quantities.
A typical transit car wheel 30 in. (76 cm) in diameter under
10,000 lb (44,500 N) load resting on a rail with a radius of
curvature on the head of 12 in. (30 cm) produces a contact
patch ~0.32 in. x 0.26 in. (8 mm x 6.6 mm).

As the running surface of the wheel passes through the con-
tact patch and the contact patch moves over the surface of the
rail those components of the roughness spectrum whose wavelengths
are much greater than the dimensions of the contact patch are

essentially unaffected. Those components whose wavelengths are less than or on the order of the dimension of the contact patch may be considerably attenuated, simply from an averaging process over the area of the contact patch. Not only the wavelength along the rail is important in this averaging process. The degree of correlation between roughness profiles measured in parallel paths along the rail and around the wheel is also important in determining the degree of wavenumber filtering. If parallel paths separated by a distance on the order of the lateral dimension of the contact patch are well correlated, then the contact patch is a less effective wavenumber filter than in the case where paths separated by that amount are poorly correlated.

Appendix B presents the detailed mathematics for the derivation of the characteristics of the contact patch wavenumber filter. It is shown that for a circular contact patch of radius b, the filter transfer function is given by

$$\left| H_{cp}(k_x) \right|^2 = \frac{4}{\alpha} \frac{1}{(k_x b)^2} \int_0^{\tan^{-1}\alpha} J_1^2(k_x b \sec\psi) d\psi , \quad (2.4-13)$$

where k_x is the wavenumber along the length of the rail or around the circumference of the wheel and α is a constant determining the degree of correlation between parallel roughness profiles at a given wavenumber (see Appendix B). Large α implies poor correlation and small α implies strong correlation.

Equation 2.4-13 has been numerically integrated for various values of α and is presented in Fig. 2.4-2. When one examines the curve $\alpha = 10$, it is apparent that significant filtering can occur. When wavelengths are on the order of 2 times the diameter of the contact patch ($kb = 1$) 10 dB reduction in
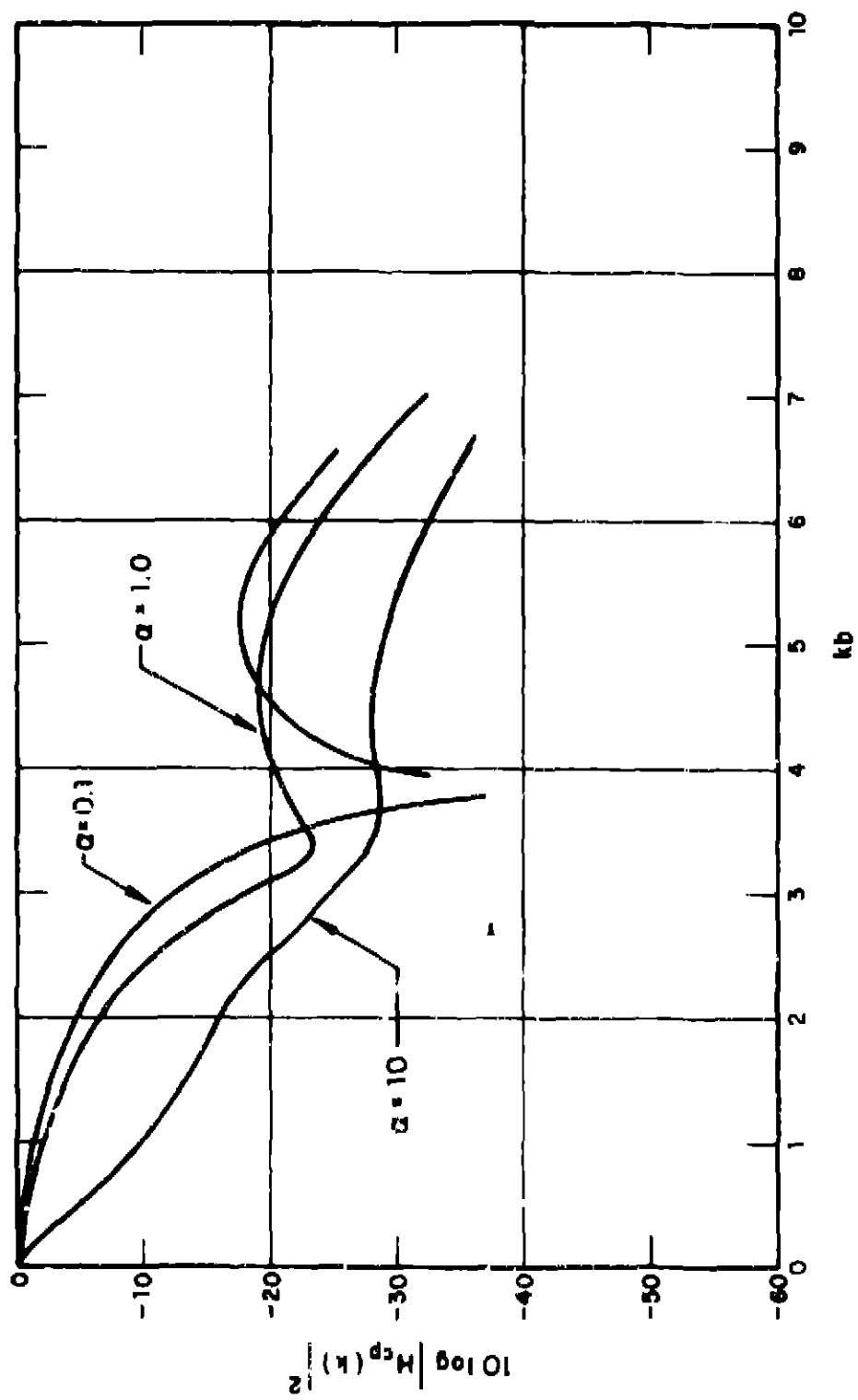
FIG. 2.4-2 CONTACT PATCH WAVENUMBER FILTER

level is achieved. For the contact patch size calculated above, this reduction would occur for wavelengths on the order of 0.75 in. (1.9 cm) to 1 in. (2.54 cm). For a rapid transit car traveling at 40 mph (64 km/hr), these wavelengths correspond to 750 to 1000 Hz. It should be emphasized that the derivation of Eq. 2.4-13 and Fig. 2.4-2 requires making some assumptions about the roughness wavenumber spectrum across the rail head or across the wheel tread. In Eq. 2.4-13 it has been assumed that for a given wavenumber component k_x along the length of the rail or around the circumference of the wheel, the correlation length across the rail head or wheel head is proportional to $1/\alpha k_x$. Other assumptions are also possible, as is discussed in Appendix B.

Combining Eq. 2.4-13 with Eqs. 2.4-9, 2.4-10, and 2.4-11, we obtain

$$\Phi_{FW}(\omega) = \frac{\omega^2}{V} \left| \frac{Z_R Z_W}{Z_R + Z_W} \right|^2 \; |H_{CF}(k)|^2 \; [\Phi_{rr}(k) + \Phi_{WW}(k)]$$

$$(2.4-14)$$

$$\Phi_{V_W V_W}(\omega) = \frac{\omega^2}{V} \left| \frac{Z_R}{Z_R + Z_W} \right|^2 \; |H_{CF}(k)|^2 \; [\Phi_{rr}(k) + \Phi_{WW}(k)]$$

$$(2.4-15)$$

$$\Phi_{V_r V_r}(\omega) = \frac{\omega^2}{V} \left| \frac{Z_W}{Z_R + Z_W} \right|^2 \; |H_{CF}(k)|^2 \; [\Phi_{rr}(k) + \Phi_{WW}(k)] \; .$$

$$(2.4-16)$$

where the subscript x has been dropped and $k = \omega/V$.

Having recognized the role of the local deformations at
the wheel/rail interface in effectively filtering the short
wavelength components of roughness, we immediately speculated
on the effect of this local deformation on the wheel and rail
impedance which appear in the above response equations. We
have examined this effect in Appendix C and found it to be neg-
ligible except at high frequency. As a result no corrections
for the contact stiffness will be made in the response equa-
tions.

2.4.2 Sound radiation

The preceding response equations, Eqs. 2.4-15 and 2.4-16,
are, of course, for the response at the point of contact between
the wheel and the rail. It remains to translate these response
spectra into sound pressure levels (SPL) spectra at the wayside.

The Rail

The acoustic radiation from the rail has already been ex-
amined in some detail in Sec. 2.1.4 in the discussion of direc-
tivity. Recall that the acoustic pressure spectrum at distance
R from the rail due to a single point of excitation directly
opposite the point where the pressure is measured is given by

$$\Phi_P(\omega) = J_R \cdot \omega_H + w_F) \; \frac{(\rho_o)^2}{\pi} \; \frac{f(\eta R)}{R} \; \Phi_{V_{r''}}(\omega) \; , \qquad (2.4-17)$$

where the directivity function $D(\phi)$ has been taken as unity as
described in Sec. 2.1.4 and where

$$f(\eta R) = 1 \qquad , \qquad \eta R < 1$$

$$f(\eta R) = 1/\eta R \; , \qquad \eta R > 1 \; .$$

In general, for multiple excitation points, such as the many wheels of a train, one simply adds the mean square pressure produced by each, since the sources are independent. Unfortunately, Eq. 2.4-17 is not valid unless the point of excitation is directly opposite the receiver, i.e., the position for measuring the acoustic pressure lies on a perpendicular to the rail at the point of excitation. If the point of excitation actually lies a distance L down the rail we distinguish two cases. The first case, L << R, can be approximately determined by Eq. 2.4-17. The second case, L >> R, can be derived from the "exact" expression for the pressure spectrum Φ_p

$$\Phi_P(\omega) = \sigma_R(W_H + W_F) \frac{(\rho c)^2}{2\pi} \Phi_{V_r V_r}(\omega)$$

$$\cdot \left(2 \cosh\eta L \int_L^\infty \frac{e^{-\eta x} dx}{x^2 + R^2} + e^{-\eta L} \int_{-L}^{L} \frac{e^{-\eta x} dx}{x^2 + R^2} \right),$$

while for L >> R can be well approximated

$$\Phi_P(\omega) = \sigma_R(W_H + W_F) \frac{(\rho c)^2}{2\pi} \Phi_{V_r V_r}(\omega) \frac{e^{-\eta L}}{R}$$

$$\cdot \left\{ \frac{\eta R}{\eta L} \cosh \eta L[1 - \eta R E_1(\eta L)] \right\},$$

where $E_1(\eta L)$ is the exponential integral defined by

$$\int_{\eta L}^\infty \frac{e^{-x}}{x} dx .$$

The bracketed term in Eq. 2.4-18 is plotted in Fig. 2.4-9. Multiplying the values in that figure by $e^{-\eta L}$, we obtain the

$$10 \log_{10} \left\{ \frac{\eta R}{\eta L} \cos h \, \eta L \left[1 - \eta L e^{\eta L} E_1(\eta L) \right] + f(\eta R) \right\}$$
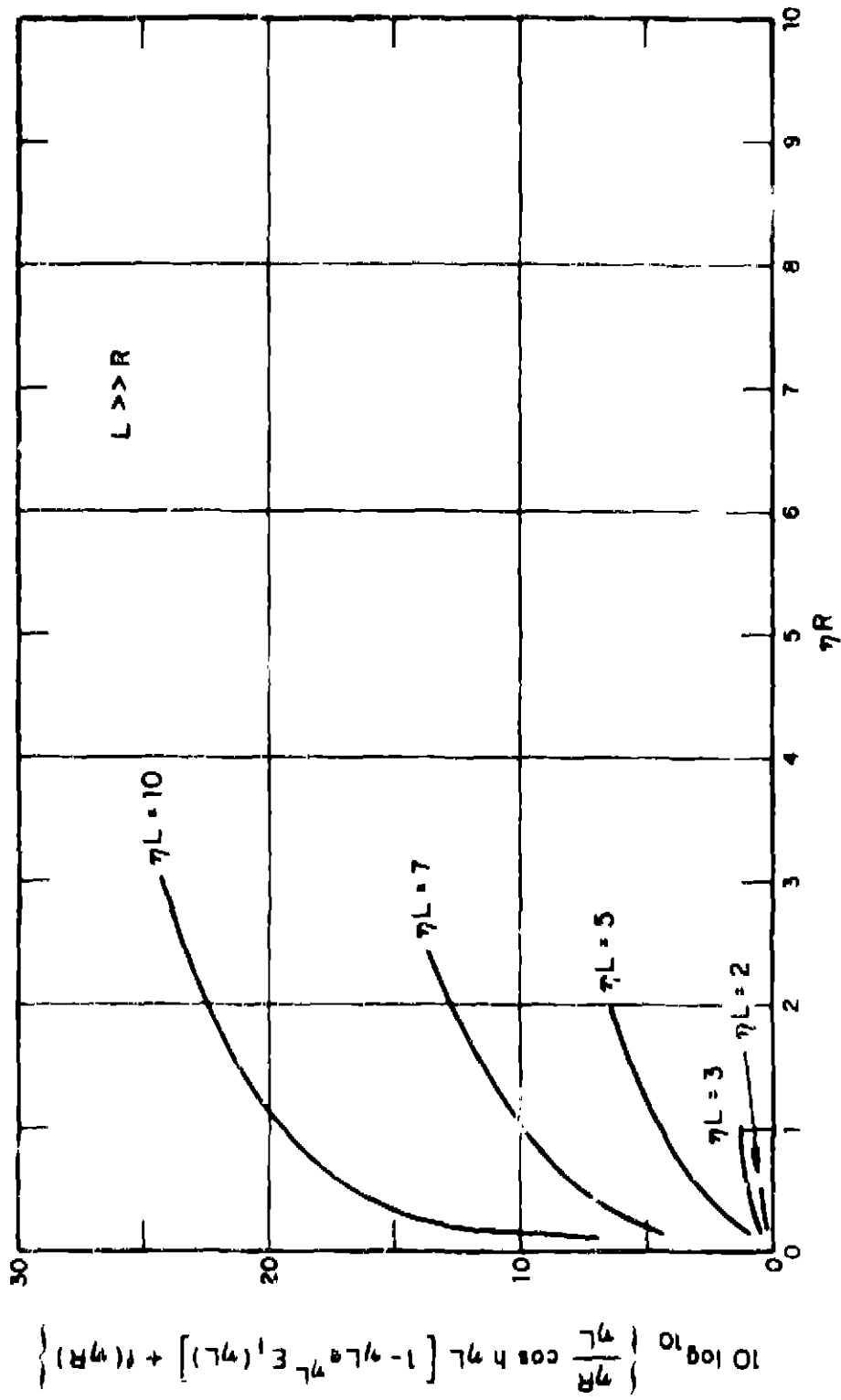
FIG. 2.4-3 DISTANCE CORRECTION FOR RAIL NOISE

perpendicular distance from the rail to the receiver, gives the
appropriate distance correction for the sound pressure level
radiated by the rail. Figure 2.4-3 shows a strong tendency at
large rL for the SPL from the rail to remain constant with dis-
tance from the rail. This results from the fact that the con-
tribution to the rail noise is primarily due to the rail vibra-
tion at the excitation point and for L >> R the distance from
the excitation point to the receiver does not change signifi-
cantly as one moves away from the rail.

By using Eqs. 2.4-17 or 2.4-18, then, one can calculate
the SPL from the rail due to a single excitation point. For
many excitation points, one simply sums the mean square pres-
sure from each.

The wheel

Roar occurs when the wheel is excited at the tread in the
radial direction. The response in Eq. 2.4-15 refers to the
radial motion of the wheel tread surface. However, the primary
radiating surface of the wheel (greatest area) is the web.
Fortunately, in Sec. 2.1.2 it was shown that vibration levels
averaged over the wheel tread in the radial direction are
essentially equal to the axial vibration levels averaged over
the web. Thus, using Eq. 2.4-6 and treating the wheel as a
monopole source with uniform directivity (see Sec. 2.1.4) re-
sults in the following expression for the pressure spectrum at
distance R from the wheel:

$$p_1(\omega) = \sigma_W(\rho c) \cdot \frac{A^2}{4\pi R^2} \, b_r V_b(\omega) , \qquad 2.4-19$$

where $\Phi_{V_r V_r}(\omega)$ is the spectrum of the radial velocity of the wheel tread at the point of contact between the wheel and the rail.

Predictive Formulas

Equation 2.4-16 appropriately combined with Eqs. 2.4-17 or 2.4-18 and Eq. 2.4-16 combined with Eq. 2.4-19 yield an analytical prediction of the pressure spectrum produced by a single wheel interacting with a rail. It is useful to rewrite these expressions in terms of the SPL in a given frequency band $\Delta\omega$. Combining Eqs. 2.4-17 and 2.4-18 with Eq. 2.4-16, and Eq. 2.4-19 with Eq. 2.4-15, dividing the pressure spectrum by p_0^2 ($2 \cdot 10^{-5}$ N/m², the standard reference pressure), multiplying both sides of the equation by $\Delta\omega$, and taking ten times the logarithm of both sides yields for the rail

$$
SPL_{\Delta\omega}(R) = 10 \log \sigma_R + 10 \log\left(\frac{w_H + w_m}{\pi h}\right) + 10 \log \left|\frac{z_w}{z_w + z_R}\right|^2
$$

$$
+ 10 \log \left|H_{cp}(k)\right|^2 + 10 \log \left|\left(\frac{\rho_0 c}{P_0}\right)^2 \Phi_{mR}(R)\Delta k\right|
$$

$$
+ 10 \log G(\eta h, k) ; \qquad k = \omega^\gamma , \qquad (2.4-20)
$$

where $\Delta k = \Delta\omega/V$, $\Phi_{mR}(k)$ is the total wheel and rail wavenumber spectrum of microroughness, V is the wheel velocity on the rail, and $G(\eta R, \cdot)$ is given as

$$
G(\eta R, \eta L) = f(\eta R) \qquad f \quad p \quad h \quad \omega
$$

2-1

$$G(nR,nL) = e^{-nL}\left[\frac{nR}{nL}\cosh nL(1-nL)e^{nL}\,E_1(nL) + f(nR)\right]$$

$$\text{for} \quad L \gg R^* \;,$$

where R is the perpendicular distance from the rail to the receiver and L is the distance along the rail from that perpendicular to the excitation point. For the *wheel*

$$SPL_{A\omega}^{(w)} = 10\log \sigma_W + 10\log\frac{a^2}{2R^2} + 10\log\frac{Z_R}{Z_R+Z_W}$$

$$+ 10\log|H_{cp}(k\xi)|^2 + 10\log\left[\left(\frac{\rho c\omega}{P_0}\right)^2\right.$$

$$\left.\cdot\;\Phi_{rR}(k)\Delta k\right], \tag{2.4-21}$$

where R is the distance from the wheel to the receiver.

Equations 2.4-20 and 2.4-21 constitute the formulas for the prediction of roar noise due to wheel/rail interaction. They require knowledge of: the radiation efficiency σ of wheels and rails, measurements of which are described in Sec. 3.1.3; the geometry (wheel radius, rail head and foot widths distance to the receiver); the wheel and rail impedance Z_W and Z_R, measurements of which are found in Sec. 3.1.1; the geometry of the contact patch (which depends on wheel/rail geometry and load); and the roughness spectrum on the wheels and rails. Until recently no measurements of $\Phi_{rR}(k)$ existed. The next section describes a device built during this program to gather such data.

_____ ____ _

*See Fig. 2.4-3.

2.4.3   Wheel/rail roughness measurements

During the program described in this report, we developed
a device for measuring the roughness spectrum on wheels and
rails.   With the device we obtained some representative measure-
ments of wheel and rail roughness on wheels and rails in revenue
service transit systems.   Additional data appear in Sec. 3 where
the Pullman Standard verification tests are described.

General Description of the Roughness Measuring Device

A sketch of the roughness measuring device is shown in
Fig. 2.4-4.   It consists of a probe pulled along by a carriage
moving along a smooth track (I-beam) parallel to the rail at
constant speed u.   An accelerometer is attached to the probe
which is in contact with the "rough" rail surface.   The probe
is attached to the carriage by means of a hinge joint (a strip
of teflon).   The roughness of a wheel is measured in a similar
way, i.e., by mounting the carriage to a table with the probe
touching the surface of a rotating wheel.

The spatial fluctuations of the rail or wheel surface are
converted to temporal fluctuations of acceleration at the probe
so that the power recorded at frequency ω corresponds to a
spatial variation of wavelength λ given by

$$\lambda = \frac{2\pi u}{\omega} .$$

In both cases, the total signal recorded by the accelerometer
is partially due to the roughness of the surface under test,
partially due to undesired vibration of the coupling device as
from the I-beam or subbase, and partially due to ambient ground
vibration.   We were able to minimize the ambient and vibra-
tion by measuring only during quiet periods.
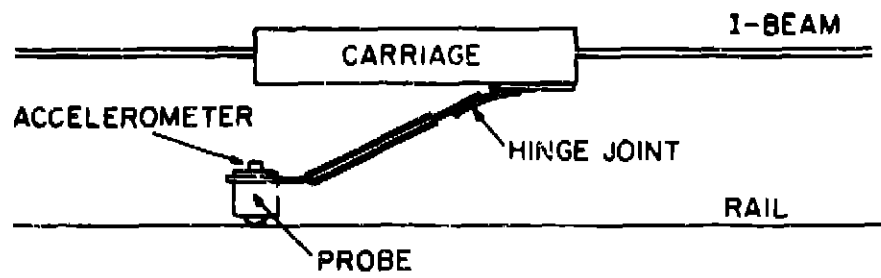
(a)
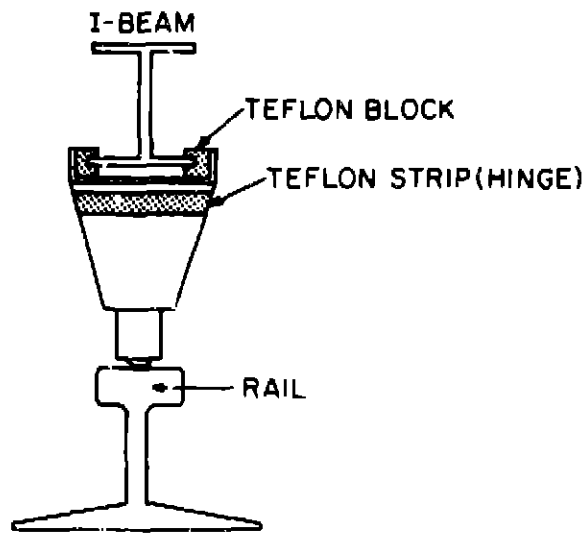
(b)

FIG. 2.4-4 ROUGHNESS MEASURING DEVICE

The extraneous vibration transmitted from the carriage to
the probe was minimized by the choice of a hinge to couple
the carriage to the probe. The hinge is effectively a low-rate
spring that with the mass of the probe forms a spring mass
vibration isolation system, i.e., effectively a low-pass filter
for rejecting carriage-generated vibration. In general, car-
riage-generated vibration was not a problem, primarily because the
roughness of the I-beam was much lower than the roughness on the
wheels and rails being measured. A detailed laboratory evalua-
tion of the device was carried out to verify its proper opera-
tion. Appendix D presents the results of that successful
evaluation.

Preliminary Rail Roughness Measurements

The roughness of typical rail sections under normal use
was measured during field trips to the Boston and Maine rail-
road yard at Ayer, Massachusetts and the Massachusetts Bay Trans-
portation Authority (MBTA) station at Forest Hills, Massachuetts.
The data were stored on magnetic tape that was later used to
obtain 1/3-octave band spectra.

The first set of data was not filtered before being
recorded, because a relatively constant spectrum level was
anticipated. This "all pass" record proved, however, to be
undesirable because the useful signal was masked by high-
frequency noise. This noise was partially produced by small
pits which are abundant on all normally used rails and parti-
ally produced by a contact resonance which was estimated to be
in the vicinity of 1 kHz. When the high frequencies were later
filtered out, the actual low-frequency signal was too close to
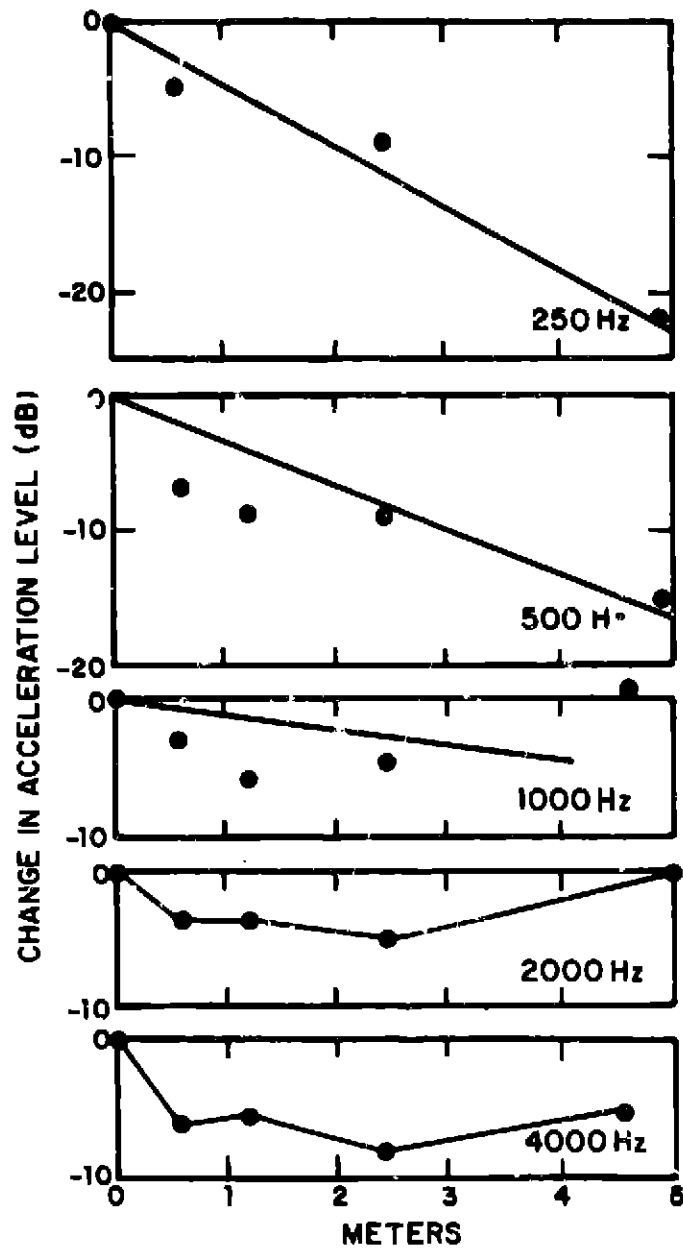the system noise floor to produce any meaningful results.

FIG. 2.1-14   OCTAVE BAND VIBRATION LEVELS VS DISTANCE ALONG
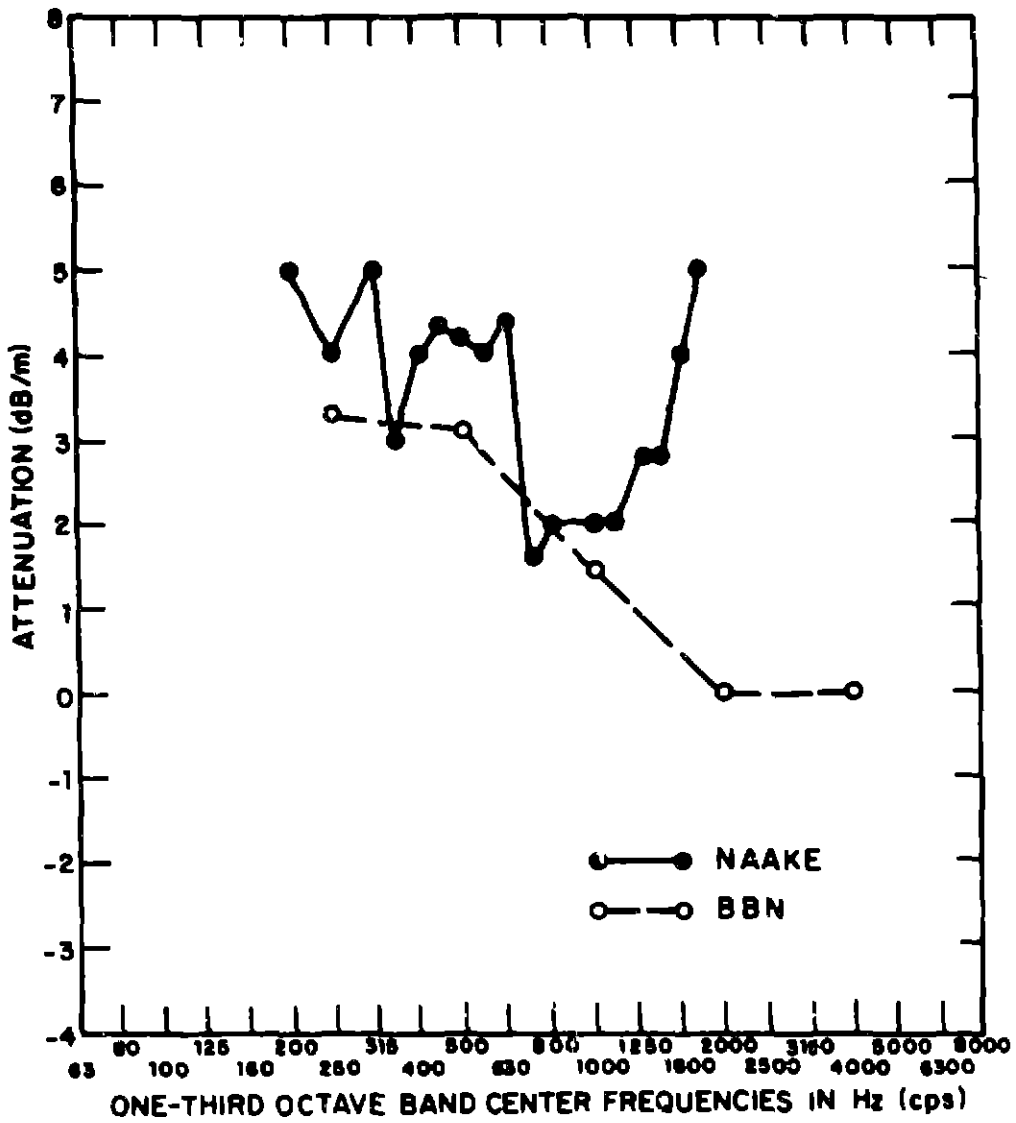A RAIL EXCITED HORIZONTALLY

FIG. 2.1-15 VIBRATION ATTENUATION WITH DISTANCE ALONG A SINGLE
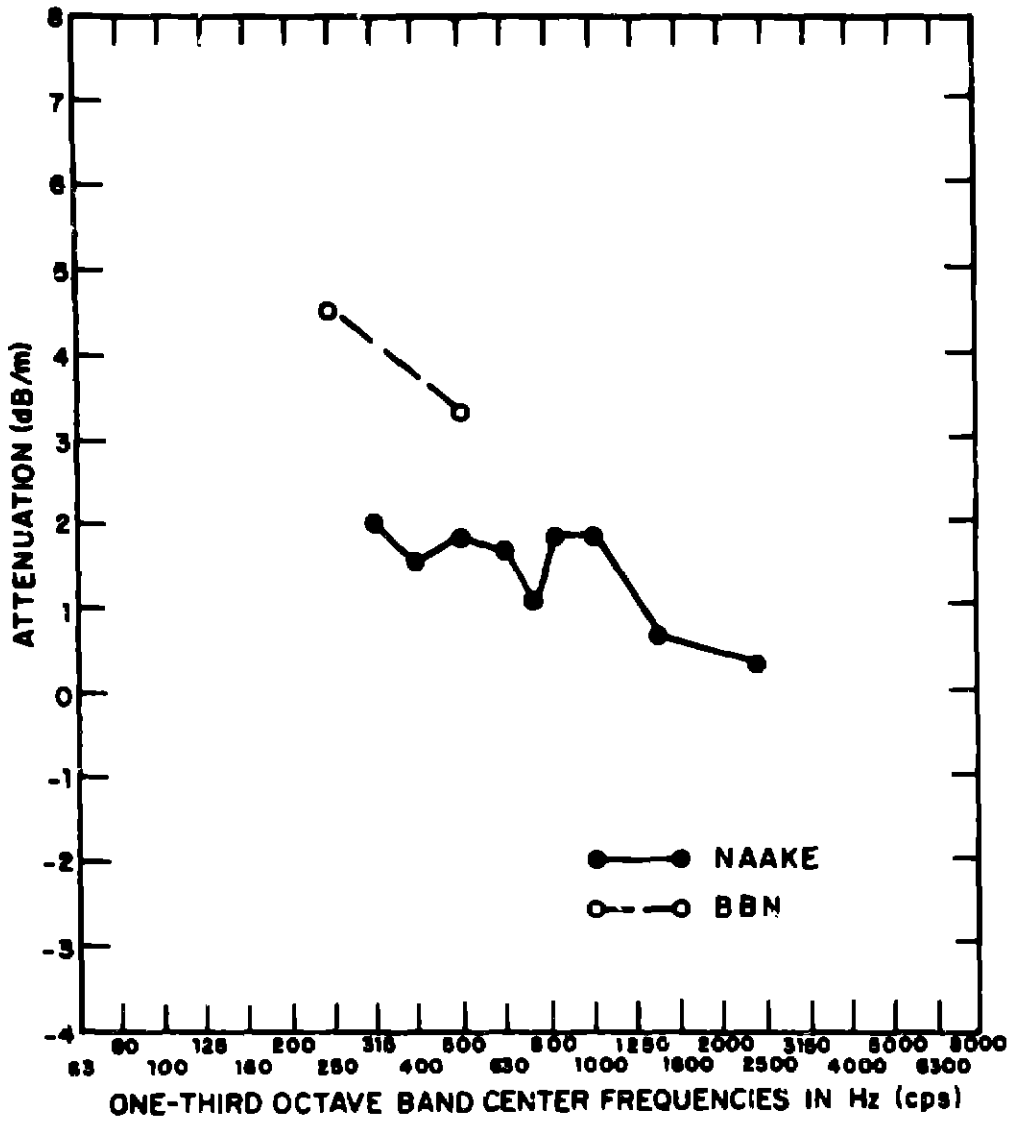LENGTH OF JOINTED RAIL EXCITED VERTICALLY

FIG. 2.1-16 VIBRATION ATTENUATION WITH DISTANCE ALONG A SINGLE
LENGTH OF JOINTED RAIL EXCITED HORIZONTALLY

The results of the background noise and carriage signal measurements are in the form of 1/3-octave band acceleration spectra. It is desirable to transform these measurements into wavenumber spectra of roughness amplitude which are invariant with probe velocity. Equating energy in equivalent spectral bands, one can show that

$$\frac{1}{\omega^4} \Psi_{aa}(\omega)\Delta\omega = \Phi_{mR}(k)\Delta k , \qquad (2.4-22)$$

where $\Delta k = \Delta\omega/u$, u is the probe velocity, $\Phi_{aa}(\omega)\Delta\omega$ is the 1/3-octave band acceleration spectrum sensed by the probe, $\Delta\omega$ is a 1/3-octave band bandwidth at frequency ω, and $\Phi_{mR}(k)$ is the microroughness wavenumber spectrum. The quantity $\Phi_{mR}(k)\Delta k$ is the exact measure of roughness required in Eqs. 2.4-20 and 2.4-21 to produce a 1/3-octave band SPL spectrum in which k and ω are related by $k = \omega/V$, where V is the speed of the train for which predictions are made.

Using Eq. 2.4-22 we have reduced the data taken on a number of segments of MBTA main-line trolley track at the Forest Hills Station. In Fig. 2.4-7 these data are compared with an estimate of the rail roughness on the Staten Island Railroad (based on rail vibration) presented in a recent paper by Bender and Remington (1974). The agreement between the measured and estimated roughnesses gives us further confidence in our device. The discrepancy at high frequency is expected, since Bender and Remington's estimation procedure breaks down above ~1000 Hz. The data from which the estimate was derived were taken during passage of a train at 35 mph (56 km/h). At this speed, frequencies of 1000 Hz are produced by roughness components having a wavenumber of ~10 rad/in. (~4 rad/cm) which is just where the data and estimate start to diverge.
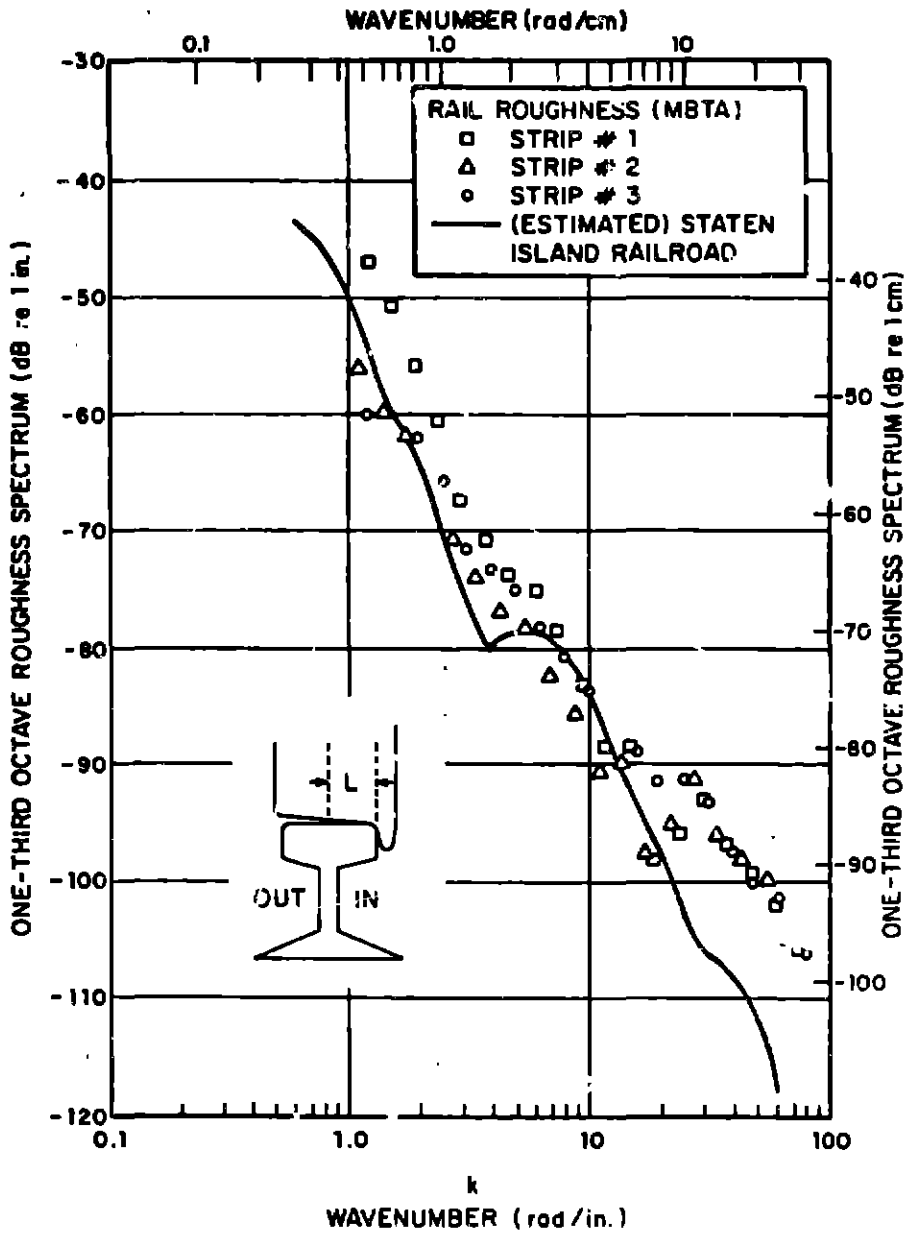
FIG. 2.4-7. MBTA RAIL ROUGHNESS.

Preliminary Wheel Roughness Measurements

We took preliminary wheel roughness measurements on a
24.5-in. (62.2-cm) diameter, 1200 lb (540 kg), surface-line
(streetcar) wheel during a one-day field trip to the MBTA main-
tenance plant at Everett, Massachusetts. The tested wheel was
in fairly good condition with no excessively rough spots.
Roughness spectra were recorded on the wheel tread before and
after the wheel was finished. During the data acquisition,
the roughness measuring device was stationary and the wheel
(actually two wheels and the joining axle) was rotated on a
heavy-duty lathe, as shown in Fig. 2.4-8.

The rotational speed of the wheel was 30 to 100 times
slower during these tests than during actual train operation.
The lower speed is undesirable in that it means a reduction of
the frequency generated by a specific roughness wavelength λ_0
as well as a decrease of the resulting acceleration, thus im-
pairing the signal-to-noise ratio. However, too high a speed
results in such high acceleration levels that the probe jumps
off the wheel surface. When the tread surface of the wheel is
pitted, the jumping-off problem is especially bad. All wheels
tested for roughness, except for the finished wheel, had pitted
surfaces; therefore, we reduced the speed until the "no-jump-
off" condition was satisfied for most of the recorded signal.
The speed of the probe relative to the measured surface was in
both cases (wheel and rail) approximately 15 in./s (38.1 cm/
sec). There were still occasional spikes in some cases which
resulted from the jumps, but they were isolated enough that
their effect on the long-time average was insignificant.

We next tested the wheel set, 24.5 and 24 in. (0.62
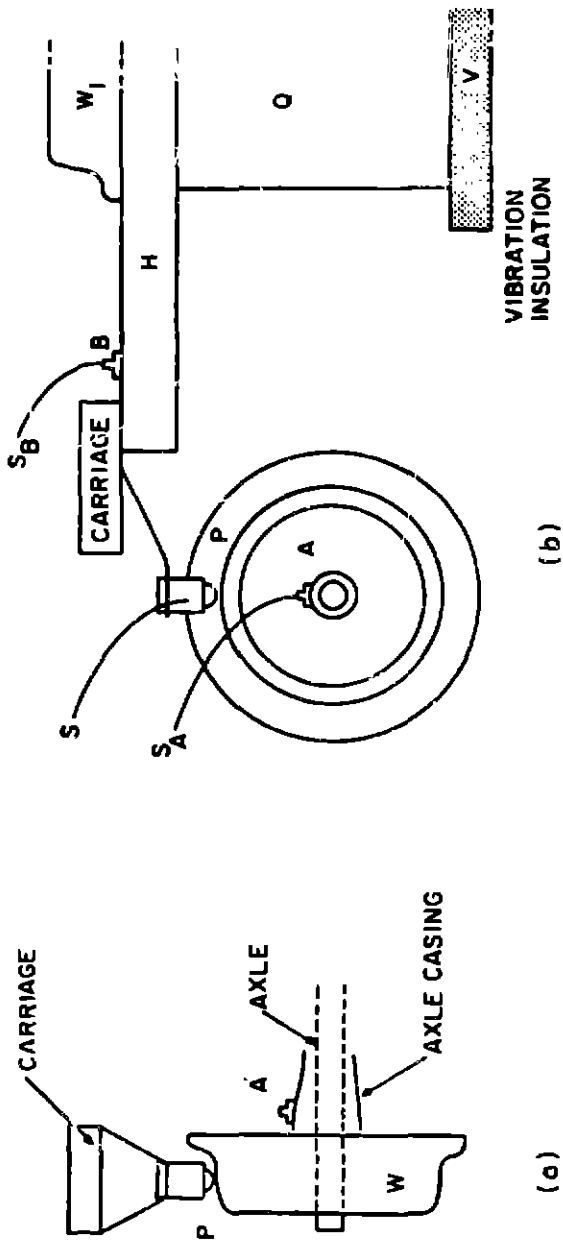and 0.61 m) in diameter before and after turning, respectively,

FIG. 2.4-8 ARRANGEMENT FOR WHEEL ROUGHNESS MEASUREMENT. VIEWED PERPENDICULARLY (a) AND ALONG THE AXLE AXIS (b).

that together with the joining axle, the axle casing, and the last transmission gear was mounted on a heavy-duty lathe. The axle casing was tied to a fixed structure so that only the wheels-axle-transmission gear combination were in motion when the lathe was running at 12.2 rpm. The probe was set in contact with the wheel surface as shown in Fig. 2.4-8. Vibration isolation between the carriage and the floor was provided by the heavy support Q (a stack of pinion gears) and an underlying layer of foam rubber. The carriage was mounted to a channel-shaped beam, H, that rested on Q and was held firmly in position under the 1400 lb (630 kg) weight of a main-line wheel, w_1.

The acceleration levels S, S_A, and S_B measured at points P, A, and B, respectively, are shown in Fig. 2.4-9 for the un-polished wheel. Each curve is the average of three 32-sec runs. The line of contact between the wheel and the probe was near the flange; a line of contact farther from the flange gave similar high-frequency readings but lower low-frequency readings.

The reading S_B is taken with the lathe in operation but with the probe and wheel not in contact. The contribution of S_B to S is $H_p S_B$, where H_p is the carriage to probe transfer function. Clearly, $H_p S_B$ is much lower than S_p and can be readily neglected. The level of S_B is consistently higher when the probe and wheel are in contact; in this case the high S_B reading is caused by vibration transmitted through the probe arm, not through the carriage foundation.

The accelerometer A was placed at numerous locations on the lathe and axle casing; on-spot comparison showed that the vibration was highest on the axle casing, particularly near the rotating transmission gear. We chose point A (Fig. 2.4-8)
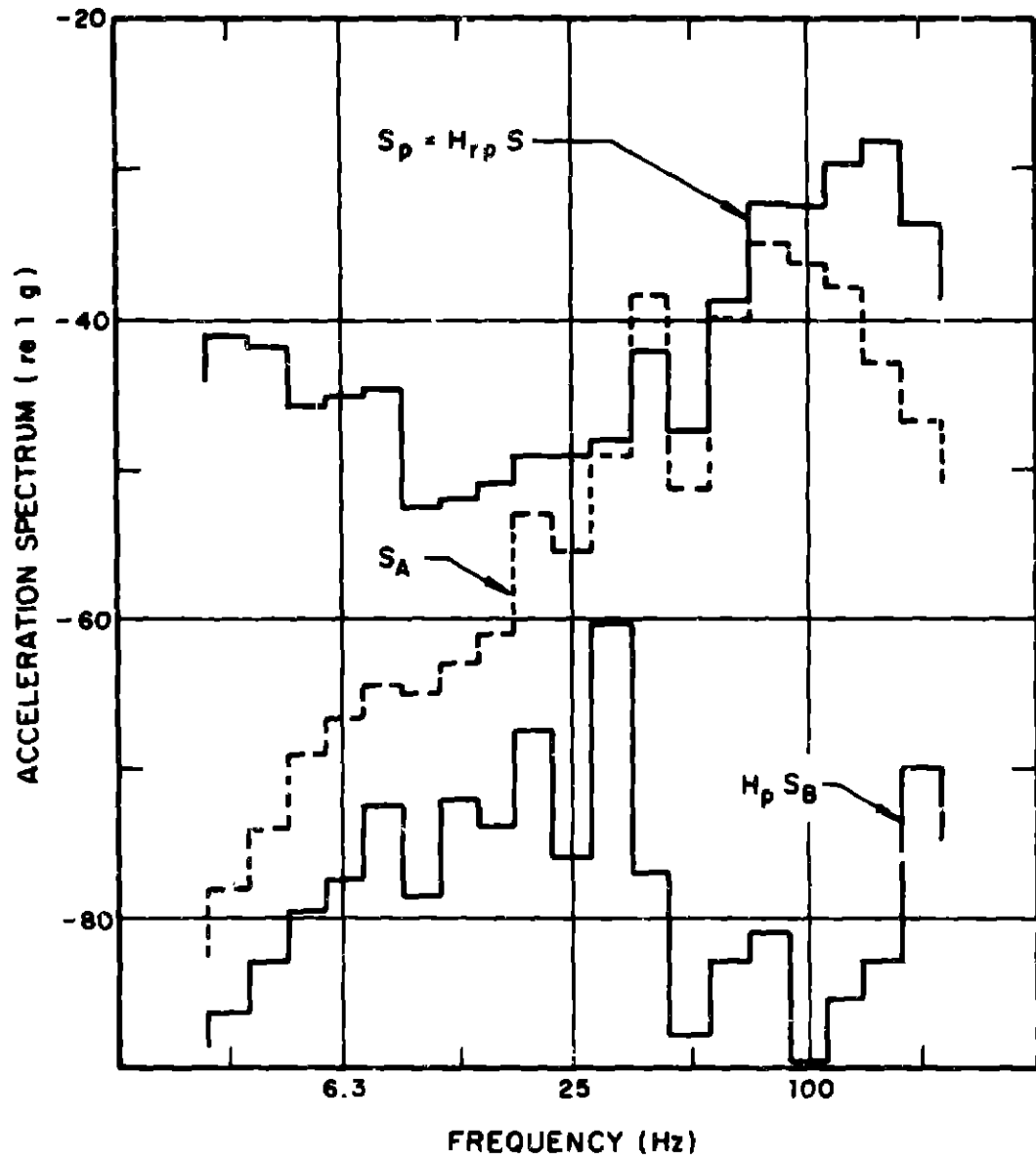
FIG. 2.4-9 ACCELERATION SPECTRA S, S_A, AND S_B AT POSITIONS P AND B RESPECTIVELY

144

on the axle casing because it was closest to the wheel-axle joint. As shown in Fig. 2.4-9, the results for S_A are quite close to S_p between 50 and 100 Hz. However, the proximity of S_A to S_p is not so real as it appears in these plots. It is reasonable to expect that the massive wheels will be less responsive to the stimulus generating the type of vibration picked up at point A. Consequently, S_A should not be taken literally as noise contributed to S, but rather as a maximum upper bound. Assuming this is true, we can then use the total value of S_p to calculate the wheel roughness, which will be slightly overestimated.

After tests on the unpolished wheel surfaces were completed, the wheel was machined with a layer approximately 1/4-in. (0.6 cm) thick being removed. First, a rough finish was performed at low speed and then a finer finish at a higher speed.

As stated earlier, the tested wheel was in fairly good condition even before it was polished. The reason it was machined was to keep it the same diameter as the other wheel on the axle, which was in definite need of repair. This was a rather fortunate coincidence, because the majority of the other wheels scheduled for repairs were too rough for our device and would require a much lower turning speed.

The 1/3-octave band wavenumber spectra for the wheel before and after polishing are shown in Fig. 2.4-10. The data were reduced from the acceleration spectra in the same manner as for the rail. The results are slightly unexpected, because the polished wheel appears to be slightly rougher than the unpolished one in the mid- and high-frequency range. We do observe a definite improvement, however, at low frequencies.

FIG. 2.4-10 WHEEL WAVENUMBER SPECTRA
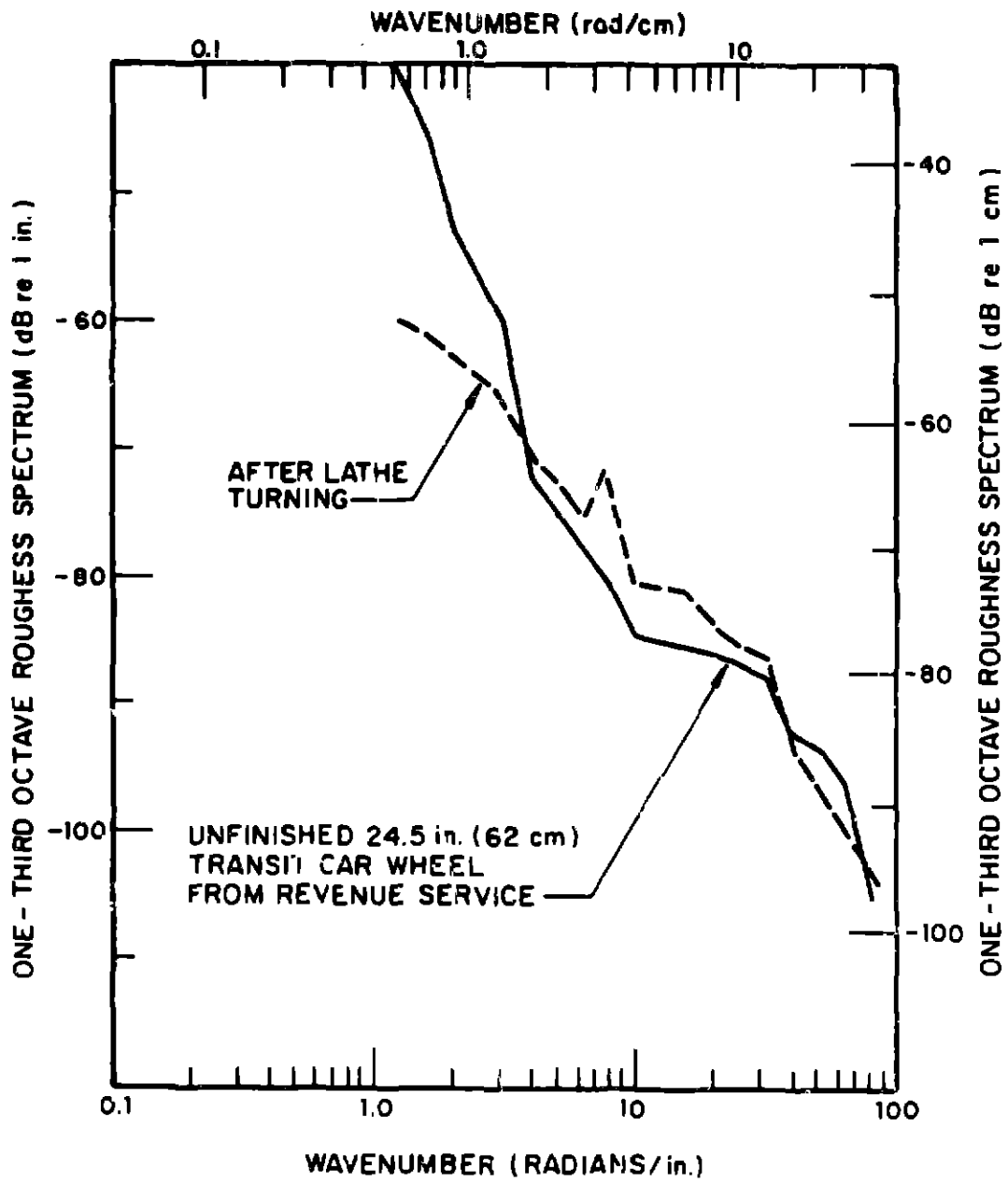
WAVENUMBER (rad/cm)

ONE-THIRD OCTAVE ROUGHNESS SPECTRUM (dB re 1 in.)

ONE-THIRD OCTAVE ROUGHNESS SPECTRUM (dB re 1 cm)

AFTER LATHE
TURNING

UNFINISHED 24.5 in. (62 cm)
TRANSIT CAR WHEEL
FROM REVENUE SERVICE

WAVENUMBER (RADIANS/in.)

Two factors are probably responsible for the peculiar behavior in the mid- and high-frequency range. First, as stated earlier, the tested wheel was in fairly good condition to start with and, therefore, no major change in its roughness could be anticipated. Second, there was evidence of occasional surface chattering with a spatial wavelength of the order of 1 in. (2.5 cm). This could explain the two distinct peaks at 8 and 16 radians/in. (3.1 and 6.2 radians/cm) which correspond to $\lambda \sim 0.75$ and $\lambda \sim 0.375$ in. (1.9 and 0.95 cm). This machine-created "roughness" is probably smoothed out during an initial period of operation before the overall surface condition of the wheel commences to deteriorate again.

In any event, the wheel roughness after lathe turning is about equal to the rail roughness plotted in Fig. 2.4-7.

2.4.4 Prediction of roar noise

With the roughness data of Figs. 2.4-7 and 2.4-10 and the analytical formulas of Eqs. 2.4-17 and 2.4-18, it is possible to make a prediction of roar noise for the MBTA. We can then make an order of magnitude comparison with the data of Hickley and Quinn (1972) taken on the South Shore line of the MBTA (welded rail) just after that line was opened.

We will calculate the SPL at 25 ft (7.6 m) from the track for a train composed of four MBTA Type I South Shore Rapid Transit cars. These cars are 70 ft long (21.4 m); have trucks with a 6.83 ft (~2.1 m) wheelbase; have a center to center truck length of 51 ft (15.6 m); use 28 in. (0.71 m) diameter wheels; and weigh ~60,000 lb (27,200 kg). We will use the rail and wheel roughness data in Figs. 2.4-7 and 2.4-10 (smooth wheel data) and assume a 50 mph (80 km/hr) train speed. These

specifications correspond to a number of measurements performed by Rickley and Quinn (1972).

Predictive Formulas

Taking the rail to be AREA 115 lb/yd (56 kg/m) and the wheel to have 1000 lb (454 kg) mass with a head cross section 5.5 in. wide by 2.75 in. thick (13.9 × 6.9 cm) and using the impedance models of Sec. 2.1.1, we obtain the impedance amplitude shown in Fig. 2.4-11.

Taking the load per wheel to be 10,000/lb (44,500 N), we obtain a contact patch of 0.32 × 0.26 in. (8 mm × 6.5 mm). In order to use the filter characteristics of Fig. 2.4-2, we will use an equivalent radius defined by

$$ b = \frac{1}{2} \sqrt{cd} = 0.15 \text{ in. (6.8 mm)} , $$

where c and d are the length of the major and minor axes of the elliptical contact patch. This relation is based simply on equivalent areas in the circle and ellipse. Adding the roughness spectra for the smooth wheel in Fig. 2.4-10 and the roughest rail in Fig. 2.4-7 and multiplying that result by the wavenumber filter characteristic $H_{cp}(\kappa)$ for $\alpha = 10$ in Fig. 2.4-2 and $(\rho c \omega / p_0)^2$, we obtain the roughness excitation plotted in Fig. 2.4-12.

Taking the wheel radius $a = 14$ in. (35.5 cm), the rail head width $w_H = 2-23/32$ in. (6.8 cm), the foot width $w_F = 5.5$ in. (14 cm), and the perpendicular distance from rail to the observer $R = 25$ ft (7.6 m), we can write the equation for the SPL from a single rail and wheel:
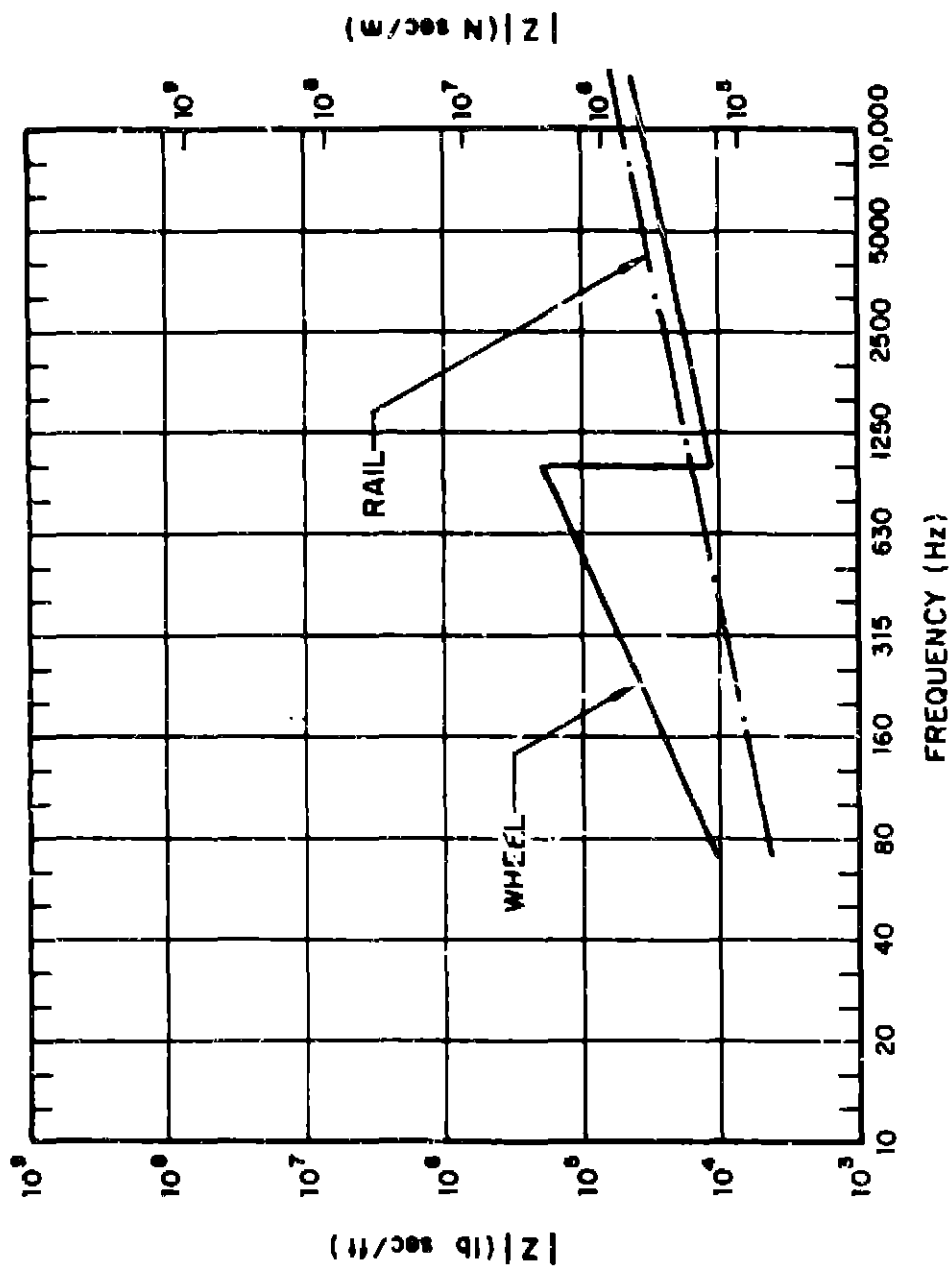
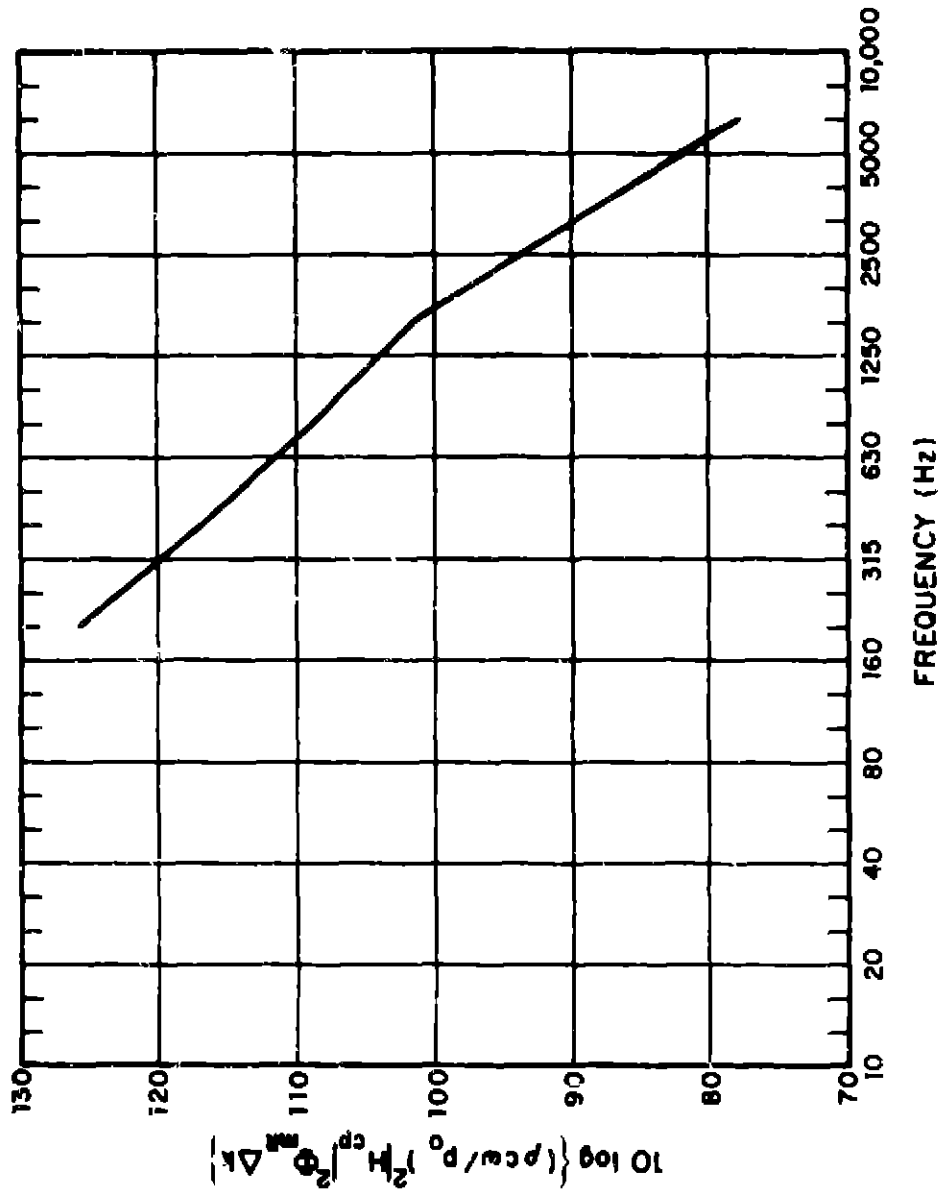FIG. 2.4-11 MBTA WHEEL AND RAIL IMPEDANCE AMPLITUDES

FIG. 2.4-12 ROUGHNESS EXCITATION

$$SPL_{\Delta\omega}^{(R)} = 10 \log \sigma_R + 10 \log \left|\frac{Z_W}{Z_W + Z_R}\right|^2 + 10 \log \left|\left(\frac{\rho c \omega}{P_0}\right)^2\right.$$

$$\left. \cdot H_{cp}(k)\Phi_{mR}(k)\Delta k\right| - 21 + 10 \log G(\eta R, \eta L)$$

$$SPL_{\Delta\omega}^{(W)} = 10 \log \left|\frac{Z_R}{Z_R + Z_W}\right|^2 + 10 \log \left|\left(\frac{\rho c \omega}{P_0}\right)^2 H_{cp}(k)\Phi_{mR}(k)\Delta k\right|$$

$$- 26 - 20 \log \frac{R'}{25} \quad ,$$

where R' is the linear distance from the wheel to the observer
and L is the distance parallel to the rail from the observer to
the wheel.

We must now sum the contribution from the 16 wheels on the
train. We will ignore the wheels and rail on the opposite
side of the track, assuming that the car body effectively blocks
their contribution.* The geometry of the situation when the
train is opposite the observer is shown in Fig. 2.4-13.
Further, we only consider the four wheels directly opposite the
observer as significant wheel sources. However, all sixteen
wheels excite the rail and we must account for each. At some
frequencies, when the loss factor η, which determines the decay
rate along the rail, is large, the excitation of the rail by a
wheel far down the track will not contribute significantly to
noise perceived by the observer. However, if η is small, the
excitation produced by a wheel far down the track will result
in significant vibration in the rail directly opposite the
observer. The distance for sound propagation is then R as
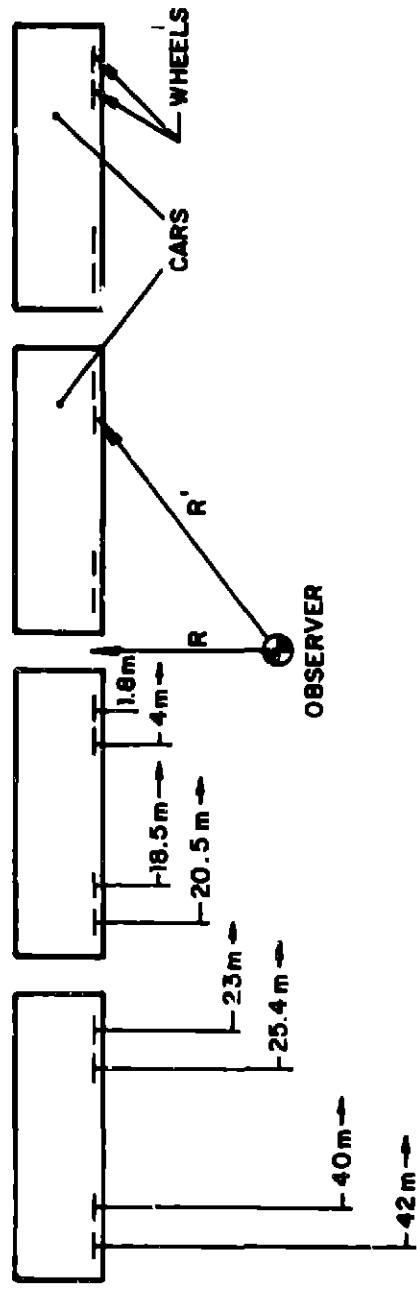
---

*This will, at most, lead to a 3 dB underprediction.

FIG: 2.4-13   FOUR-CAR TRAIN SHOWING THE DISTANCE PARALLEL TO THE TRACK
IN METERS FROM THE OBSERVER TO EACH WHEEL

152

opposed to R' (see Fig. 2.4-13) and, as a result, the excitation in the rail produced by the wheel may be a significant source of noise.

The mathematics for the process have been worked out approximately in Sec. 2.4.1. Using the values of η measured in Sec. 2.1.2 and Figs. 2.1-25 and 2.4-3, we find that below 2000 Hz only the excitation produced in the rail by the four wheels directly opposite the observer contributes significantly to the radiated noise. Above 2000 Hz the excitation produced by all sixteen wheels is significant.[*] The result of carrying out the above calculations is shown in Fig. 2.4-14. Both the wheel and rail contributions and their sum are shown in the figure and compared with the range of sound pressure levels measured during five pass-bys (Rickley and Quinn, 1972). The predictions fall acceptably within the range of measured data. The wheel contribution dominates at low frequencies and the rail dominates at high frequencies. However, this should not be taken as a general result. The relative contributions of wheel and rail noise depend on the distance of the observer from the rail and the relative magnitude of the wheel and rail impedance.

Since the wheel is predominantly a point source and the rail (when η is small) is predominantly a line source, as the observer moves away from the rail, the wheel contribution to the SPL decays more rapidly $(1/R^2)$ than the rail contribution $(1/R)$. As a result, one would expect the rail to become a more significant source as one moves away from the rail. We will address this and other points in Sec. 3 when a more

----

[*]This is an approximation based on quite limited measurements of η. Extrapolating measurements made over a 5 m length of track to 40 m is quite necessarily fraught with danger. But at most we are introducing a 6 dB overestimation of the SPL.
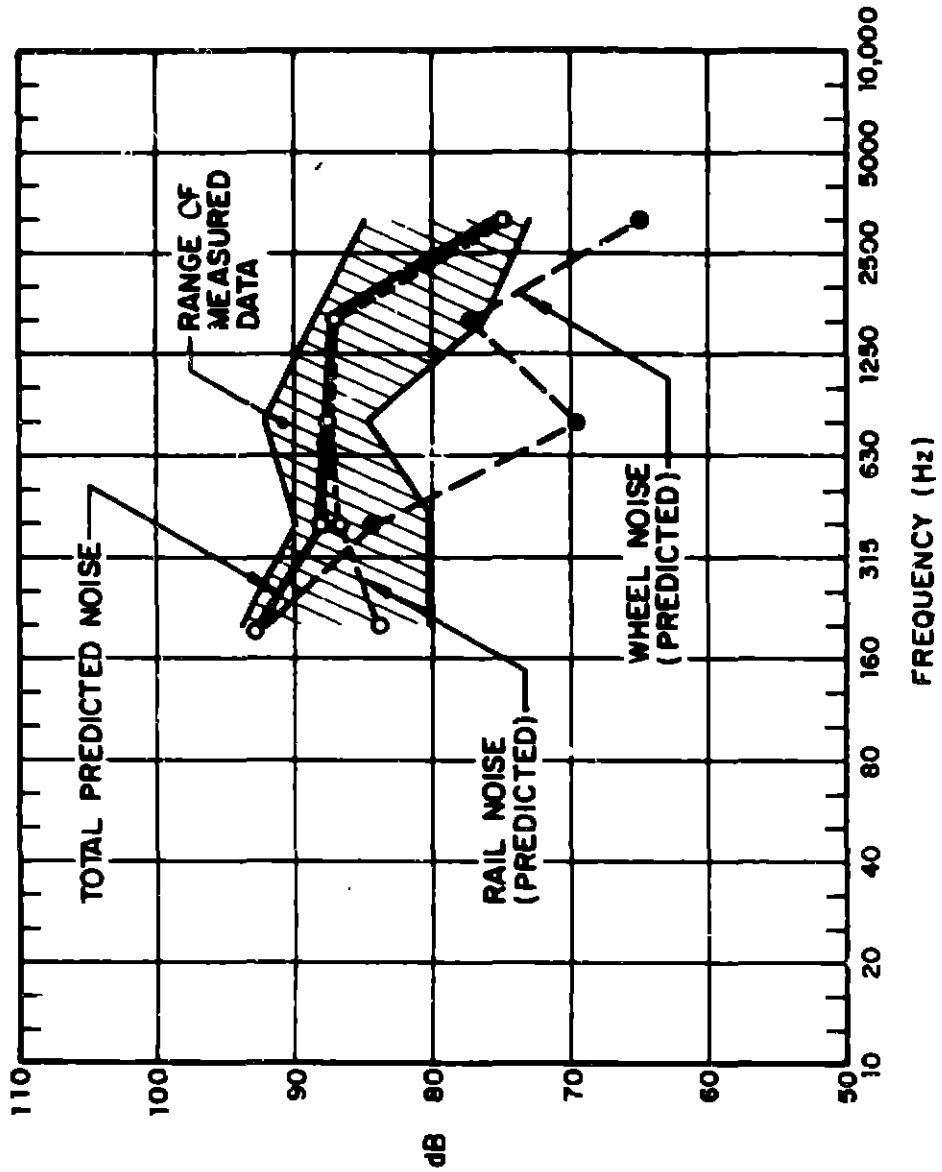
FIG. 2.4-14 COMPARISON OF ROAR NOISE PREDICTIONS AND MEASURED DATA

complete comparison with measured data will be carried out. In Sec. 4 we will discuss the noise control implications of the roar noise model.